TECHNISCHE UNIVERSITÄT MÜNCHEN

Lehrstuhl E20-

Molekulare Nanowissenschaften & Chemische Physik von Grenzflächen

Tuning non-covalent interactions in two dimensions: from H-bonded networks to metal coordination

Bodong Zhang

Vollstädiger Abdruck der von der Fakultät für Physik der Technischen Universität München zur Erlangung des akademischen Grades eines Doktors der Naturwissenschaften (Dr. rer. nat.) genehmigten Dissertation.

Vorsitzender:	Prof. Dr. Björn Garbrecht
Prüfer der Dissertation:	1. Prof. Dr. Johannes V. Barth
	2. Priv.-Doz. Dr. Markus Lackinger

Die Promotion wurde am 22.05.2019 bei der Technischen Universität München eingereicht und durch die Fakultät für Physik am 10.07.2019 angenommen.

Abstract

The design of surface-confined low-dimensional nanoarchitectures provides important guidance for ultra-thin functional films fabrication. Therefore, functional molecules serving as building blocks for supramolecular structure as well as embedding metal atoms in them attracts growing attentions.

In this thesis, we have investigated ordered low-dimensional nanostructures formed by lophine derivatives and hydroxamic acid molecules on (111) close-packed faces of Au, Ag and Cu. The structures were explored by means of scanning tunneling microscopy and X-ray photoelectron spectroscopy under ultra-high vacuum, which reveal that the formation of distinct nanostructures is driven by hydrogen bonding and metal-organic interactions. Lophine derivatives show competitive interactions with metal atoms on different interaction sites. The flexible hydroxamic acid group induces the formation of multiple nanostructures, whereby the dehydrogenation of the hydroxamic acid group leads to novel self-assembled structures.

Our investigations reveal the self-assembly behavior of these functional molecules and their potential application in luminescence, sensors and biology.

Contents

Abstract......I

Contents...... III

1. **Introduction**...... 1

2. **Methodology**...... 7

2.1 Scanning tunneling microscopy (STM)...... 7
2.1.1 Theory of the tunneling effect...... 8
2.1.2 Scanning modes...... 13
2.1.3 Experimental set-up...... 14
2.1.4 Sample preparation...... 19

2.2 X-ray photoelectron spectroscopy (XPS)...... 19
2.2.1 Principle of XPS...... 19
2.2.2 Experimental setup...... 22

3. **On-surface assembly of a chemiluminescent module: porous and densely packed structures by simultaneous expression of different metal coordination motifs**...... 25

3.1 Self-assembled structures of TCPI on Ag(111)...... 26

3.2 Self-assembled structures of TCPI on Au(111)...... 29

3.3 Metal-organic structures of TCPI on Cu(111)...... 34

3.4 Summary and conclusions...... 37

4. **Emerging complexity in two dimensional molecular architectures with bis-hydroxamic acid linear modules**...... 39

4.1 Isolated molecule on Ag(111) and Au(111) surfaces...... 41

4.2 Molecular ensembles on Ag(111) and Au(111)...... 44

4.3 Summary and conclusions...... 55

5. Metal-organic structures of hydroxamic acid on metal surface 57
5.1 Co directed coordination structure on Au(111) 58
5.2 Co directed coordination structure on Ag(111) 62
5.3 Concluding remark 69
6. Thermal chemistry and self-assembly of a dihydroxamic acid linear linker on Cu(111) 71
6.1 Densely packed metal-coordination structure on Cu(111) at room temperature .. 72
6.2 2D metal-organic coordination network involving stoichiometriadatoms/BPDH ratio on Cu(111) at room temperature 73
6.3 Stable metal-coordination structure on Cu(111) 77
6.4 Conclusion 81
7. Conclusions and Outlook 83
8. Acknowledgements 85
9. List of Publications 87
10. List of Figures 89
11. List of Tables 93
12. List of Abbreviations 95
Bibliography 97

1. Introduction

Nanotechnology requires the control of matter at the atomic scale, a concept put forward by the famous lecture of Richard Feynman: “There’s Plenty of Room at the Bottom” [1] in 1959. Since then, research about nanotechnology took off. In 1968, the technique of molecular beam epitaxy (MBE) was invented [2]. It offers a very important deposition method to fabricate thin-films with a very low deposition rate on a wafer under ultra-high vacuum. With this approach, scientists have fabricated single molecular layers with precisely controlled quantities and compositions. Therefore, MBE played a crucial role in the evolution of nanoscience and nanotechnology [3]. Then in 1976, atomic layer deposition was introduced by Thumo Suntola [4], which is an indispensable tool in the synthesis of nanomaterials. In 1981, scanning tunneling microscopy (STM) was created by Binnig and Roher in IBM Rüschlikon laboratory, a very powerful tool to observe and control nanostructure on surfaces at nanometer scale under a non-contact working mode, without destruction to the sample. Its theoretical basis originates from the quantum tunneling effect: the electrons could pass through a non-contact gap between two conductors (or semiconductors). The tunneling current shows exponential decay with increasing distance between the two electrodes. Through recording the change of tunneling current or movement at the vertical direction of the tip, the precise surface topography could be obtained at atomic scale. STM also could monitor single molecular movements continuously in the same area as a function of time at room temperature or low temperature. Subsequently in 1986, atomic force microscopy (AFM) was invented. Thus, a series of related techniques were introduced, classified as scanning probe microscopy (SPM). After several years, researchers from IBM Almaden laboratory successfully manipulated the position of single xenon atoms on a nickel surface with the STM tip [5], which is the first example of controlling the position of a single atom. In the past decades, nanotechnology proceeded greatly, many novel nanomaterials and nanotechnology processes have been developed and explored, including microcontact printing [6], graphene [7], 1 nanometer thick carbon nanotubes [8] etc.

1. Introduction

There are mainly two ways to synthesize new materials at the nanoscale, named “top-down”, and “bottom-up” methods. The micropatterning techniques containing microcontact printing [9], inkjet printing [10], "Dip-Pen" nanolithography [11] are the more representative nanotechnologies in top-down method. The lithography techniques are widely used in the semiconductor industry, which has brought enormous revolution for the society and the way of human life, through computing and communication technologies. However, in the semiconductor industry, nanolithography on the silicon will quickly approach its physical limitation. Therefore, scientists explore other ways to achieve further miniaturization. The alternative method, “bottom-up” method based on the use of single molecules or atoms to build desired nanostructures through e.g. the self-assembly of molecules with specific functional groups attracts plentiful attentions. In the “bottom-up” strategies, the atoms and molecules could be manipulated, fabricating electronics and machines at nanoscale. Introducing approach of “bottom-up” to the supramolecular chemistry opens a new effective way for artificial construction of nanostructures, which focuses on the chemical systems comprising assembled molecular building blocks, interacting with each other through weak forces, such as hydrogen bonds, metal-organic coordination, π-π stacking, van der Waals interactions etc.. Supramolecular chemistry on surfaces has application potentials in many areas, such as catalysis [12], biosensors [13], data storage [14], nanomachines [15]. STM under ultra-high vacuum provides high resolution images for the topology information of low dimensional nanostructures, while it does not give direct chemical identification. And X-ray photoelectron spectroscopy (XPS) measurements can complementary probe the chemical state of the atoms. The core level electron of an atom is excited by X-ray light and a photoelectron is emitted, with a kinetic energy, which is unique depending on chemical environment of the atoms. Therefore, the chemical state of the adsorbates could be investigated by XPS. Combining techniques of STM and XPS, the supramolecular nanoarchitectures and interactions between the molecules on surface could be obtained.

This thesis will focus on surface-assisted supramolecular structures driven by hydrogen bonding, organometallic interactions. Hydrogen bonding, as a kind of weak interaction force could occur in inter/intra molecules, showing high selective and directional properties. For instance, hydrogen bonding plays a crucial role in biological systems: to direct the formation of multi-hierarchic structures of biological macromolecules. Introducing supramolecular chemistry driven by hydrogen bonding for fabricating low dimensional nanostructures is attractive, and many achievements have been hitherto accomplished [16-18]. Metal-organic coordination is another very important approach to build supramolecular architectures. Molecules with specific functional groups can coordinate with metal atoms, forming well-defined nanostructures by linking organic and inorganic units through relatively strong bonds. The composition, size and geometry of the structure can be regulated, which attracted significant attention in their study. Thus, surface-supported metal-ligand coordination is an important approach to synthesize low-dimension nanofilms, with potential applications in energy storage [19-21], sensors [22-24] and catalysis [25-27].

In this thesis, investigations of 2D nanostructures by STM and XPS under ultra-high vacuum are presented. The theoretical background of the two techniques is briefly introduced in chapter 2. The experimental apparatuses, and procedures including substrate cleaning and preparation of samples are also presented in this chapter.

In the following, we will explore low-dimensional nanostructures on coinage surfaces driven by hydrogen bonding and metal-ligand coordination interactions. A brief summary of these works is as follows:

In chapter 3, tri-phenynitrile imidazole (TCPI) is studied on Ag(111), Au(111) and Cu(111) surfaces. Furthermore its coordination with Co, Fe atoms on Ag(111) and Au(111) as well as its coordination with the native Cu adatoms on Cu(111) is demonstrated and the pertaining nanostructures are characterized. From DFT calculations and STM imaging, we can identify that the phenyl rings of TCPI are not planar on the metal surfaces. On Ag(111) and Au(111), TCPI forms long-range well-ordered 2D architectures through hydrogen bonding, dipolar coupling, the interaction of proton accepter-donator. After dosing Co onto a submonolayer coverage of TCPI, we found different coordination behavior on the two surfaces. On Ag(111) surface, the self-assembly is more stable that the molecules only coordinated with Co atoms on the island boundaries. On Au(111) surface, the previously formed supramolecular islands dissolved into different porous structures with various Co-coordination nodes. From the results of XPS and STM, we identified which moieties of TCPI interacted with Co atoms. The TCPI molecules on Au(111), retain their protonation state under all investigated conditions. After dosing Co, Co-coordination occurred at the imine N of the imidazole group and terminal CN group, as well as between terminal CN groups. On Cu(111), different metal-organic coordination structure with that of on Ag(111) and Au(111) formed. The central imidazole group is intact at room temperature. By increasing temperature, the –NH group dehydrogenated gradually and subsequently coordinated with Cu adatoms.

In chapter 4, the self-assembled structures of 4,4′-biphenyldihydroxamic acid (BPDH) on Au(111) and Ag(111) were investigated. On Au(111), it adsorbs intact assembling in a closed packed structure mediated by intermolecular hydrogen bonding interactions at room temperature and after annealing at 373 K, the chemical state is reflected by XP spectrum. On Ag(111), the molecules form a variety of self-assembled structures. The closed packed structures are the same as that of on Au(111). Additionally, different open network structures are characterized and found to be driven by the -OH group dehydrogenation commencing at room temperature.

In Chapter 5, we further discuss the coordination of BPDH with Co atoms on Au(111) and Ag(111). The molecules still assembled in close packed structures in most of domains on Au(111) surface and on the boundary, the molecules coordinated with Co atoms, forming different coordination nodes at room temperature. After annealing at 373 K, BPDH molecules coordinated with Co atoms to form rigid framework structures. Combining with XP spectrums, we concluded that the -OH dehydrogenated to form coordination bonds with Co, and the aminic N also dehydrogenated with adding Co and further annealing. On the Ag(111) substrate, the molecules could form different coordination structures with Co atoms at room temperature. One structure is open porous metal-organic coordination with different metal centers. A close packed ordered layer is presented on Ag(111), every six molecules coordinate with the metal center comprising one Co atom. The chemical reaction process is similar with that of on Au(111) through XPS results.

In chapter 6, we study the behavior of the BPDH molecules on Cu(111). The molecules coordinated with Cu adatoms at room temperature, leading to different patterns coexisted on the surface. A large area of new close packed structure was observed, while an ordered network structure containing a four-fold coordination node comprising two Cu adatoms. Furtherly, a hexagonal network formed and kept stable at room temperature, which could be served as a molecular cage to confine the molecular dimers. The continuous rotation of the dimer in this hexagonal network is visualized at room temperature. After annealing at 373 K, these coordination structures changed into a sole structure, which presented as a flower-shape coordination pack with a dinuclear Cu adatoms metal node. The -OH groups dehydrogenated at room temperature on the surface, while the aminic N dehydrogenated gradually with the increasing of temperature, resulting that the oxygens interacted with Cu adatoms, the interactions of two oxygens with Cu adatoms support the final stable architecture.

Chapter 7 summarizes all of the presented work and gives future perspectives.

2. Methodology

This part mainly describes techniques and apparatuses employed for the experiments in this thesis. All the measurements in thesis are performed with variable-temperature scanning tunneling microscopy (VT-STM) under ultra-high vacuum conditions. And most of presented STM results are supported by X-ray spectroscopy measurements. Therefore, in the first section, basic theory of quantum tunneling effect is concisely explained, following by introduction of the setup of VT-STM and corresponding to ultra-high vacuum chamber. The second section concentrates on the theory of X-ray photoelectron spectroscopy together with the description of the setup (SPECS GmbH) performed at the E20—WSI laboratory in Garching. Complementary insight was provided by theoretical calculations provided by collaborators. The geometry optimizations presented in chapter 3 were performed by Simon Nadal and the density functional theory calculations in chapter 4 were given by Mariam Ebrahimi. Moreover, the investigations of scanning probe microscopy at 4 K presented in chapter 4 were also carried out by collaborators. These studies support the results and discussion of this thesis are thus presented in only in this context, chapters 3 and 4, without addressing the methodology in this section.

2.1 Scanning tunneling microscopy (STM)

STM as a non-destructive, well-defined conductive surface analysis method was invented by Binnig and Rohrer in IBM Research laboratory, Zurich, in 1981 [28]. It enables the investigation of atomic-scale surface topography in real space, such as revelation of monoatomic steps on Au(110) [29] and atomic resolution of the Si(111) 7×7 reconstruction [30]. It is also used to control single atoms or molecules at the nano scale, which could establish varieties of low dimensional patterns on metal surface. Developing a new way to nanotechnology and wide implement fields, the invention of STM won the Nobel Prize in Physics in 1986. Until now, many breakthrough achievements have been obtained in the fields of manipulation of atoms [31-33], materials science [34, 35] and molecular biology

[36, 37] etc.

Figure 2.1 gives a brief illustration of STM. An atomically sharp metallic tip is placed at a distance of ~ 1 nm from semi-conductive or conductive surface. The relative position of the tip and the sample is controlled by piezo elements. The electrons could pass through the potential barrier between metallic tip and (semi) conductive surface by applying a bias of the order of a few mV to a few V, leading to a net tunneling current flow between them. The tunneling current has an exponential dependence on the gap width between tip and surface.

In the following, the principle of quantum mechanics of tunneling current, different scanning modes and the whole set-up will be introduced briefly.

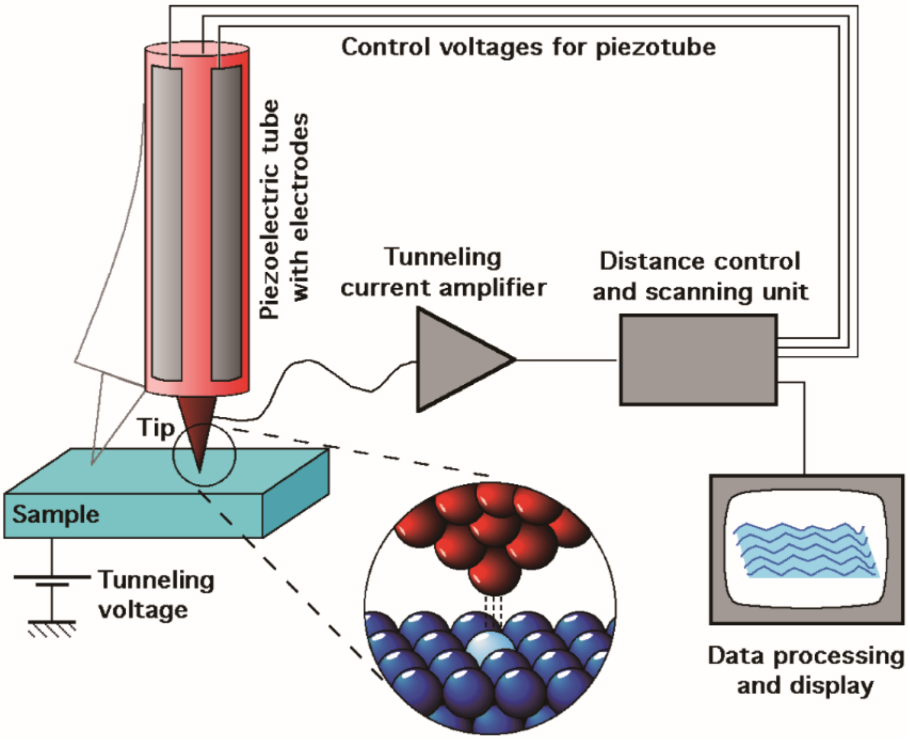
Control voltages for piezotube
Piezoelectric tube with electrodes
Tunneling current amplifier
Distance control and scanning unit
Tip
Sample
Tunneling voltage
Data processing and display

Figure 2.1: Schematic illustration of STM-adapted from [38].

2.1.1 Theory of the tunneling effect

The working principle of STM is based on quantum tunneling effect, explaining the behavior of matter at atomic scale. One of its basic theories is “wave-particle duality”, a result of this concept is the tunnel effect, which is different from classical physical point. In figure 2.2, which depicts the differences between classical and quantum physics. In classical physics, the position and momentum of a particle could be expressed by its trajectory and the particle has no possibility to overcome potential barrier larger than its kinetic energy. However, in quantum physics, electrons with wave-like properties have probability to go through the barrier, even if the potential barrier is higher [39-41].

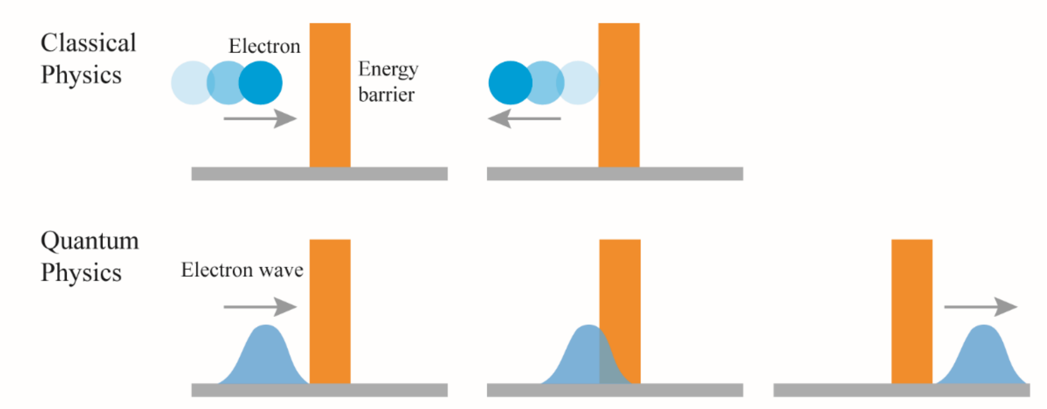

Figure 2.2: Schematic of different views between classical and quantum physics adapted from [42].

In quantum mechanics, electrons can be described by the one dimensional time-independent Schrodinger equation:

$$-\frac{\hbar^2}{2m}\frac{d^2}{dx^2}\psi(x)+V_x\psi(x)=E\psi(x) \tag{2.1}$$

where $\hbar$ is the reduced Plank constant, m is the electron mass, V is the potential barrier, E is the energy of an electron. In figure 2.3, $V = V_0 > E$ when $0 \leq x \leq a$, and $V = V_0 = 0$ when $x \leq 0$ and $x \geq a$.

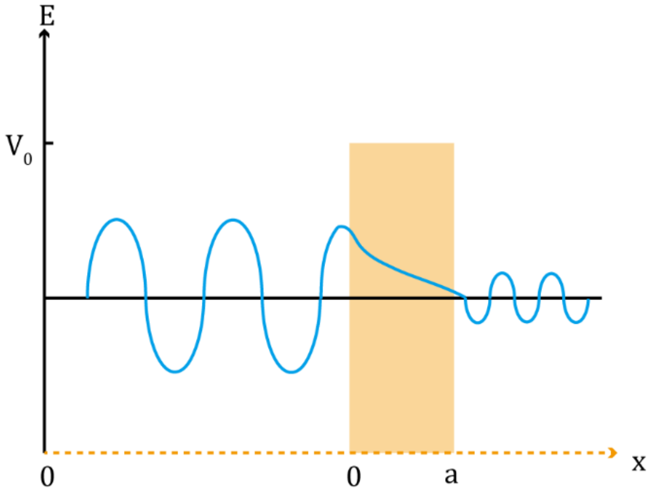

Figure 2.3: Schematic illustration of a particle-wave tunneling through a potential barrier V_0 with width a.

The time-independent Schrödinger equation gives a general solution of the wave function:

$$\psi(x) = \begin{cases} A_1 x e^{ikx} + A_2 x e^{-ikx}, & (x \leq 0) \\ B_1 x e^{\kappa x} + B_2 x e^{-\kappa x}, & (0 \leq x \leq a) \\ C_1 x e^{ikx} + C_2 x e^{-ikx}, & (x \geq a) \end{cases} \tag{2.2}$$

where A_1, A_2, B_1, B_2, C_1 and C_2 are constants, $k = \sqrt{\frac{2mE}{\hbar^2}}$ and $\kappa = \sqrt{\frac{2m(V_0-E)}{\hbar^2}}$. When $x \geq a$, the waves can only propagate out of the potential barrier, C_2 can be set to zero. For a continuous wave function at between 0 and a, the transmission coefficient can be written as:

$$T = \left(1 + \frac{(k^2+\kappa^2)^2}{4k^2\kappa^2} \sin h^2(\kappa a)\right)^{-1} \tag{2.3}$$

If the attenuation barrier is large, the transmission coefficient can be expressed as

$$T \approx \frac{16k^2\kappa^2}{(k^2+\kappa^2)^2} e^{-2\kappa a} \tag{2.4}$$

Herein, the transmission coefficient has an exponential decay inside the barrier depending on the width of barrier.

Therefore, the tunneling current could be expressed as

$$I_t = A * e^{-2\kappa a} = A * \exp\left[-2\frac{\sqrt{2m(V_0-E)}}{\hbar} a\right] \tag{2.5}$$

where A is a constant.

This equation shows the probability of an electron transferring through a potential barrier larger than its own energy, generating tunneling current between two solid surfaces. The tunneling current has an exponential dependence on the width and height of the barrier.

The generation of a net tunneling current for the scanning tunneling microscopy is depicted in figure 2.4. The STM is assumed to be a metal-vacuum-metal system, the potential barrier could be thought as the vacuum level of the metal. For the electrons at Fermi level, the workfunction Φ stands for the minimum energy barrier to overcome. In figure 2.4A, the tip and sample have the same vacuum level and are not in tunneling contact, therefore, there is no tunneling current to generate. When tip and sample are in tunneling contact (Figure 2.4b), their Fermi levels are equal. It means that there is no bias voltage to be applied. When a positive bias voltage is applied to the sample (Figure 2.4C), its energy level shifts down, leading to a tunneling current. Similarly, a negative bias voltage on the sample will lead to a tunneling current in opposite direction (Figure 2.4D).

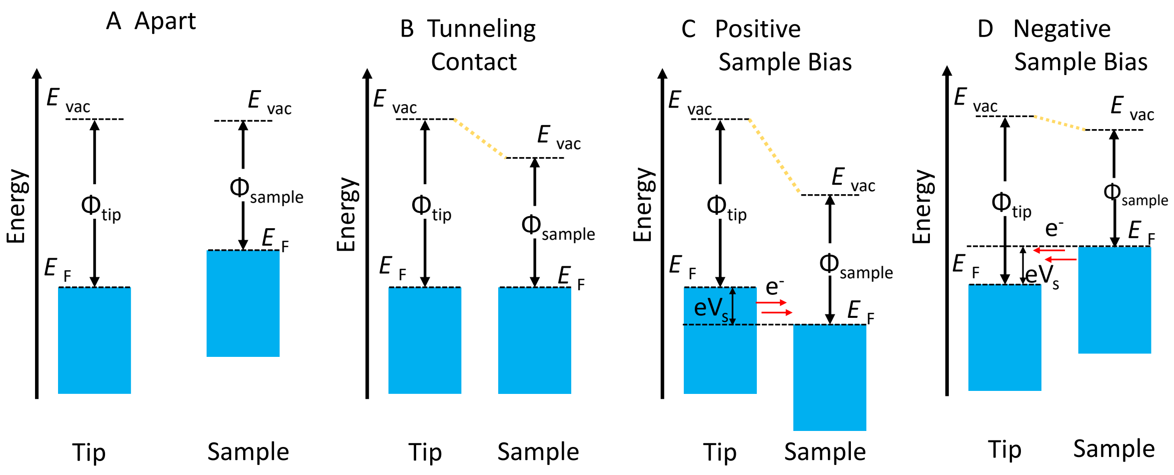

Figure 2.4: Energy levels diagram shows tunneling current between tip and sample: (A), they are not in tunneling contact and the same vacuum energy level; (B), they are in tunneling contact, and the fermi levels (E_F) of the tip and the sample are aligned; (C), they are tunneling contact, positive sample bias is applied to the sample, the Fermi level of the sample shifts down, a net flow of tunneling electrons from the filled states of the tip through the vacuum barrier into the empty states of the sample. (D), they are in tunneling contact, negative bias is applied to the sample, the Fermi level of the sample shifts up, a net flow of tunneling electrons from the filled states of the sample through the vacuum barrier into the empty states of the tip. The net flow of tunneling electrons are marked as red arrows.

Furthermore, Bardeen [43] introduced more precise solutions of the exact Hamiltonian for the time-dependent cases. In the equation, the tunneling current between two electrodes (tip and surface in the STM) is described with:

$$I_t = \frac{2\pi e}{\hbar} \sum_{t,s} \{ f(E_t) \cdot [1 - f(E_s - eV_b)] - f(E_s - eV_b) \cdot [1 - f(E_t)] \} \cdot |M_{ts}| \cdot \delta(E_s - E_t) \qquad (2.6)$$

where $f(E)$ is the Fermi distribution, V_b is the sample bias [40], M_{ts} is matrix of tunneling element between the states ψ_t of the tip and the states ψ_s of the sample surface, E_t and E_s are the eigenvalues of ψ_t and ψ_s, respectively. For small bias voltage (V_b), the tunneling matrix could be written as

$$M_{ts} = \frac{-\hbar}{2m} \int (\psi_t^* \nabla \psi_s) \cdot \mathrm{dS} \tag{2.7}$$

where S is the surface area within the barrier. If the temperature is low, the tunneling current can be expressed as

$$I_t = \frac{2\pi e^2}{\hbar} V_s \sum_{t,s} |M_{ts}|^2 \cdot \delta(E_s - E_F) \cdot \delta(E_t - E_F) \tag{2.8}$$

Depending on Tersoff and Hamann's theory [40], if considering the tip as a spherical potential with a radius R, r_0 stands for the center of the curvature of, the tunneling current could be expressed further:

$$I_t \propto V_b \cdot \rho_t(E_F) \cdot \exp\left(2 \frac{\sqrt{2m\Phi_t}}{\hbar} R\right) \sum_V |\psi_s(\mathrm{r}_0)|^2 \cdot \delta(E_s - E_F) \tag{2.9}$$

where Φ is workfunction, ρ_t (E_F) is the density of states (DOS) of the tip at Fermi level.

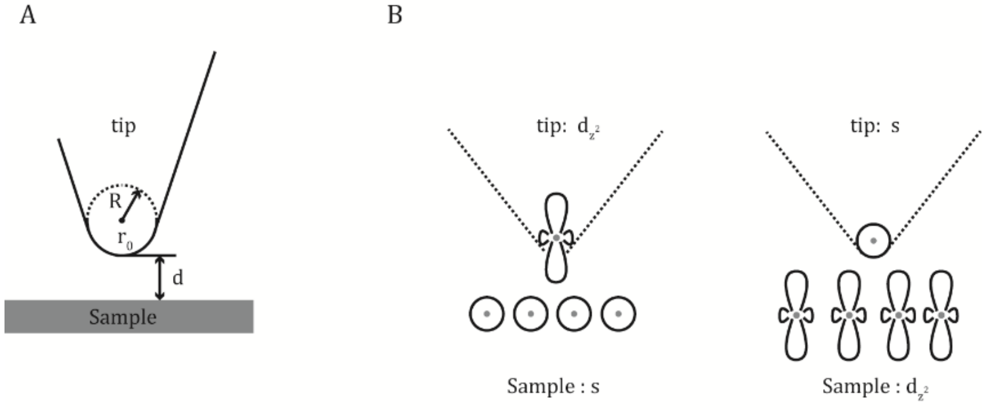

Figure 2.5: The size and the DOS ρt (EF) of the tip. (A) Tersoff-Hamann approximation of s-type tip. (B) Description of reciprocity principle. The tunneling process is the same that a d_{z^2}-wave tip scans over an s-wave surface or an s-wave tip scans over a d_{z^2}-wave surface.

Totally, the tunneling current depends on the applied bias voltage, the distance between tip and sample, the size and the DOS ρ_t (E_F) of the tip. Therefore, the STM image can be seen as a convolution of topographic and electronic information. For example, Chen [44] introduced the reciprocity principle showing that if the tip and sample states were interchanged (Figure 2.5B), the observed image would still be the same. Most of the STM tips made by W or PtIr etc. have a *d* band electrons. An s-wave tip scanned over a d_{z^2}-wave surface resulted in atomically resolved corrugation as simulation, in accordance with the atomic resolution observed in experimental results. Chen also noted the importance of knowing the nature of the tip apex atom (tip termination), when estimating the maximum corrugation of an STM image.

2.1.2 Scanning modes

In STM, the tip mounted on the piezoelectric tube could move with high accuracy in x-y-z position under precise voltages to deform the piezo (Figure 2.6). In the experiments, the tip gradually approached to the surface and starts to scan the sample once the tunneling current is recorded.

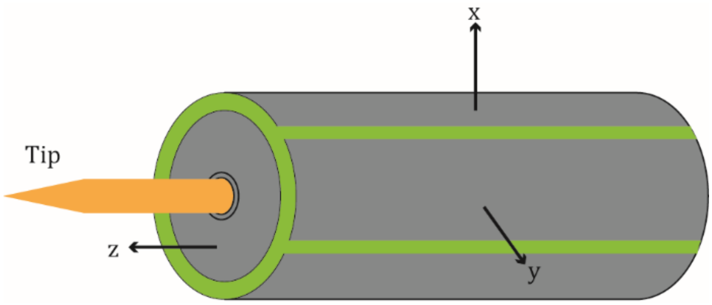

Figure 2.6: Schematic a piezo tube scanner. The scanner can provide 3 dimension motion with the tip.

During measurement of the tunneling current, two important scanning modes are classified: constant current mode (the most common scanning mode) and constant height mode (Figure 2.7).

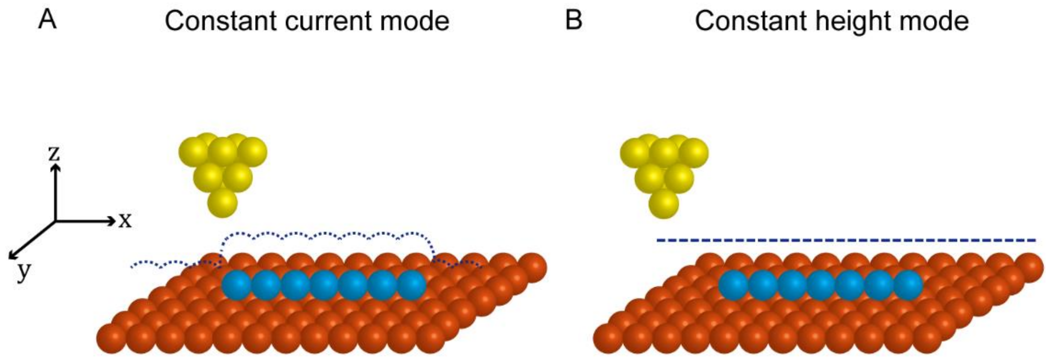

Figure 2.7: Illustration of two scanning modes in scanning tunneling microscopy: (A) constant current mode and (B) constant height mode.

In the constant current mode (Figure 2.7A), a constant tunneling current will be set, the tip scans the sample line-by-line in two dimensions against x and y positons. If the tunneling current deviates from the set point, the control system will send a signal to the piezo to adjust the height of the tip. A topographic image is obtained through recording the movement of the tip in the z direction. Different apparent height can be recorded due to the different local density of states of surface atoms.

In the constant height mode (Figure 2.7B), the height of the tip above the surface is constant, while the tunneling current is recorded. During the measurement, the tip scans over the surface in x-y positions, obtaining the current tunneling. The advantage of this mode is that it can be applied at a high scanning speed. The disadvantage is that it can be only used for atomically flat surface, otherwise the tip may crash onto the surface or lose the tunneling contact.

2.1.3 Experimental set-up

To keep the sample free of contaminations during the sample preparation and investigations, all the STM experiments in this thesis were performed in an UHV chamber (designed by Alexander Weber-Bargioni) equipped with a commercial variable-temperature STM (Aarhus 150 SPECS, Surface Nano Analysis GmbH [45, 46]), which is depicted in figure 2.8. The STM system consists of a preparation chamber and analysis chamber which contains the VT-STM, with a gate valve to separate. The sample can be transferred from UHV chamber to air without breaking the vacuum through the load-lock. The lateral manipulator d can be used to transfer the sample between preparation and STM chamber. The sample can be transferred with manipulator h from the preparation stage to the lateral manipulator in the preparation chamber. Manipulator l is located in STM chamber.

Ultra-High Vacuum

The whole ultra-high vacuum system is maintained by a series of connected pumps. A rotary pump is used to achieve the pressure of about 10^{-3} mbar. It is indispensable for the first turbo-molecular pump running, which can decrease the pressure further to 10^{-6} mbar. The main turbo-molecular pump (Figure 2.8g) installed at the preparation chamber is used to achieve the pressure around 2×10^{-10} mbar. The turbo-molecule pump is widely utilized to maintain high vacuum in the range of 10^{-10} mbar [47]. Its working principle is to impart momentum to the gas molecules in a designed direction: the very fast rotating fans collide with the molecules repeatedly from the inlet of the pump towards the outlet of the pump. Finally, an ion getter pump mounted at the STM chamber could maintain the low pressure by ionizing and accelerating ions and capturing them on a solid electrode.

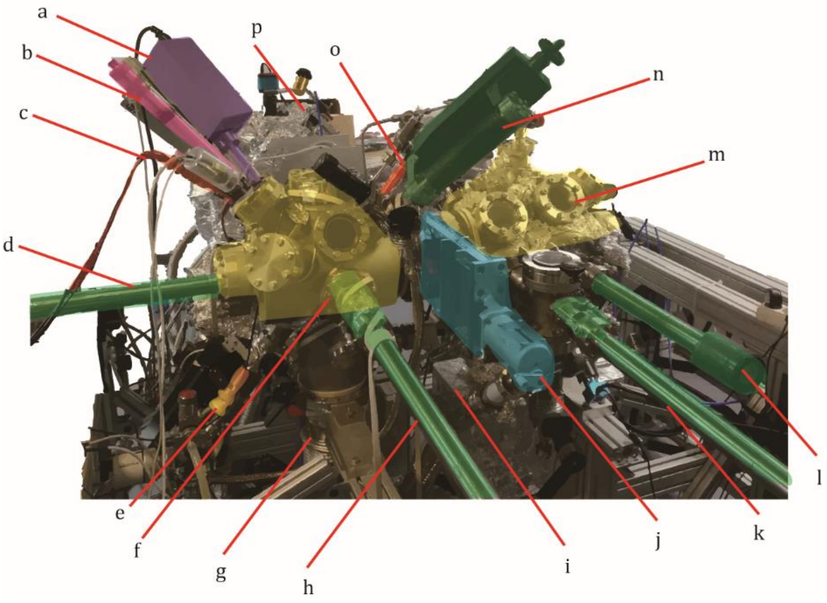

Figure 2.8: Image of the apparatus of the variable-temperature of STM under ultra-hgih vacuum. (a) mass spectrometry, (b) sample parking stage, (c) high voltage for annealing sample, (d) lateral manipulator, (h, j, l) the manipulator for preparation chamber, load lock, STM chamber separately, (e) an OMBE, (f) preparation chamber, (g) turbo-molecule pump, (i) ion pump (j) gate valve, (m) STM chamber, (n) metal evaporator, (o) sputtering gun, (p) chamber of Temperature programmed desorption.

Preparation Chamber

The preparation chamber contains a sample parking stage, a mass spectrometer, a sputtering gun, a metal evaporator and an organic molecular beam epitaxy (OMBE). In this chamber, substrate cleaning and molecules/metal depositions can be performed. There is a gate valve to separate preparation and STM chamber, while the normal operation in preparation chamber would not affect the pressure of STM chamber.

Metal crystal preparation. All of the molecules what we studied in this thesis are deposited on Au, Ag, Cu single crystals with a (111) surface orientation. Au(111), Ag(111) and Cu(111) have a face centered cubic (*fcc*) structure with the distance between the nearest atoms of 2.88 Å, 2.89 Å and 2.56 Å respectively. The crystals were fixed on a sample holder shown in figure 2.9. Atomically clean and flat single crystal surfaces are very important for the experiment. All the single crystals are cleaned by several cycles of argon ion sputtering and annealing. This procedure is summarized as following. Firstly, open the leak valve and fill the preparation chamber with Ar with a pressure of 2×10^{-5} mbar. (The purity of Ar is regularly checked with the mass spectrometer installed on the preparation chamber.) Then Ar atoms are ionized into Ar^+ and accelerated by the sputtering gun with an energy of 1 kV and emission current of 10 mA to bombard the target surface. The top atomic layers of the surface will be ejected due to collisions with the higher energetic Ar^+ leading to a rough surface. Therefore an annealing process is necessary, which causes high mobility of surface atoms so that they will rearrange into energetically favorable larger flat terraces. The annealing temperatures for Au(111), Ag(111) and Cu(111) are 650 K, 700 K and 770 K respectively. The cycles of sputtering and annealing are repeated until large clean and flat areas form, as examined by STM. After getting the desired surface, the molecules could be deposited from OMBE.

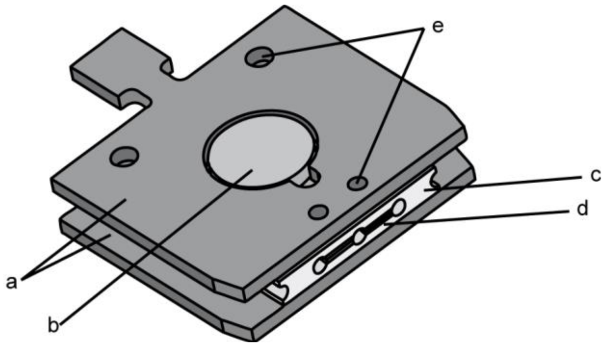

Figure 2.9: Image of the metal sample holder. (a) Molybdenum plates, (b) single crystal, (c) insulating ceramic piece, thermocouple wires, (e) screws [48].

Organic molecular beam epitaxy (OMBE). The OMBE (Figure 2.10) contains four quartz crucibles, which cab be heated independently by means of integrated tungsten filament and measured the temperature. The molecules are placed into the crucibles and sublimated onto the cleaned single crystal at a predefined temperature.

Figure 2.10: Image of OMBE with 4 independent crucibles, from *Dodecon Nanotechnology GmbH*.

Metal evaporator. Deposition of high purity of Co and Fe (about 99.995%) on the surface is carried out by the home-made metal evaporator (Figure 2.11), which is installed onto the preparation chamber.

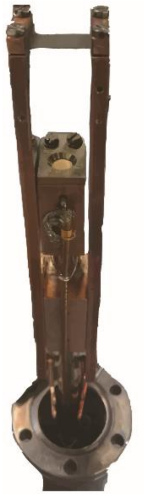

Figure 2.11: Image of home-built metal evaporator.

Analysis Chamber

The variable-temperature STM was fixed in the analysis chamber, which is separated by a valve gate from the preparation chamber. The investigations of STM were performed in a temperature range of 93 K to 300 K. Figure 2.12 shows the sample (1) into a single plate molybdenum sample holder (2), which is fixed by two springs (3). The quartz balls (10) separate the top part with the STM scanner thermally and electrically, and the top plate with the scanner is mounted on an aluminum block which could be cooled down to 93 K by liquid nitrogen or heated up to 470 K by two Zener diodes. The tip (4) is held by the tip-holder (5) which is fixed on the top of the scanner tube, together with the SiC rod and piezo motor form a system of inchworm motor. By applying suitable voltages to the inchworm motor with piezo elements, the tip can coarsely approach to sample surface with high precision in a tunneling distance,. Once the tip approached to the tunneling distance and scanning is initiated, the piezo system will receive the signal of feedback loop to keep a constant current. The Zener diode could keep the scanner at room temperature when investigating the sample at low temperature. The whole STM system is suspended by springs during investigation in order to shock absorptions from the outside, also combined with four damping pumps.

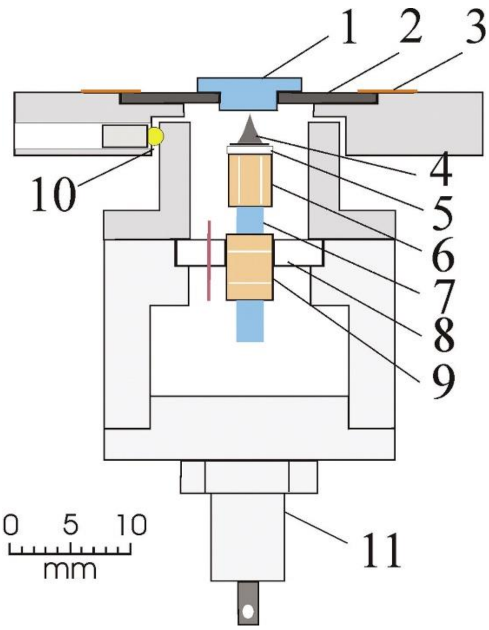

Figure 2.12: Schematic of Aarhus 150 VT-STM.(1) Sample, (2) Tantalum sample holder, (3) Clamps, (4) Tip, (5) Tip holder, (6) Scanner tube, (7) SiC rod, (8) Mount inchworm motor, (9) Piezo motor, (10) Quartz balls, (11) Zener diode for possibility of tip heating [46].

Tungsten tips are used for all the experiments in this thesis. The tungsten wire with a diameter of 0.25 mm is immersed into 2M NaOH solution, then processed through electrochemical etching by applying 2.5 V - 3.5 V DC between the aluminum cathode and the anode of tungsten wire (Figure 2.13). The related electrochemical reaction is:

$$W_{(s)} + 8\ OH^{-} \rightarrow WO_4^{2-} + 4\ H_2O + 6\ e^{-}$$

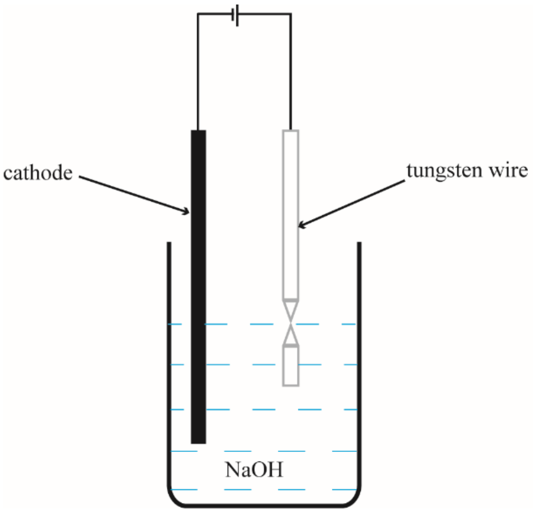

Figure 2.13: Sketch of the etching process of tungsten tip.

Deionized water is used to clean the tip after etching. The tip is stable in exposure to air due to the formation of a thin oxide layer on surface. Then, the tip is mounted onto the STM scanner, and the oxide layer will be removed through bombardment of argon ions during a sputtering process.

2.1.4 Sample preparation

The clean metal crystals are kept at room temperature during the deposition of molecules from the OMBE and metal atoms from the metal evaporator. The molecule temperature and duration of the deposition depend on the properties of molecules and the expected coverage. The heating temperatures used for the deposition of different molecules are listed in table 2.1. Then the sample could be transferred into STM chamber for characterization. The WSxM software [49] is used to analyze the images.

Table 2.1: Details of molecules investigated in this thesis and related deposition temperatures.

Molecule	**Purity**	**Sublimation temperature**	**Synthesized by**
1,3,5-tri-benzonitrile imidazole (TCPI)	≥ 99%	440 K	G. Médard (Proteomics and Bioanalytics, TUM)
4,4´-biphenyl dihydroxamic acid (BPDH)	≥ 99%	463 K	G. Médard (Proteomics and Bioanalytics, TUM)

2.2 X-ray photoelectron spectroscopy (XPS)

2.2.1 Principle of XPS

We can observe the topography of the molecules on surface from the results provide by STM, such as the self-assembled or metal-coordinated structures, phase transformations and so on. However, STM can not provide chemical information. Therefore, it’s necessary to combine with another surface analysis technique for obtaining the critical information of the chemical state of molecules to further analyze the formed nanostructures. XPS (X-ray photoelectron spectroscopy) is a powerful tool to determine the elemental composition, chemical bonding, and electronic properties of surfaces, whereas soft X-rays have also high surface sensitivity. The theory of XPS is based on the photoelectric effect, which was discovered by Heinrich Rudolf Hertz in 1887, explained by Albert Einstein in 1905. When X-rays (photons) with sufficient energy (hv) (usually in a range of 200~2000 eV) irradiate the sample's surface, electrons can be excited to escape from the sample, which can be detected by an electron analyzer. The binding energy of the ejected electron is given by:

$$E_b = hv - E_k - \phi_s \tag{2.10}$$

Here ϕ_s is the work function (energy required that photoelectrons escape from the Fermi level to free vacuum level) of the spectrometer and E_k is the kinetic energy of photoelectron, as illustrated in figure 2.14.

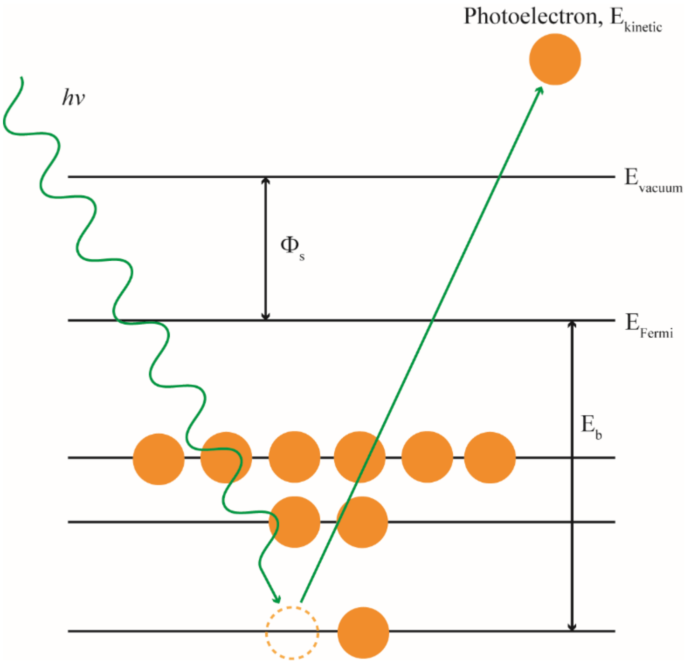

Figure 2.14: Core electrons are excited by X-ray radiation. And the kinetic energy of the photoelectron is detected by energy analyzer.

When the photoelectron escapes from the solid surface, electrons located on the top layer and inside in the bulk will travel through different paths. On the top layer, the electrons can escape without losing energy owing to the lack of inelastic collisions, while electrons located inside will go through inelastic collisions, and will lose kinetic energy. Therefore, in figure 2.15, the universal curve of inelastic mean free path (a photoelectron goes the average distance during collision in solid bulk) and data of different materials are shown as a function of the kinetic energy. Electrons with higher kinetic energy than ~ 50 eV will have longer free paths. Approximately 95% of XPS signals come from the electrons located on the top layer [50].

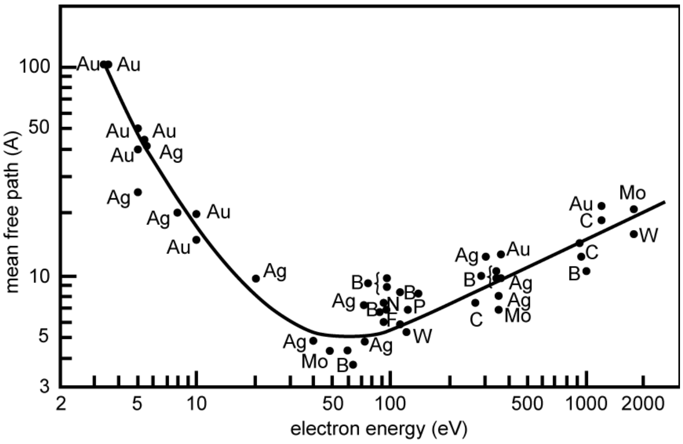

Figure 2.15: Graph of inelastic mean free path versus the kinetic energy of the photoelectron[50].

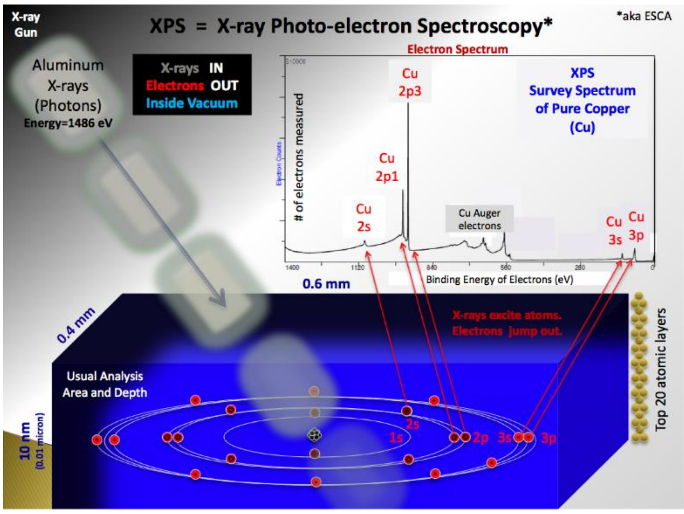
X-ray
Gun
XPS = X-ray Photo-electron Spectroscopy*
*aka ESCA
Aluminum
X-rays
(Photons)
Energy=1486 eV
X-rays IN
Electrons OUT
Inside Vacuum
Electron Spectrum
# of electrons measured
Cu
2p3
Cu
2p1
Cu
2s
Cu Auger
electrons
Cu
3s
Cu
3p
XPS
Survey Spectrum
of Pure Copper
(Cu)
1400
1120
840
560
280
0
Binding Energy of Electrons (eV)
0.6 mm
0.4 mm
X-rays excite atoms.
Electrons jump out.
Usual Analysis
Area and Depth
10 nm
(0.01 micron)
1s
2s
2p
3s
3p
Top 20 atomic layers

Figure 2.16: Working principle of XPS. (https://en.wikipedia.org/wiki/X-ray_photoelectron_spectroscopy)

In the XP spectra, the binding energy is characteristic of the element. The chemical and electronic structures of elements can affect the binding energy in result of small shifts. Such shifts of the peak of binding energy are called chemical shifts due to different electronic environments of the escaped electrons. Valence electrons and the bonds formed between neighboring atoms will cause the chemical shifts resulting into differences in the peak centers. When the core electrons exist in an outer-electron-poor environment, the binding energy will increase due to the positive charge having an attraction to the core electrons. While the core electrons in an outer electron-rich environment, it will exhibit a decrease of binding energy. In the process of photon emission, the Auger electron always accompanies with the first ordered photoelectrons (Figure 2.16). After the primary excitation and creation of an electron vacancy, de-excitation can occur with an electron from an occupied higher energy level filling the vacant core level and another electron (called as Auger electron) of higher energy being excited to the vacuum. The kinetic energy of Auger electron is characteristic for the energy levels of the atom (so of the material) and is not effected by the excitation energy.

2.2.2 Experimental set-up

All of the XPS experiments are carried out on a commercial UHV equipment (SPECS) at the TUM-WSI lab in Garching (Figure 2.17). The pressure of analysis chamber is about 2×10^{-10} mbar supported by the similar pump system as that of STM. The preparation chamber is equipped with a sputtering gun. An OMBE and metal evaporator are installed for our in-situ sample preparation. The cleaning process of the substrate follows the protocol described in the STM part.

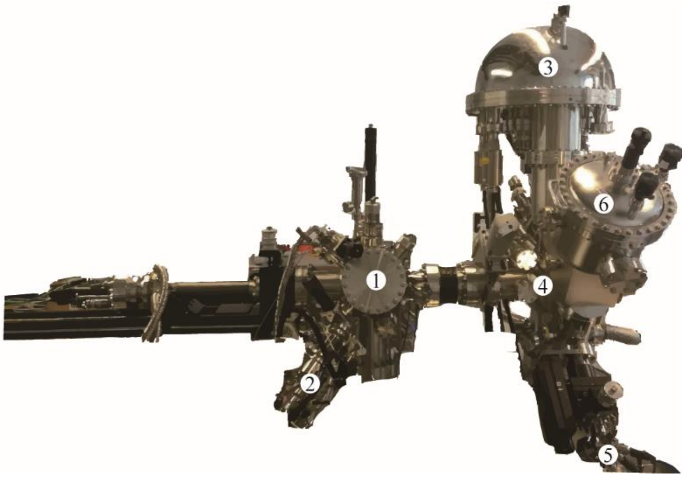

Figure 2.17: Image of the XPS setup of TUM-WSI in Garching.(1) preparation chamber, (2) organic molecular beam epitaxy, (3) PHOIBOS 150 hemispherical energy analyzer, (4) analysis chamber, (5) XR 50 X-ray source (SPECS GmbH), (6) FOCUS 500 X-ray ellipsoidal monochromator (SPECS GmbH).

We use the XR 50 X-ray source which gives monochromated Al Kα radiation ($h\nu = 1486.74$ eV). Equipment of water-cooling system on the energy source could keep the increase of the temperature of the anode by less than 5 K during long-term operation. The ellipsoidal monochromator works based on Bragg diffraction, which is depicted in figure 2.18. The wave of X-rays is reflected by the single quartz crystal mirror fixed at a specific angle, so that the X-ray wave could focus on the sample perfectly. The large surface area of the crystal results in high efficiency of reflection. The photoelectrons are then detected by the

PHOIBOS 150 analyzer, and the well-designed computer simulations could characterize and optimize the electron optical properties of the analyzer and transfer lens system.

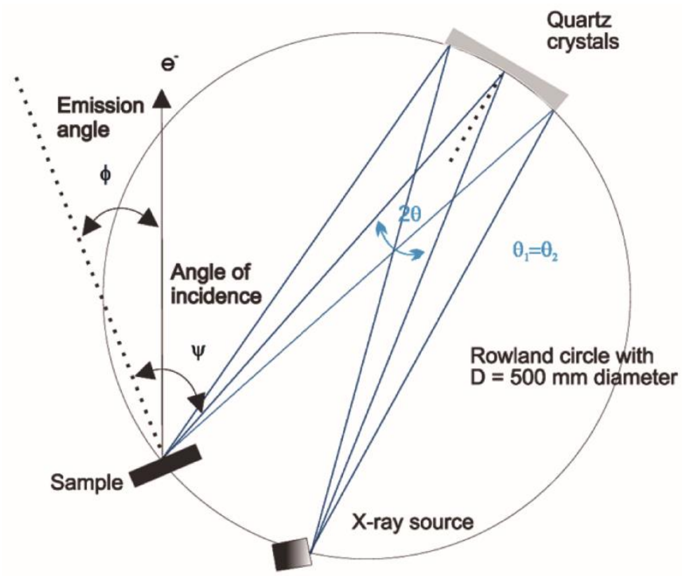
Quartz
crystals
e-
Emission
angle
ϕ
Angle of
incidence
ψ
2θ
θ1=θ2
Rowland circle with
D = 500 mm diameter
Sample
X-ray source

Figure 2.18: Basic working principle of the ellipsoidal monochromator FOCUS 500 (from SPECS GmbH).

In the experiments, main signals of C 1s, N 1s, O 1s and Co 2p$_{3/2}$ are reported. Their binding energies are calibrated against the substrate core level peaks: Ag 3d$_{5/2}$, Au 4f$_{7/2}$, or Cu 2p$_{3/2}$ at 368.3 eV, 84.0 eV and 75.1 eV, respectively. The liner, Shirley and polynomial background is subtracted from the raw data. The core level peaks are fitted with the Voigt functions.

3. On-surface assembly of a chemiluminescent module: porous and densely packed structures by simultaneous expression of different metal coordination motifs

A series of non-covalent interactions, such as hydrogen bonding [51-53], dipolar interactions [54-56] and metal-organic coordination [57] have been used into the synthesis of organized nanostructures. Compared to other non-covalent interactions, metal-organic molecular nanostructures are stable and flexible [58-60] so that fabrication of highly organized two-dimensional metal-organic structures, which comprise metal cores and various functional ligands on a metal surface has attracted tremendous interest over the past few years [61-64], with potential applications including sensors, solid catalysis, and electronic [65-70].

Lophine (2,4,5-triphenyl-1H-imidazole, **1**, Scheme 3.1) and its derivatives are of interest owing that their wide application in chemiluminescence, fluorescence, and bioanalytical tools [71-73]. These stem from the oxidation of the imidazole core by oxygen in the presence of strong base to form diaroylamidines resulting in light emission [74-76].

Scheme 3.1: Lophine 1 and the carbonitrile functionalized lophine (TCPI) 2 used here.

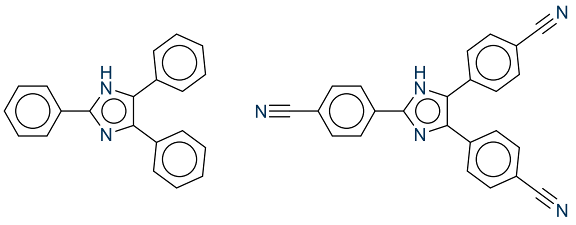

1 **2**

To expand the application of lophine derivatives, various functional groups could decorate the phenyl rings including –H, -OH, -NO_2, -CN [77-79]. Such functionalities can result in ordered surface nanoarchitectures different from those in bulk and have the capacity for on-surface coordination with metal adatoms. Moreover, the fabrication of the precise nano-structures of lophine derivatives on surfaces could fulfill its potential applications better, for example, as a sensitive layer for the detection of dissolved oxygen [80].

Hitherto, cyano substituted molecules have been intensely studied on surfaces. The unbalanced charge distribution of the carbonitrile group ensues in strong dipole force, which can form dipolar couplings with other functional groups, and most importantly they can coordinate with transition and lanthanide metals to fabricate well defined coordination architectures [81]. Herein, we aim to combine the functionality of the lophine with the directional supramolecular assembly enabled by carbonitrile linkers, therefore 2, 4, 5 - tri (4-cyanophenyl) imidazole (TCPI) 2 (Scheme 3.1) comprising of an imidazole core and with three symmetrical cyanophenyls was de novo synthesized. By means of scanning tunneling microscopy (STM) and X-ray photoelectron spectroscopy (XPS) we investigated its self-assembly and metal adatom coordination on three different single crystal metal surfaces, namely on the (111) close packed faces of Au, Ag and Cu.

3.1 Self-assembled structures of TCPI on Ag(111)

An *ab initio* energy optimization of the isolated TCPI structure found two atropisomers as global minima, one structure is presented in figure 3.1A.

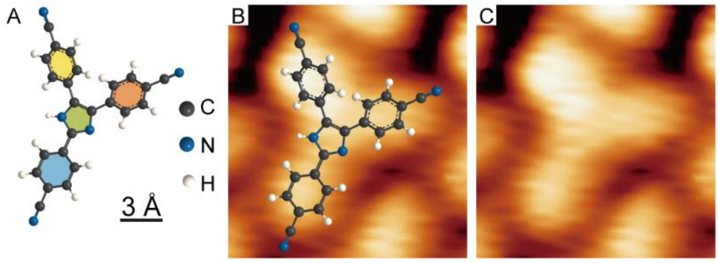

Figure 3.1: Molecular model and STM image of TCPI. (A) Top view of TCPI (2) ball-and-stick model: The highlighted area on the phenyls are physically protruding from the plane of the imidazole (B-C). STM image zoom in a single molecule with proposed molecular conformation overlaid in B (U_s = 1.74 V, I_t = 0.08 nA, recorded at 298 K).

In STM image, individual molecule is imaged as separate asymmetric trilobed protrusions (Figure 3.1B-C), matching the shape resulting from a roughly parallel adsorption to the Ag plane (Figure 3.1C). One of the lobes appears brighter, indicating that a tilt angle of the more upstanding phenyl moiety (yellow in figure 3.1A) is (partially) preserved upon adsorption to the Ag surface, whereas no significant variation is observed in the apparent height of the other three rings.

The STM overview of the TCPI on Ag(111) after room temperature deposition is depicted in Figure 2A. We found that the molecules formed long range close packed self-assembled structures described by the unit cell shown with the green parallelogram in Figure 2C. Within the accuracy of our measurement (~5%) the overlayer can be described by the point-on-line epitaxial matrix $\begin{bmatrix}3.5 & -1\\ 7 & 9\end{bmatrix}$. Each unit cell contains two antiparallel TCPI molecules. A molecular model can be proposed for this self-assembled structure based on maximizing the attractive molecule-molecule interactions. In such a model stabilization is achieved by dipolar coupling of terminal cyano groups (green oval in figure 3.2B) [82], attractive interactions between cyano groups and phenyl rings (orange oval in figure 3.2B) [83] and -NH···NC- hydrogen bondings with a projected distance of ~ 1.8 Å (green oval in figure 3.2B).

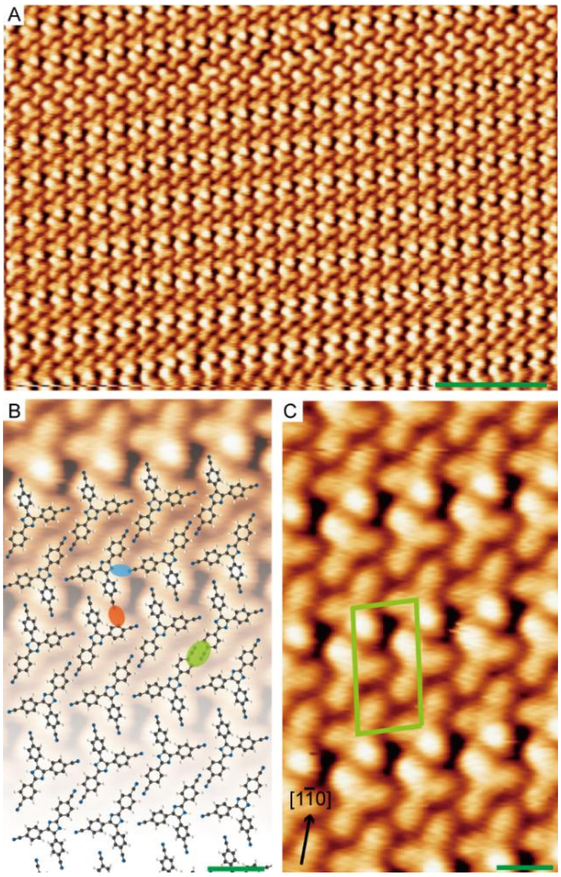

Figure 3.2: STM image of self-assembled structure on Ag(111). (A) Large-scale STM image of self-assemble structure on Ag(111) (U_s= 1.74 V, I_t = 0.10 nA, recorded at 298 K), the scale bar is 6 nm. (B) STM images

(U_s = 1.74 V, I_t = 0.08 nA, recorded at 298 K, scale bar is1 nm) of the molecular self-assembled structure on Ag(111) and overlaid partially with molecular model (C) The unit cell is outlined in green and a Ag high symmetry axis is indicated. A green, an orange, and a cyano oval mark two terminal cyano groups with dipolar coupling, a cyano group and a phenyl ring with attractive interaction, and a NH···NC hydrogen bond, respectively.

Subsequently, inspired by the unusual three-fold surface coordination of Co by cyano groups on the Ag(111) [84], we deposited Co atoms onto a submonolayer of TCPI. As shown in figure 3.3, there is scarce evidence of the Co atoms directing the molecular self-assembly in this case. Large areas of the afore described dense packed phase are visible, with the addition of Co related clusters. At the boundaries of the ordered dense packed islands, coordination three-fold and four-fold motifs of cyano groups by Co can be identified (molecular model overlaid in figure 3.3). This self-assembly scenario remained unchanged with increasing Co/TCPI stoichiometry. We note that it is possible for Co to be incorporated in the closed packed structure by coordination of the iminic N of an imidazole moiety and a cyano group of a neighboring molecule (see model in figure 3.3), instead of the formation of NH···NC hydrogen bond. This might alter the dimensions of the relevant unit cell, however on average there was no evidence of such a change within the accuracy of our STM measurements. Such a coordination motif is previously unreported on surfaces.

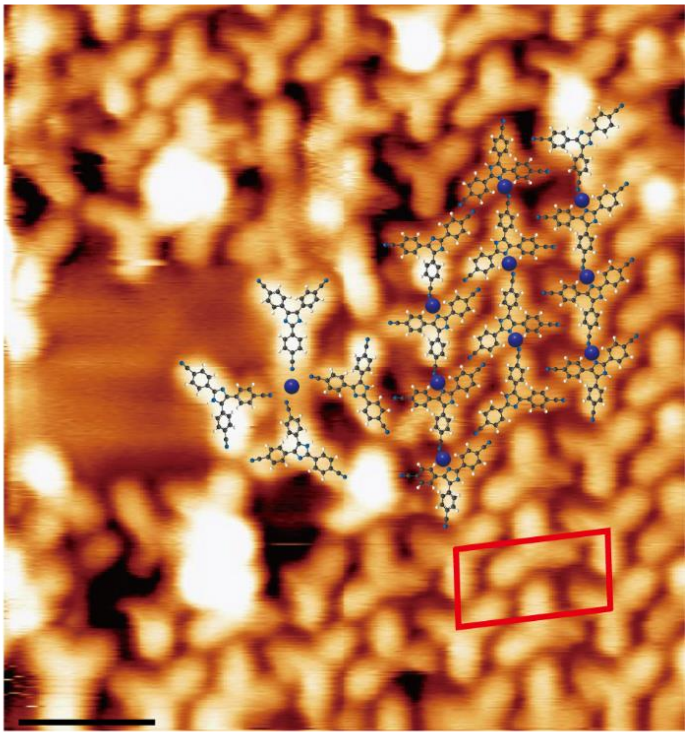

Figure 3.3: STM image of submonolayer of TCPI with addition of excessive Co on Ag(111) (scale bar = 2

nm, U_s= 1.40 V, I_t = 0.11 nA, recorded at 298 K) partially overlaid with proposed model (Blue spheres represent Co atoms). It shows 4-fold and 3-fold TCPI-Co coordination motifs on the boundary of a dense packed island (characteristic unit cell indicated in red). Very bright protrusions are assigned to Co related cluster.

3.2 Self-assembled structures of TCPI on Au(111)

Deposition of molecular monolayer on Au(111) formed the same self-assembled structure as on Ag(111), albeit with more defects at the island boundaries (Figure 3.4A). The same unit cell as that of on Ag(111) is marked by blue parallelogram in figure 3.4B.

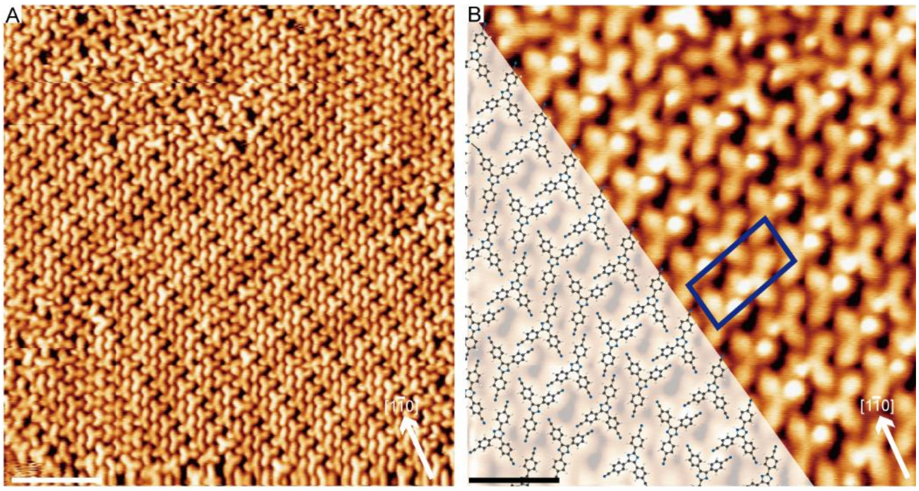

Figure 3.4: STM image of the molecules on Au(111) at room temperature. (A) The overview STM image of self-assembled structures of TCPI at room temperature (scale bar = 6 nm, U_s= 1.28 V, I_t = 0.07 nA, recorded at 298 K). (B) High resolution STM image of self-assembled structures of TCPI at room temperature (scale bar = 2 nm, U_s= 1.28 V, I_t = 0.11 nA, recorded at 298 K), the unit cell marked with blue parallelogram.

Cobalt directed self-assembly: However, following deposition of Co onto a submonolayer TCPI according to covered Au(111) at room temperature, we observed marked changes in the self-assembly scenario (Figure 3.5A). This self-assembly does not change significantly after annealing to temperatures up to ~ 363 K (Figure 3.5B). A microscopic close up (Figure 3.5) reveals the unambiguous formation of three main types of Co coordination nodes expressing simultaneously. The former are the expected and previously observed 3-fold and (rarely) 4-fold cyano coordination by Co adatoms. The latter is the previously proposed the cyano to iminic N of the imidazole coordinated by Co. The formation of this motif is supported by identifying that approximately 65% of the imidazole rings have cyano groups pointing towards iminic N, coexisting with a tiny of hydrogen bonding of CN-NH in the same area, as the NH of imidazole group keep intact during on surface, which could be proved by the following XP results (figure 3.7). Different metal coordination nodes at room temperature and after annealing were plotted in figure 3.5D. It was found that the dimer motifs increase, while the trimers decrease after annealing, which means that the CN-Co-$N_{imidazole}$ is preferential coordination compared with coordination of $(CN)_3$-Co. Furthermore, -NH of imidazole group still keep intact after annealing and this is consistent with the XPS data in figure 3.7C. For the case of the iminic N atoms of the imidazole such an interaction with the cyano atom can only be substantiated by the mediation of the supplied Co atoms and it is furtherly evidenced by XPS measurements, as discussed below.

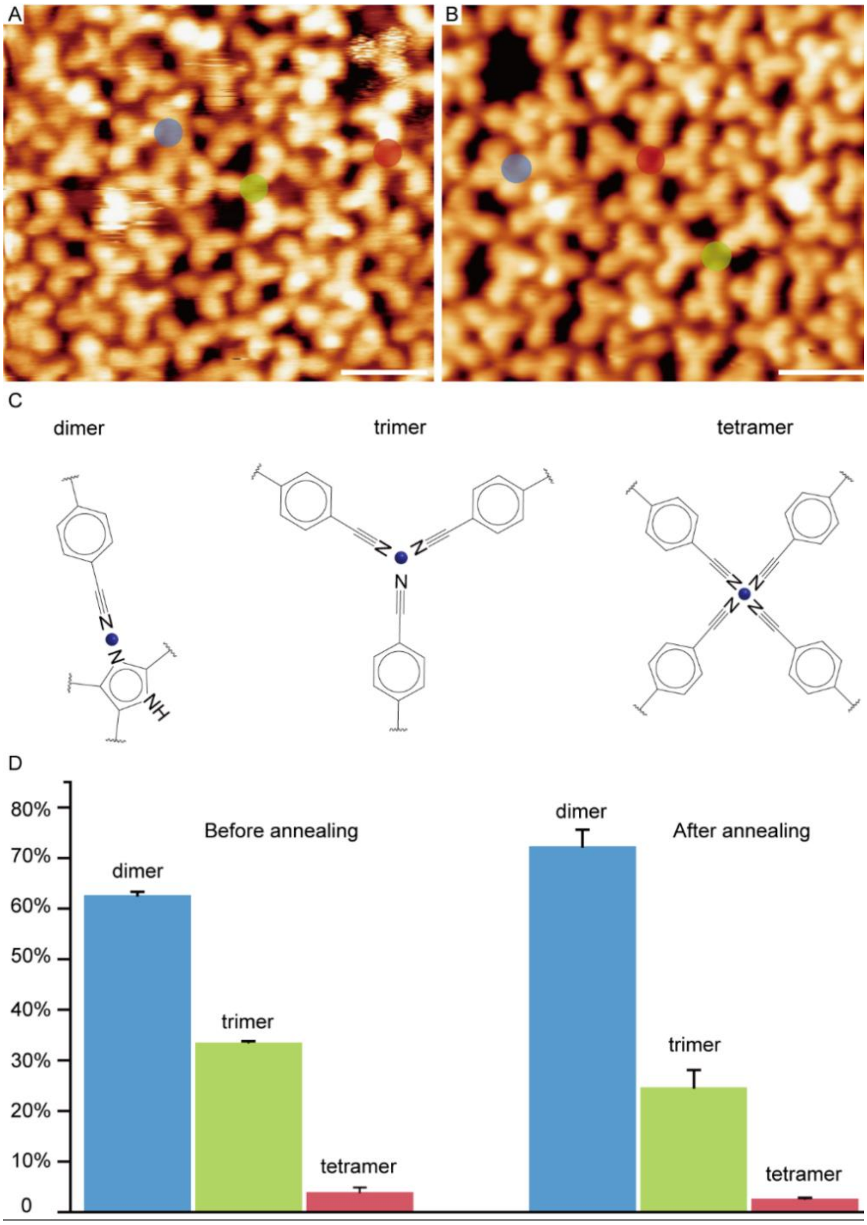

Figure 3.5: Structures of TCPI with Co atoms on flat surface. (A) STM image of the random metal-organic structure on surface (U_s= 1.25 V, I_t = 0.11 nA, recorded at 298 K) formed at room temperature. (B) STM image of the multi-metal-coordination structure on Au(111) after annealing (U_s= 1.25 V, I_t = 0.10 nA,

recorded at 298 K). Different coordination nodes are marked with colorful circle. Scale bar is 2 nm. (C) Corresponding metal-coordination models. (D) Histogram of different coordination motifs generated before and after annealing.

We further identified the formation of the coordination motifs via XPS. The Au $4f_{7/2}$ lines at 84 eV was used for the binding energy scale calibration. Shirley background was subtracted from the original XPS data, with Voigt functions to fit every component.

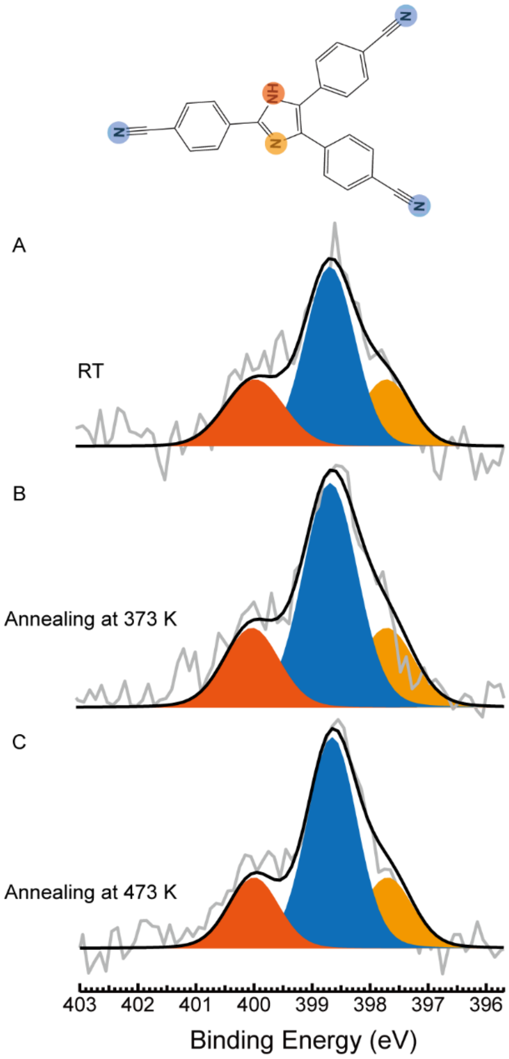

Figure 3.6: XPS measurement of N 1s of TCPI at RT on Au(111). (A) Monolayer of TCPI on Au(111) at RT, showing that the molecule keep intact during sublimation and deposition. (B) Annealing the monolayer at 373 K. (C) Subsequent annealing at 473 K.

The N 1s signal of the molecule (figure 3.6) in the monolayer is characterized by three peaks at 400 eV (orange), 398.67 eV (blue) and 397.7 eV (yellow). The peak of iminic N shifts to lower bonding energy compared with previous work [85], it could be due to surface charging effects. Their intensity matches the expected stoichiometric ratio of 1: 3: 1, and they are assigned to the imidazole aminic N, the cyano groups and the imidazole iminic N [86, 87]. We note that these signatures do not change noticeably even after annealing to temperatures up to ~ 473 K (figure 3.6). Should significant Au adatom to cyano coordination occurred (as reported for a different cyano functionalized molecule on Au(111) after annealing to 433 K) [88], we would have expected a shift of the respective component (blue) towards higher binding energy [89, 90].

The effect of addition of Co atoms onto a submonolayer coverage of TCPI in a 1.0 : 1.3 ratio of Co : TCPI on Au(111) on the N 1s signal is shown in figure 3.7. The ratio of Co : TCPI was calculated by comparing the individual component peak area (N 1s and Co 2p) / corresponding atomic subshell photoionization cross sections [91].

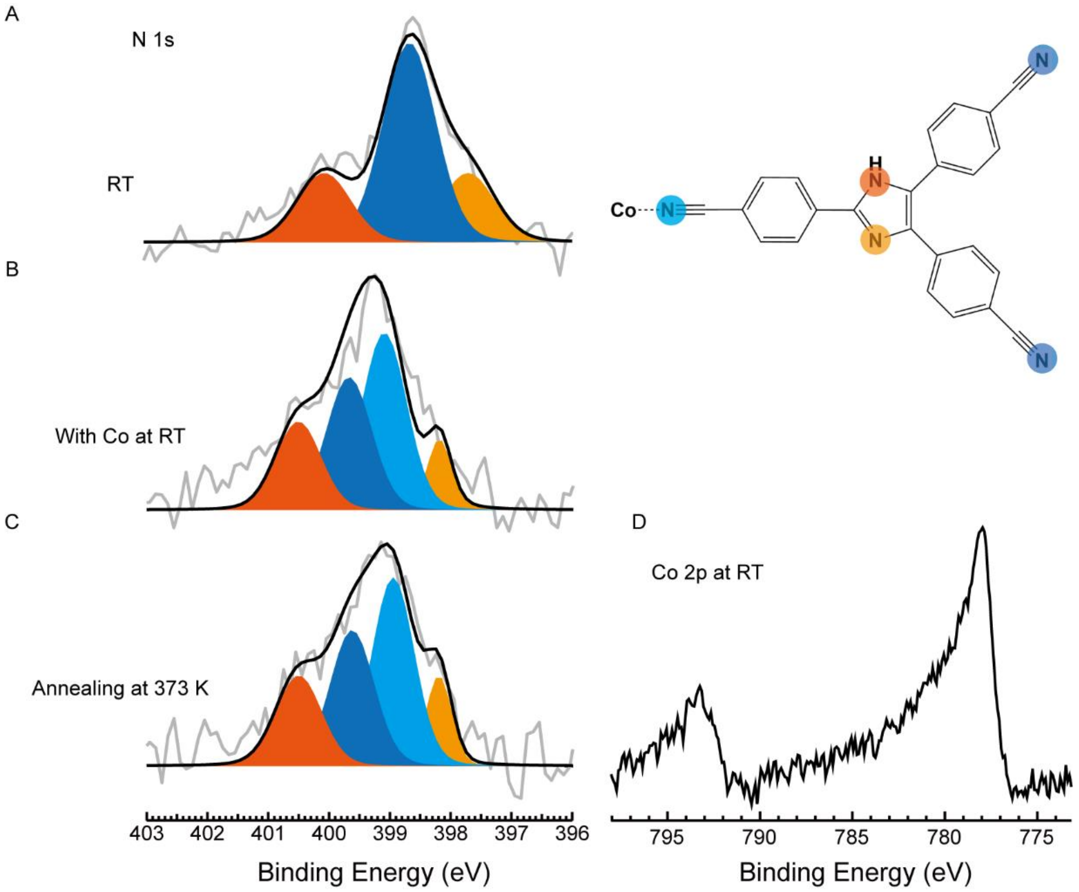

Figure 3.7: XPS measurement of N 1s and Co 2p at RT on Au(111). (A) Monolayer of TCPI on Au(111) at RT. (B) Adding Co onto the monolayer. (C) Annealing the blend of TCPI and Co at 373 K. (D) Co 2p spectrum for mixture of Co and TCPI on Au(111).

All peaks of the N 1s shift by 0.6 eV towards higher binding energy, caused by Co atoms, which is consistent with previous work [92]. The yellow component represents iminic N which do not form metal coordination bonding. The peak at 399.6 eV is ascribed to the CN groups, while the new component at 399.0 eV (light blue in Figure 7B) is attributed to terminal group CN coordinated with Co. With our assignment, consistent with previous work, the CN group showed that the coordination with Co lowers the binding energy by 0.6 eV [89]. Importantly the imidazole aminic N is also found upshifted by 0.5 eV (400.5 eV). This is consistent with the N maintaining its aminic character. The peak of Co $2p_{3/2}$ at 778.3 eV is typical value of Co (0) [93]. The downshift suggests an initial state effect, the electrons flow from Au substrate to Co atoms, reducing effective oxidation state of Co atom. Following annealing of the sample at 423 K, all of the peaks remain unchanged, which is consistent with the result concluded from the STM statistic data in figure 3.5.

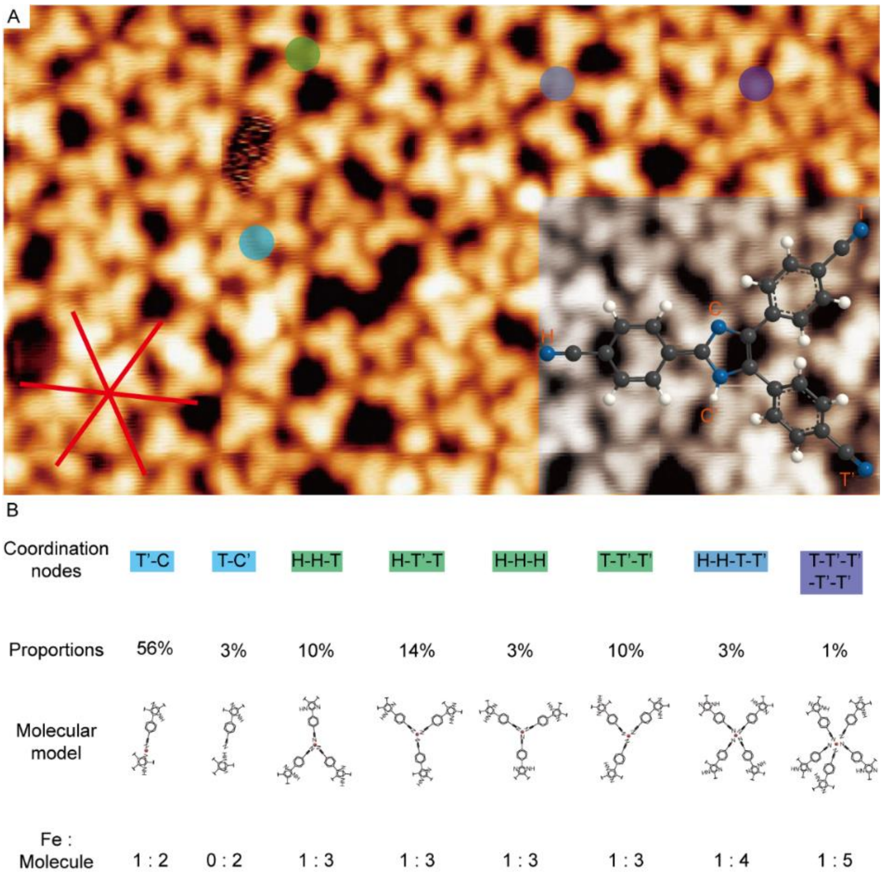

Figure 3.8: Blends of TCPI and Fe atoms on Au(111). (A) Annealing sub-monolayer of molecules dissolved by Fe atoms at 373 K on Au(111) (U_s= 1.68 V, I_t = 0.09 nA, recorded at 298 K). Scale bar is 4 nm. Different metal coordination nodes are marked with colorful cycles. (B) Distribution of TCPI coordination with Fe atoms.

***Iron directed self-assembly*:** Moreover, we investigated the effect of the change of the directing transition metal to Fe in the observed coordination motifs and resulting structures. This was achieved by deposition of Fe atoms on Au(111) which forms multiple reservoirs of Fe clusters on the plane terraces, due to the cluster nucleation at the elbows of the chevron reconstruction [94], which has been proven by previous research [95]. Addition of TCPI and annealing at 373 K, resulted structures are shown in the STM topography in Figure 3.8A. A detailed analysis of the coordination motifs shows the same distribution as observed with post-deposited Co (figures 3.5A, 3.5B, 3.8B). We therefore infer that on Au(111) with transition metal atoms to form the coordination structure.

3.3 Metal-organic structures of TCPI on Cu(111)

Deposition of submonolayer of TCPI onto Cu(111) at RT results in a close-packed structure with molecular density of 0.5 molecules nm^{-2} (figure 3.9A) different than the one observed on Ag(111) and Au(111). Within the structure we can identify trimers of TCPI (examples indicated in blue and in grey in figure 3.9A) forming by closing a loop of three N_{cyano}-Cu-$N_{imidazole}$ bonds. These coordinate to neighboring trimers with another three NH···N hydrogen bonds and three $(N_{cyano})_3$-Cu coordination bonds, which are labeled by green and light yellow circles in figure 10A. Interestingly in the competition between the cyano groups engaging in N_{cyano}-Cu-$N_{imidazole}$ bonds and $(N_{cyano})_x$-Cu bonds, we note that the former seem to be preferable: the maximum number of these bonds has formed by engaging in them all the surface $N_{imidazole}$ moieties. We therefore propose that a hierarchical fashion of self-assembly commencing with the formation of TCPI trimers, which self-assemble further in two-dimensional islands.

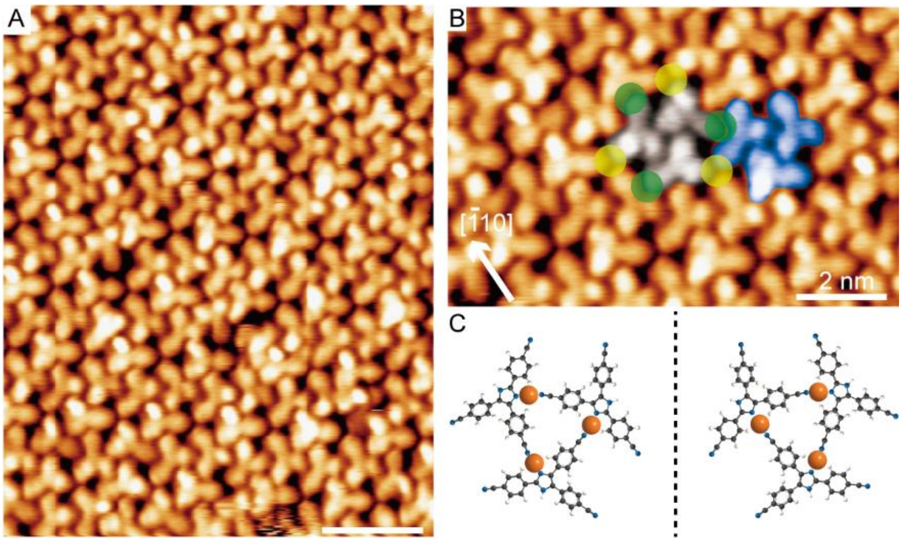

Figure 3.9: Self-assembled molecular structure of TCPI on Cu(111) at room temperature. (A) Large-scale STM image observed at room temperature (U_s= -1.44 V, I_t = -0.07 nA, recorded at 298 K). (B) High resolution

of STM image obtained at room temperature (U_s= -1.44 V, I_t = -0.07 nA, recorded at 298 K). The green and yellow circles stand for NH···N hydrogen bonds and three $(N_{cyano})_3$-Cu coordination bonds respectively. (C) Atomistic model of molecules on Cu(111).

The trimers exhibit organizational chirality and can be distinguished in *R* and *S* forms, shown in figure 3.9B. These are mixed on the self-assembled islands. Annealing the monolayer at 413 K for extended time results in islands of consisting solely of homochiral trimers as shown in figure 3.10B. The self-assembled structure is periodic with a unit cell of side length of 2.45 nm (marked blue line in figure 3.11B), which can be described by the epitaxial matrix $\begin{bmatrix} 9 & -2 \\ 10 & 9 \end{bmatrix}$.

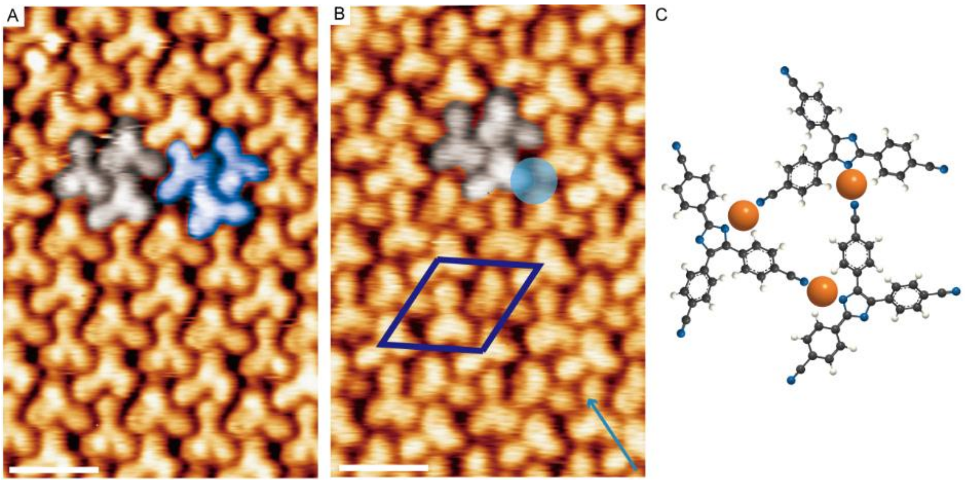

Figure 3.10: Annealing the monolayer of TCPI on Cu (111) from 363 K to 413 K. (A) The monolayer is annealed at 363 K (U_s= -1.40 V, I_t = -0.07 nA, recorded at 298 K). (B) Go on annealing monolayer at 413 K, kept 14 h (U_s= 1.40 V, I_t = 0.09 nA, recorded at 298 K). Scale bar is 2 nm. (C) Model of metal coordination structures, yellow spheres stand for Cu adatoms.

To validate our proposed models and to rationalize the ordering of the TCPI trimers to homochiral islands, we performed commentary XPS measurements of the N 1s region for a submonolayer TCPI coverage on Cu(111) (in figure 3.11 and 3.12). The Cu $3p_{3/2}$ line at 75.1 eV was used for the binding energy scale calibration. Shirley background was subtracted from the original XPS data, with Voigt functions to fit every component. Firstly, we performed XPS investigation of a molecular multilayer on Cu(111). After subtraction of a background of N 1s from TCPI monolayer on Cu(111), it is found that the area ratio of the N 1s three peaks is similar with that of monolayer (figure 3.12 A), the stoichiometric is 1 : 3 : 1 (aminic N /cyano N/iminic imidazole N). For submonolayer data, the aminic N remains intact at room temperature, forming the observed NH···N hydrogen bonds with neighboring molecules.

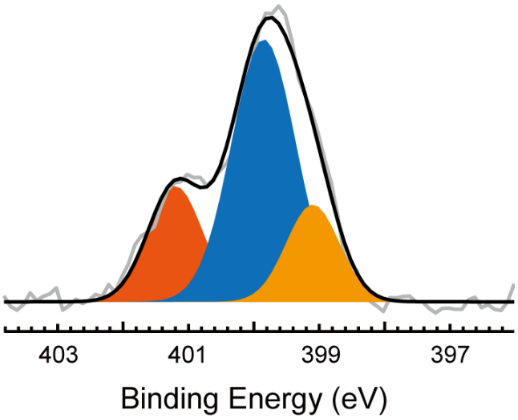

Figure 3.11: XP spectra of N1s for multilayer of TCPI on Cu(111) at room temperature.

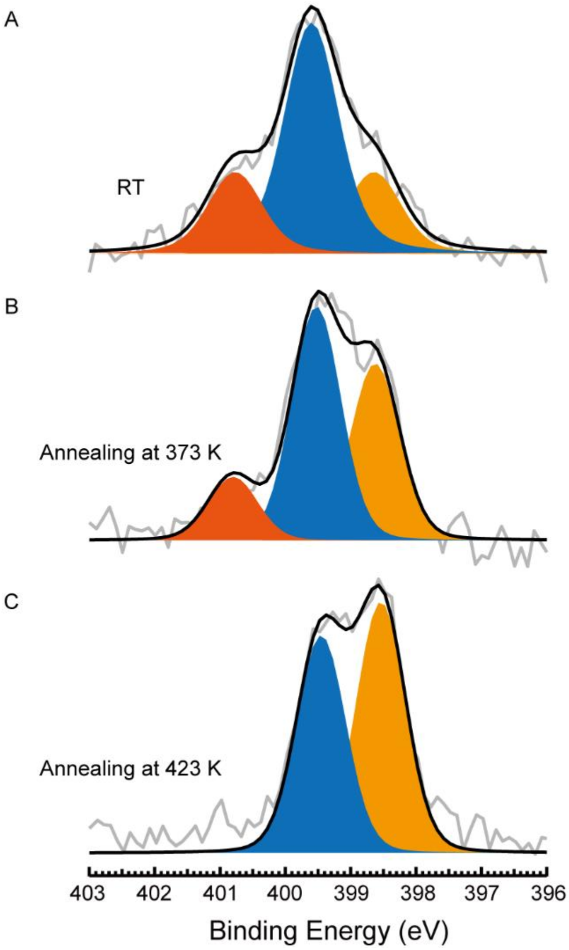

Figure 3.12: XP spectra of N1s of TCPI at RT on Cu(111). (A) Monolayer of TCPI at Cu(111) at RT. (B) Annealingthe sample at 373 K. (C) Subsequent annealing at 423 K..

The coordination bonds of N_{cyano}-Cu-$N_{imidazole}$ bonds and $(N_{cyano})_x$-Cu bonds also coexist on surface, so in this case the signal at 398.5 eV and 399.4 eV represents coordination bonds.

One can observe that the increase of peak ratio of imidazole iminic N to imidazole aminic N which is caused by annealing to 373 K. By annealing to 423 K the aminic N signal is no longer present. This is consistent with a gradual deprotonation and Cu coordination of the aminic N. Hence we can propose that the shift from racemic mixtures of the trimers to enantiomerically pure trimer domains is governed by the deprotonation of the imidazole ring and the replacement of the NH···N bond by N-Cu-N bond.

3.4 Summary and conclusions

We have presented a detailed study of tri(cyano) functionalized lophine on the closed packed coinage metal surfaces by combining STM and XPS. We find that the molecules adsorb intact at room temperature on all three surfaces. The molecules formed close-packed self-assembled structures on Ag(111), and they formed open porous coordination structure with Co atoms at room temperature and higher temperature. The molecules form the same self-assembled pattern on Au(111) with that of on Ag(111), driven by dipolar coupling between two terminal cyano groups of neighboring molecules, hydrogen bonding of cyano groups with imidazole groups from neighboring molecules, and attractive proton acceptor to ring interactions. Porous networks form through the random interaction of N_{cyano}-Co, $N_{imidazole}$-Co-N_{cyano}, NH···N on Au(111). Mixing Fe atoms with monolayer of the molecules also form similar porous structures. On Cu(111), the self-assembly is stabilized by two competitive interactions. The XPS data shows that the Cu adatoms are enrolled into the unit cell at room temperature, and the –NH of the imidazole dehydrogenate gradually with increasing temperature, and finally only the iminic N signal left, which means they form metal coordination structures although the structures observed from STM image almost do not change. We find that Cu, Co and Fe adatoms prefer to coordinate with a terminal cyano group and an iminic N atom of the imidazole moiety rather than the most commonly reported multi-fold cyano coordination.

4. Emerging complexity in two dimensional molecular architectures with bis-hydroxamic acid linear modules

In the past decades, the miniaturization and molecular level control of materials aimed at by nanotechnology witnessed a plethora of mathematically described tessellations realized with atomically precise advanced materials engineering. In this context, the realization of two-dimensional (2D) nanostructures is attracting increasing attention, reflected in detail in recent topical review articles [96, 97]. The 2D supramolecular structures are expected to have promising applications in molecular devices and nanochips among others [98, 99]. In particular the modular assembly of intricate structures and the associated design principles are posing a current challenge. Neoteric breakthroughs include the concept of self-similarity expressed in intermolecular interactions and leading to fractal structures [100] and other tessellations[101], as well as the use of the extended coordination sphere of lanthanide atoms in order to construct well-defined nodes enabling the formation of Archimedian tessellations and 2D quasicrystals [102].

Here we introduce a bioinspired building moiety, hydroxamic acid, for the construction of sophisticated, two-dimensional architectures. Hydroxamic acids are ubiquitous in nature and widely applied in chemistry, biology and medicine [103, 104]. More recently, they have shown promise in dye-sensitized solar cells as anchor groups, where the self-assembly of hydroxamic acids optimizes the adsorption of dyes and in turn influences the power conversion efficiency [105-107]. The functional unit is a suitable binding group for 2D self-assembled structures, with a bonding strength on the native oxides of metal surfaces determined to be in between the carboxylic acid and a thiol [108, 109]. Notably, hydroxamic acids bear great versatility for intermolecular interactions that they exhibit 25 possibilities of 2-fold bonding nodes based on hydrogen bonding according to simulations [110, 111], and have a hitherto unexplored potential for 2D hydrogen bonded structures.

Inspired by previous work on tectons containing multiple head groups, which enabled the formation of intricate 2D tessellations, we designed and synthesized a symmetric linker molecule with opposing hydroxamic acids as head groups and a biphenyl backbone as an ‘inert’ and tunable moiety (biphenyl-4,4′-dihydroxamic acid, BPDH, Figure 4.1A). Here we report on the adsorption of this tecton on Au(111) and Ag(111) surfaces and the pertaining self-assembly by an integrated approach of characterization at the atomic scale encompassing scanning tunneling microscopy (STM), non-contact atomic force microscopy (nc-AFM), complemented by X-ray photoelectron spectroscopy (XPS) and density functional theory (DFT) investigations.

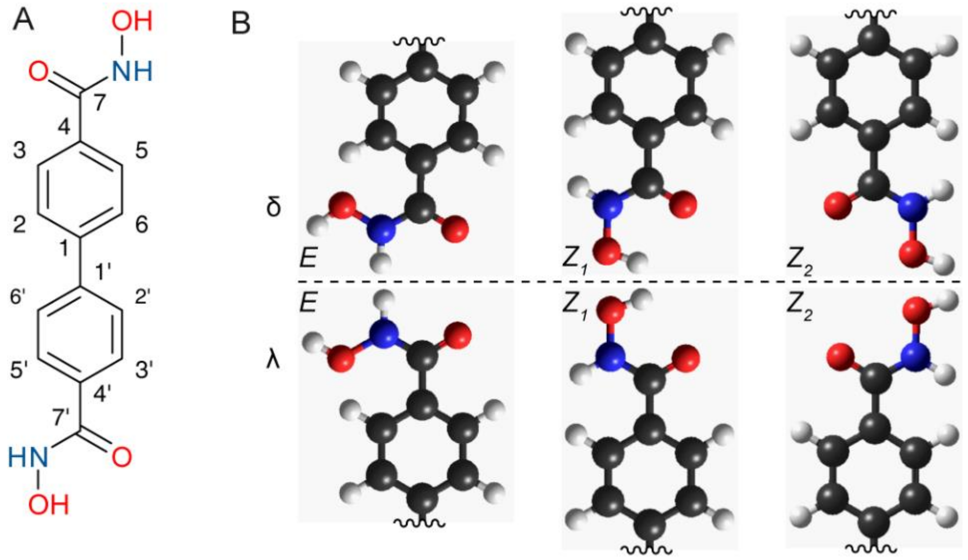

Figure 4.1: Biphenyl-4,4′-dihydroxamic acid (BPDH). (A) Structural formula with C atom numbering indicated. (B) Six possible surface-confined forms of a phenyl hydroxamic acid moiety: E and Z isomers are the result of C–N bond rotation (left and middle panels); the possible rotation around the N–O bond of a Z isomer results in two different rotamers differing in the positions of the alcohol H (middle and right panels); confinement of the hydroxamic acid C atom on a surface results in a chiral center which gives rise to the δ and λ surface enantiomers (top vs. bottom panels).

We have created films of submonolayer coverage BPDH molecules on the Au(111) and Ag(111) surfaces. To characterize these, we will first address the adsorption of the isolated molecules on the surface. In the latter section we will focus in the supramolecular self-assembly.

4.1 Isolated molecule on Ag(111) and Au(111) surfaces

The scanning probe microscopy study reveals very similar topographies for the single isolated molecule of BPDH on both Ag(111) (Figure 4.2A, D) and Au(111) (Figure 4.3) shortly after room temperature (RT, ~293 K) deposition. By STM they are imaged as bright rods, consistent with the biphenyl backbone lying parallel to the Ag substrate along the $\langle 1\bar{2}1 \rangle$ family of directions. In nc-AFM (Figure 4.2D), the biphenyl moiety appears relatively flat as can be seen from the small variation of brightness across the backbone of the molecule [112]. However regrettably the end groups proved elusive [113-115]. BPDH molecules might exhibit a plethora of isomers including Z-E isomers (Figure 4.1B), amide–iminol tautomers and zwitterionic forms [116].

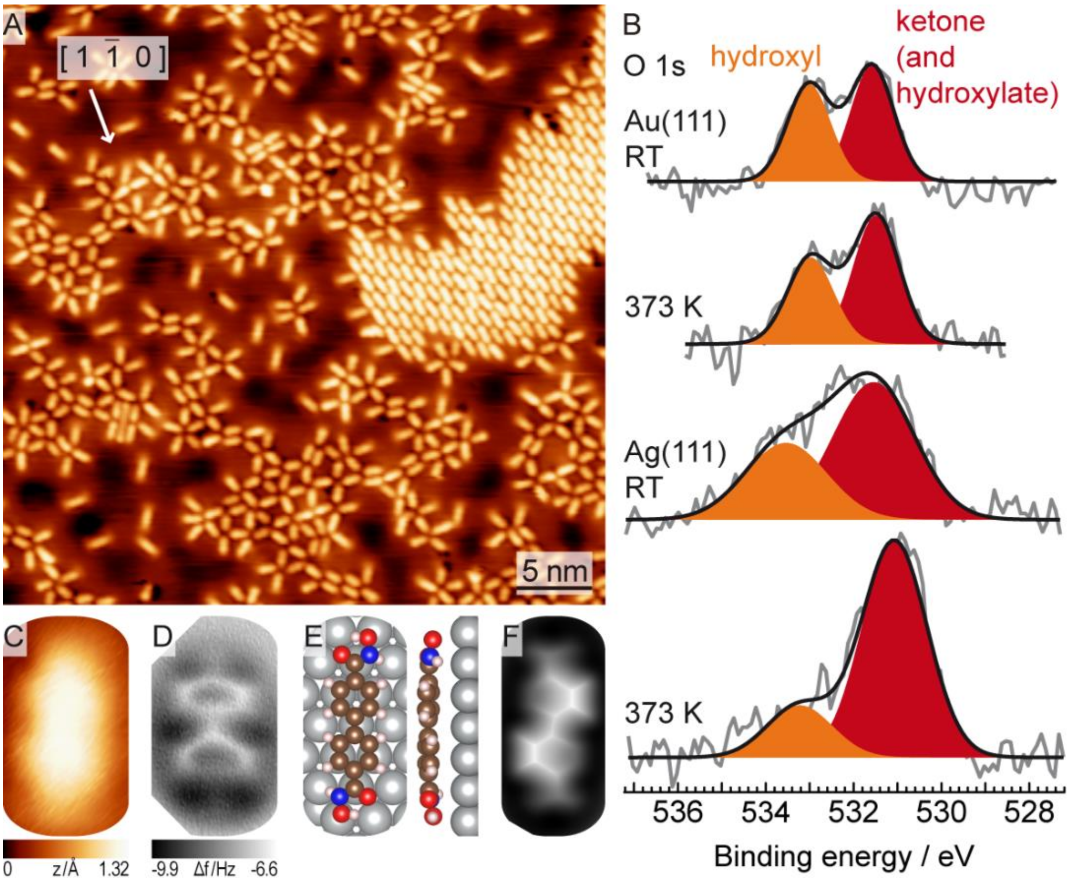

Figure 4.2. (A) STM overview topography of BPDH on Ag(111) following RT deposition (U_s = 1.00 V, I_t = 0.01 nA, recorded at 5 K). The white arrow indicates the Ag $[1\bar{1}0]$ direction. (B) O 1s core level of BPDH molecules: (from top to bottom) adsorbed Au(111) at RT, after annealing at 373 K on Au(111), adsorbed Ag(111) at RT, and after annealing at 373 K on Ag(111). The background subtracted experimental data (grey lines) are fitted (black lines) with two components for hydroxyl (in orange) and ketone plus hydroxylate (in red) contribution. (C-D) Images of isolated BPDH on Ag(111) in the same scale: (C) STM topography (U_s =

0.10 V, I_t = 0.02 nA, 5 K); (D) nc-AFM frequency shift (tip closer by 10 pm with respect to the STM set point above the silver surface); (E) top view and side view of the DFT optimized structure (C, O, N, H, and Ag atoms are represented in brown, red, blue, pink, and silver color, respectively); (F) simulated AFM image (z = 19.45 Å).

In gas phase, according to our DFT simulation, BPDH is more stable in the Z-isomer amide form (Figure 4.4) whereas the existence of the iminol or zwitterionic form is not supported by the respective XPS data (vide infra). Hence, structures of trans and cis isomers in Z-type amide terminal groups, as well as the hydroxamate forms, were considered for DFT simulations of the single BPDH molecule on the Ag(111), in order to identify the preferential configuration (Figure 4.5). From these, only the trans amide form matched the biphenyl alignment along the direction observed by STM. The cis amide form deviates by 9° from the observed one and is less favoured by 0.05 eV, whereas for both *cis* and *trans* BPDH with dissociated O–H bonds, the biphenyl moiety aligns along the Ag $\langle 2\bar{3}1 \rangle$ direction. Upon adsorption, the biphenyl dihedral angle is reduced from 38° to 15° according to DFT. In agreement with experiment, AFM simulations reveal little contrast from the functional group.

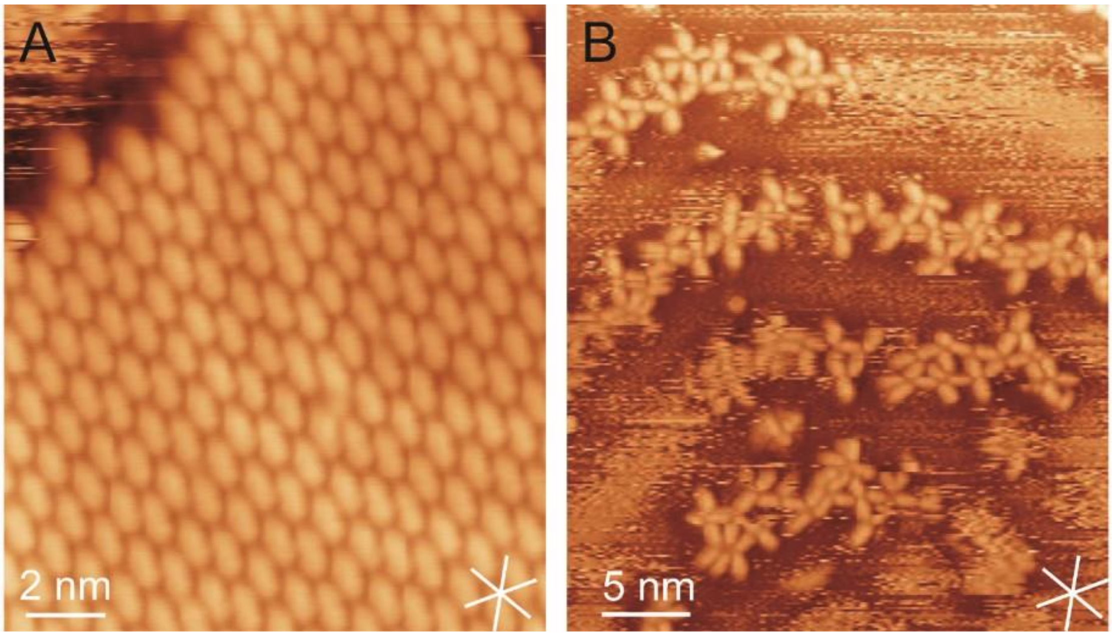

Figure 4.3: STM topography of BPDH molecules on Au(111) substrate. (A) Close packed BPDH phase (130 K, Us = 1.63 V, It = 0.12 nA). (B) BPDH molecules tessellating the fcc domains (130 K, U_s = 1.63 V, I_t = 0.11 nA). The white lines in a star shape indicate the substrate high symmetry axes.

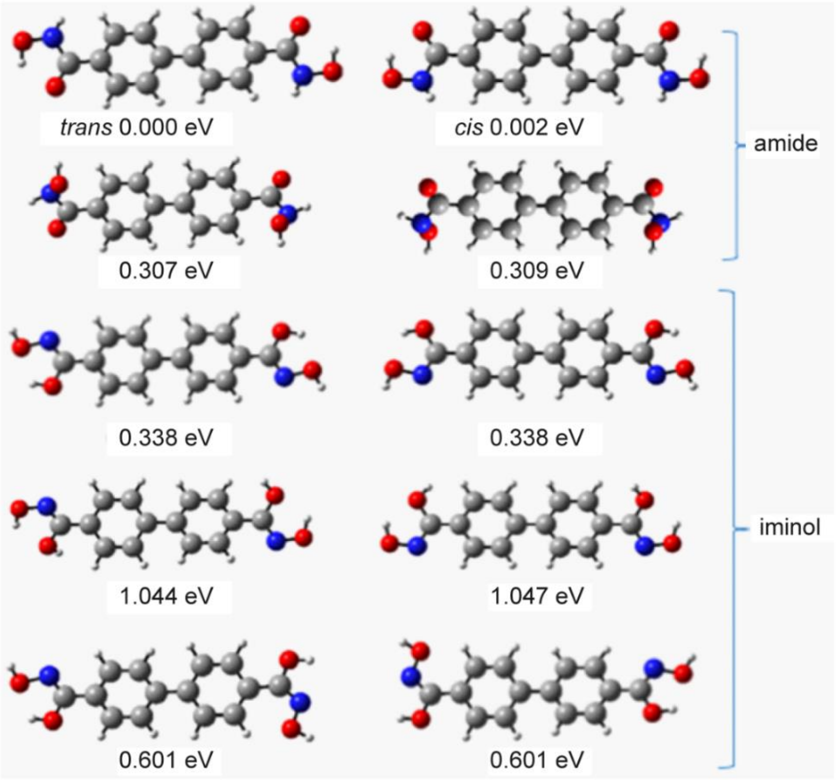
trans 0.000 eV
cis 0.002 eV
amide
0.307 eV
0.309 eV
0.338 eV
0.338 eV
iminol
1.044 eV
1.047 eV
0.601 eV
0.601 eV

Figure 4.4: Ball-and-stick models of DFT simulated structures of BPDH molecule and their energy difference with respect to the most energetically stable isomer. Carbon, oxygen, nitrogen, and hydrogen atoms are shown in grey, red, blue, and white, respectively. We assign the *cis* and *trans* isomers to the structures in which hydroxamic acid's N atoms (of the end group) are located in the same and opposite sides of the biphenyl group, respectively. In its amide form, trans-BPDH is the most energetically stable structure.

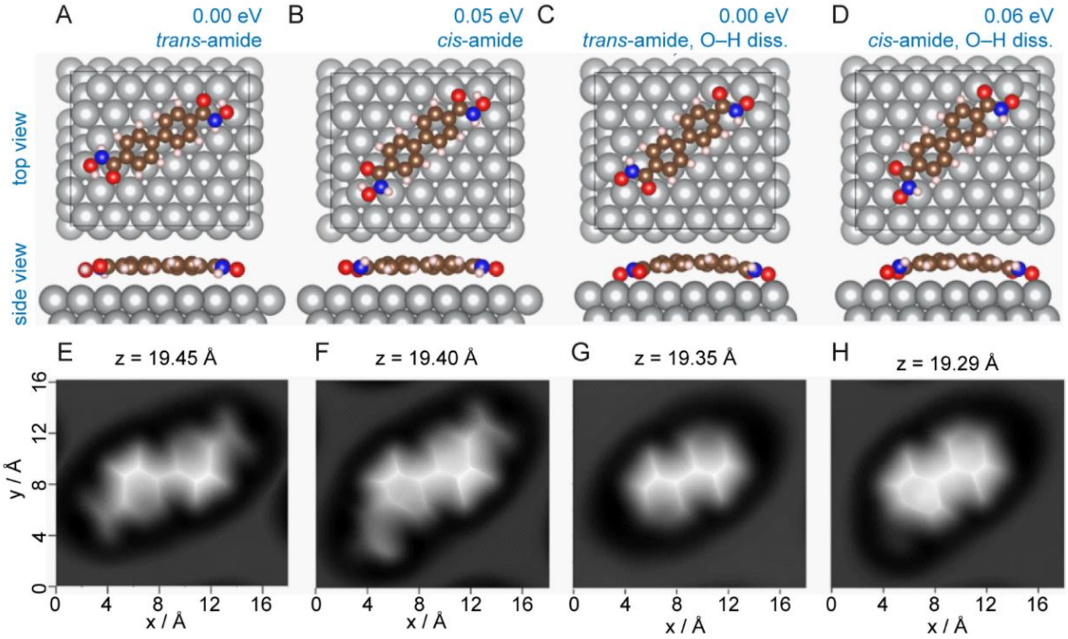
A
0.00 eV
trans-amide
B
0.05 eV
cis-amide
C
0.00 eV
trans-amide, O–H diss.
D
0.06 eV
cis-amide, O–H diss.
top view
side view
E
z = 19.45 Å
F
z = 19.40 Å
G
z = 19.35 Å
H
z = 19.29 Å
y / Å
0
4
8
12
16
x / Å
0
4
8
12
16

Figure 4.5: Top-view, side-view (A-D) and nc-AFM simulated images (E-H) of the adsorption of BPDH on Ag(111) for *trans*-amide (A, E), *cis*-amide (B, F), *trans*-dehydrogenated (C, G) and *cis*-dehydrogenated (D,

H) structures based on DFT simulations. The energy difference between the isomers attributes a more stable structure to the *trans* than its *cis* counterpart, for both the intact and dehydrogenated forms. Silver, carbon, oxygen, nitrogen, and hydrogen atoms are shown in silver, brown, red, blue, and pink, respectively.

4.2 Molecular ensembles on Ag(111) and Au(111)

The O 1s signal of BPDH molecules on the Au(111) and Ag(111) surfaces after RT deposition (Figure 4.2B) provided a signature of the chemical state of the functional group. On Au(111), two peaks at 531.6 eV and 533.0 eV at approximately 1 : 1 ratio can be assigned to the almost equal presence of C=O and –OH groups, respectively. The corresponding N 1s signal appears as a single peak at 399.3 eV (Figure 4.6). For BPDH on Ag(111) at RT, there is a change in the ratio of the components of the O 1s signal with the high energy component attributed to the –OH group being partially depleted already at RT. This effect is accentuated after annealing to ~ 373 K (Figure 4.2B).

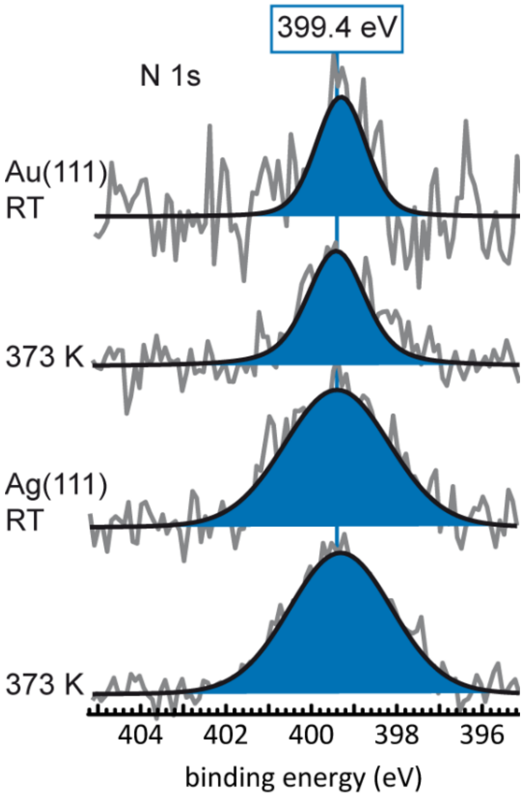

Figure 4.6: N 1s signal of (sub) monolayer coverage of BPDH molecules on Au(111) and Ag(111) surfaces at RT and after annealing at 373 K, as indicated.

This is consistent with a gradual deprotonation of the –OH group commencing already at RT. In addition, compared with the spectra on gold, the N 1s signal on silver display asymmetric broad peak at 399.4 eV (Figure 4.6). We therefore infer that after RT deposition the hydroxamic acid moieties are mostly intact on both surfaces, whereas annealing is promoting the surface induced scission of the O–H bond, an effect which is more pronounced on Ag(111).

Close-packed structures appear already at submonolayer BPDH coverages and dominate the STM images at higher coverages on both Ag(111) (Figures 4.2A, 4.7A) and Au(111) (Figure 4.3A). The molecules form 1D hydrogen bonded chains which aggregate and form 2D islands, reminiscent of the assembly of related biphenyl-4,4´-dicarboxylic acid on Au(111) and Cu(111) surfaces [117-120]. Close inspection reveals that the molecular rods appear asymmetric in the STM image with one end brighter than the other. Interestingly, the chains in figure 4.7A pack in an ABAB fashion with inverse bright ends (marked with yellow and black rectangles) forming a regular structure with frequent defects and a molecular density of ~ 1.0 molecule/nm^2. As the same supramolecular structure was identified on both Ag(111) and Au(111) surfaces, we modelled it with intact molecules on Ag(111) — in accordance with the XPS signals (Figure 4.2B) — in the favorable *trans* conformation. The STM image is partially overlaid with the DFT model in figure 4.7A, showing good agreement. Each hydroxamic acid group participates in two hydrogen bonds (-OH…O=C-) with its neighbor, which stabilize further the molecule in the close-packed structure (adsorption energy of -2.4 eV) compared to single molecule bonding.

The interaction between adjacent molecules is akin to the packing of carboxylic acids on planar metal surfaces [117-120], whereas the amino group does not seem to direct the assembly. We note that more recent reports on the self-assembly of dicarboxylic acid containing molecules indicate that the corresponding overlayer unit cell can be also expressed after annealing-induced (partial) dissociation of the O–H bond [120, 121], an event which we cannot exclude based on our XPS data, especially on the Ag(111) surface.

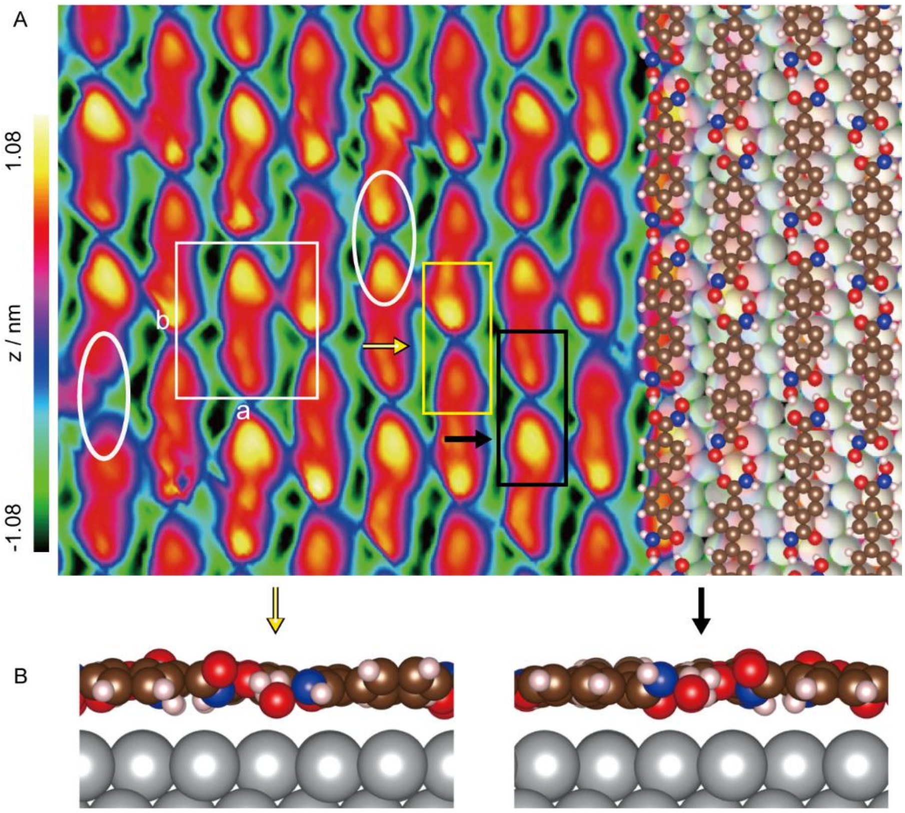

Figure 4.7: Close packed islands of BPDH molecules on Ag(111) substrate. (A) STM image in false color scale (U_s=1.00 V, I_t= 0.01 nA, recorded at 5 K) merged with a top view of simulated structure. (B) Side view of simulated bonding nodes indicated by the corresponding arrows on the STM image. C, O, N, H, and Ag atoms are represented in brown, red, blue, pink, and silver colour, respectively.

Comparing the simulation with the STM data we find that the brighter ends coincide with the physically protruding carbonyl groups (Figure 4.7). nc-AFM data of close packed molecules on both Ag and Au surfaces reveal that different tilt angles of the phenyl substituents exist, evidenced by the variation of intensity in the frequency shift (Figure 4.8). The DFT simulation reproduces the tilt of the phenyl rings with respect to the silver surface with angles of 6° and 22° (Figure 4.7), demonstrating an unexpected effect of the molecule-molecule interaction on the molecular conformation. Some defects in the packing, such as a broken sequence of the bright/dark visualization of the molecular end groups are indicated by ellipses in figure 4.7A. In other areas, small deviations of the direction of the molecular modules can be observed (Figure 4.2A). These are signs of the simultaneous expression of different hydrogen bonding schemes, presumably further facilitated by molecular bond rotations and conformational adaptability. This assembly is characteristic of biological modules which offer a variety of stable hydrogen bonded dimers and can result in many 2D supramolecular assemblies with very similar lattice vectors [122-124]

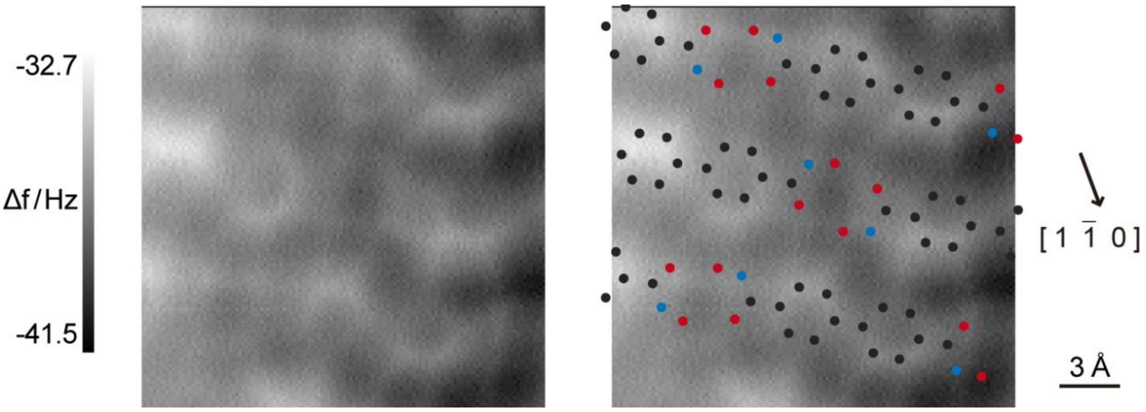

Figure 4.8: nc-AFM image taken on an island of close packed BPDH molecules on Ag(111). Left: Raw data. Right: Raw data overlaid with suggested positions of C (black), O (red) and N (blue) atoms of nodes. The functional group contrast is dominated either by the contribution of the more upstanding carbonyl O atom (e.g. bottom right carbonyl), or evident as a pair of protrusions corresponding to the O atoms (e.g. bottom left node) [125].

Additionally, molecules arrange in different types of molecular clusters with node motifs forming vertices between 2, 3, 4 or 5 molecules (Figure 4.2A), which demonstrates the structural flexibility of the employed functional group in node construction. It should be emphasized that here we use the terms "node" and "vertex" to describe the proximity of 2 or more functional groups, although the molecular axes (line passing through the biphenyl backbone) do not necessarily all intersect at the same point (examples illustrated in figure 4.9). The oligomers assemble in irregular islands also on Au(111), where islands were confined to the *fcc* domains (Figure 4.4).

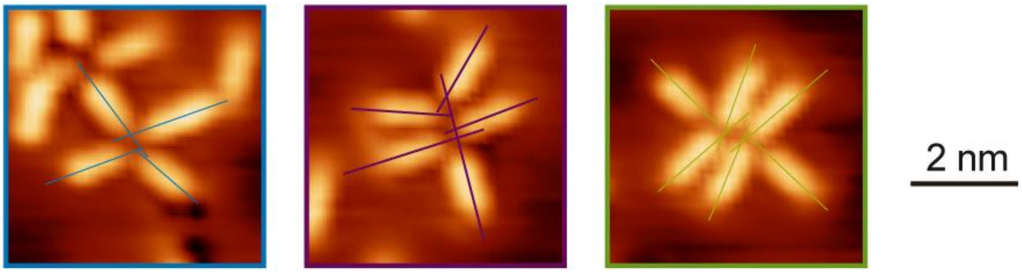

Figure 4.9: Close up to 4-fold (left), 5-fold (middle) and 6-fold (right) nodes from the STM image presented in figure 4.2A.

Notably, an intricate, highly ordered structure can be observed (Figure 4.10) solely on Ag(111). This structure can be found in domains of 50 nm radius (Figure 4.11) and is characterized by an unusually extended hexagonal unit cell of p6 symmetry oriented along the substrate high symmetry axes (Figure 4.10A) and described by the epitaxial matrix

$\begin{pmatrix}25 & 0\\ 0 & 25\end{pmatrix}$. The unit cell (outlined in white in figure 4.10A) encompasses 24 molecules in a relatively low molecular density of 0.53 molecule/nm^2. The large unit cell of this structure impedes DFT simulations, however, we will describe the observed network geometry and propose a tentative molecular model.

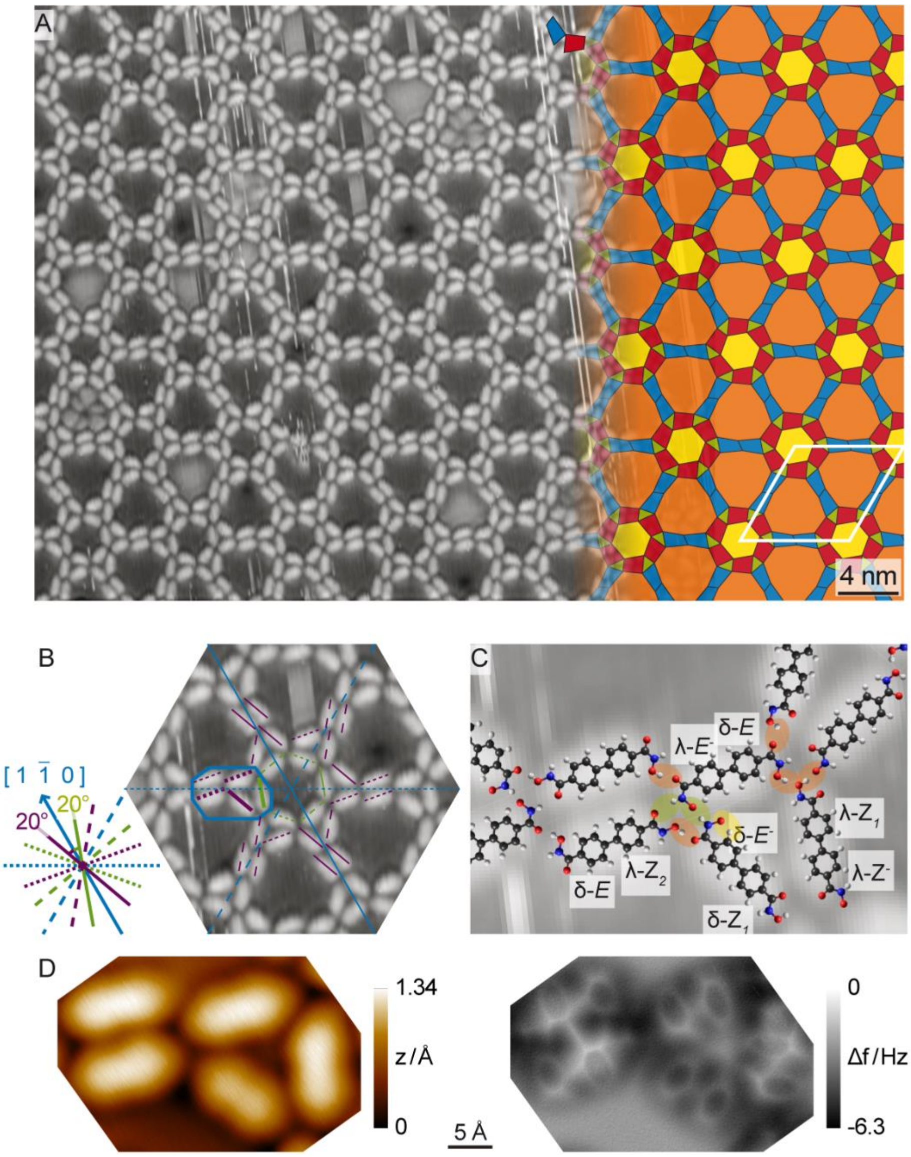

Figure 4.10: Polyporous network of BPDH molecules on Ag(111). (A) STM image (U_s = 0.91 V, I_t = 0.09 nA, recorded at 298 K) partially overlaid with the tessellation on the right. The unit cell is shown in white on the tessellation. (B) Detail of the STM structure overlaid with green and purple lines indicating the molecular axes. Solid lines and different dotted lines of the same color correspond to the same substrate direction and its rotation by 120° and 240°. High symmetry axes of the Ag substrate in blue and molecular axes ordinations in green and purple. (C) Tentative molecular model overlaid on the STM image. C, O, N, and H atoms are shown in black, red, blue and white, respectively. (D) STM topography (left, U_s = 0.10 V, I_t = 0.02 nA,

recorded at 4 K) and corresponding nc-AFM frequency shift (tip closer by 95 pm with respect to a set point above the silver surface) of the fragment of the network making the blue tile (indicated the blue outline in B).

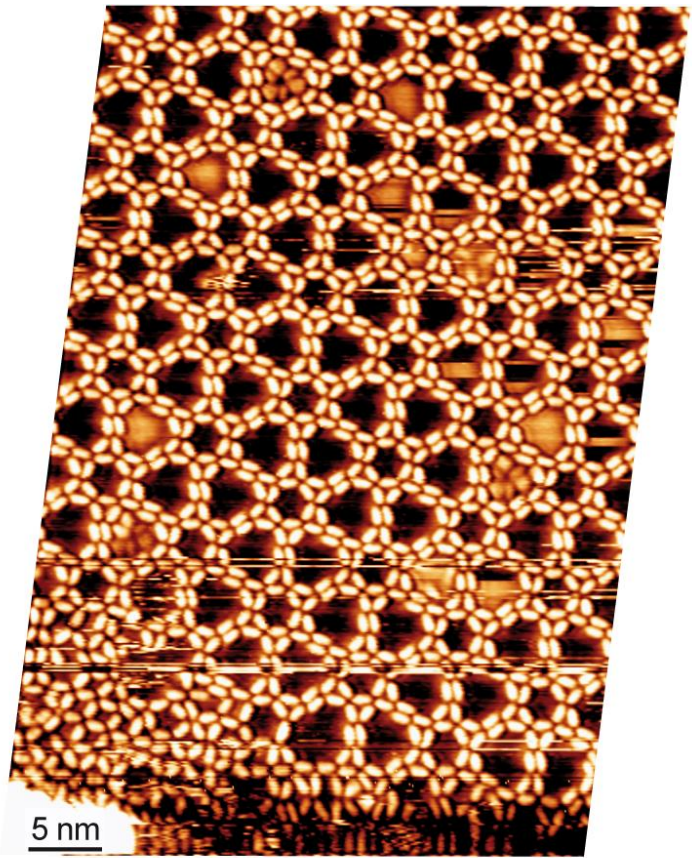

Figure 4.11: STM image (U_s = 0.91 V, I_t = 0.09 nA, recorded at 298 K) of the polyporous structure almost wetting the atomically flat area and bordering to a small patch of the cross-like phase on the bottom left corner.

This complex structure can be deconstructed to consist of solely two supramolecular motifs: two inequivalent vertices of 4 molecules, which can reproduce the complete pattern by (operations of) 60° rotations (permitted by the 6-fold symmetry of the Ag substrate surface layer) and translation dictated by the unit cell. The red and blue tiles in figure 4.10A correspond to these two vertices by linking the (approximate) centers of the related biphenyl moieties. Thus the network can be described by a tiling made by two building blocks corresponding to the nodes of the molecules (red and blue tiles in figure 4.10A) and three building blocks corresponding to the voids (orange, yellow, and green tiles in figure 4.10A). The pores differ significantly in size with the orange, yellow, and green pores (see figure 4.12) having areas of ~ 9.3, 4.2 and 0.5 nm^2, respectively, based on the van der Waals radii of the proposed model. The latter could potentially host a small molecule atomic adsorbates.

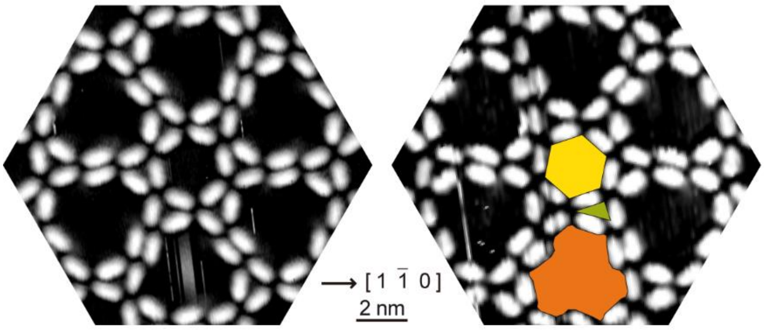

Figure 4.12: Organizational chirality and different pores in polyporous network of BPDH molecules on Ag(111). STM images of the motifs of the polyporous structure in the two enantiomeric domains (left: RT, U_s = 0.91 V, I_t = 0.10 nA, right: RT, U_s = 1.44 V, I_t = 0.10 nA). The Ag $[1\bar{1}0]$ is indicated. The STM image on the right is overlaid with colored blocks (orange, yellow, and green) corresponding to the areas assigned to the different pores (9.3 nm^2, 4.2 nm^2, and 0.5 nm^2, respectively).

A careful examination of the repeated pattern in figure 4.10B reveals that all the BPDH molecules in this structure align with their biphenyl axis at ~ ±20° with respect to the Ag(111) high symmetry direction. The clockwise rotation of -20° with respect to the Ag(111) high symmetry axis of the BPDH molecules enclosing the hexagonal pore (yellow tile in figure 4.10A) and the anti-clockwise rotation of the molecules (by +20° with respect to the Ag(111) high symmetry axis) around the hexagonal pore (orange tile in figure 4.10A) result in a gyrated tiling with organizational chirality [126]. The two enantiomeric domains are displayed side-by-side in figure 4.12. The chirality of the network is transferred to its pores and is expected to be crucial in directing host-guest interactions [127].

In figure 4.10D, a closer look to the blue node by AFM reveals that the biphenyl moieties of the building blocks exhibit different tilt angles, despite maintaining very similar orientations with respect to high symmetry axes. XPS measurements (Figure 4.2B) shortly after RT deposition show a decrease in the relative intensity of the O 1s signal attributed to the –OH groups, indicating a partial deprotonation of about 30% at RT. As the polyporous structure is observed following BPDH deposition on a Ag(111) at RT, we attribute its formation to the partial dehydrogenation of the alcohol moieties. Here, it should be highlighted that the degrees of freedom of the functional group preclude a systematic modeling of this 2D network: to construct this network the two four-fold nodes need to be identified. There are 6 surface amide forms for each surface phenyl hydroxamic acid (Figure 4.1B) and another 4 for phenyl hydroxamate (to account for O–H dissociation). So the sum of 10 possibilities would need to be considered for each of the 8 phenyl hydroxamic acids/hydroxamate moieties which compose the blue and red building blocks, adding up to 10^8 combinations. Nevertheless, one can propose a model, based on H-bridges to stabilize the network. Here we considered the 10 options mentioned above, based on the rational that the small energy difference between *E* and *Z* forms of an isolated molecule in vacuum (Figure 4.4), could be outweighed by the formation of attractive H-bonding in the network. The possible involvement of Ag adatoms in the supramolecular nodes [128, 129] was not considered, based on the intermolecular distances. A tentative model is given in figure 4.10C with the phenyl hydroxamic acids/hydroxamate moieties' configuration labeled as in figure 1B and 3/8 of the groups containing O^- instead of OH groups, in accordance with the XPS signals. Ovals in figure 4.10C are used to highlight the attractive interactions in the proposed model: $OH\cdots O=C$ (orange), $NH\cdots O^-$/ $NH\cdots O=C$ (green) and $CH\cdots O^-$ (yellow) in the blue and red nodes.

Coexisting with the polyporous network and occasionally fluently merging with it, we observed a fully reticulated network comprising 4-fold nodes. These nodes have opening angles close to 90°, resembling crosses, leading us to call it “cross” phase. A zoom in the structure is shown in figure 4.13, whereas an overview can be found in figure 4.14. The assembled networks extend to decorate atomically flat areas. A perusal of the 4-fold nodes reveals their chirality, labelled with purple and green in figure 4.13 to denote *R* and *S*, respectively, analogous to the 3-fold chiral nodes reported in other surface supramolecular synthons [130]. *R* (or *S*) nodes are found to align along the Ag $[11\bar{2}]$ direction. Within the 2D networks formed at RT, narrow areas of conglomerates of *R* or *S* node columns (marked with purple and green dashed lines in figure 4.13A) are found. The arrangement of *R* and *S* nodes results in pores in the network. Based on the ratio of *R* : *S* in the four nodes surrounding each pore, 8 possible kinds of chiral rhomboid pores with various dimensions and shapes occur, as shown in figure 4.13 and figure 4.15. The molecular density of homochiral structures is ca. 0.66 molecule/nm^2. As 1D chiral switches are very frequent, one may suggest that the irregular alteration of the *R* and *S* nodes along the Ag $[1\bar{1}0]$ direction is the signature of 1D randomness (Figure 4.13A) [131]. Indeed the randomness in these domains is also evident as streaks in the fast Fourier transform (FFT) of the STM micrographs (see inset in figure 4.13B and figure 4.14D).

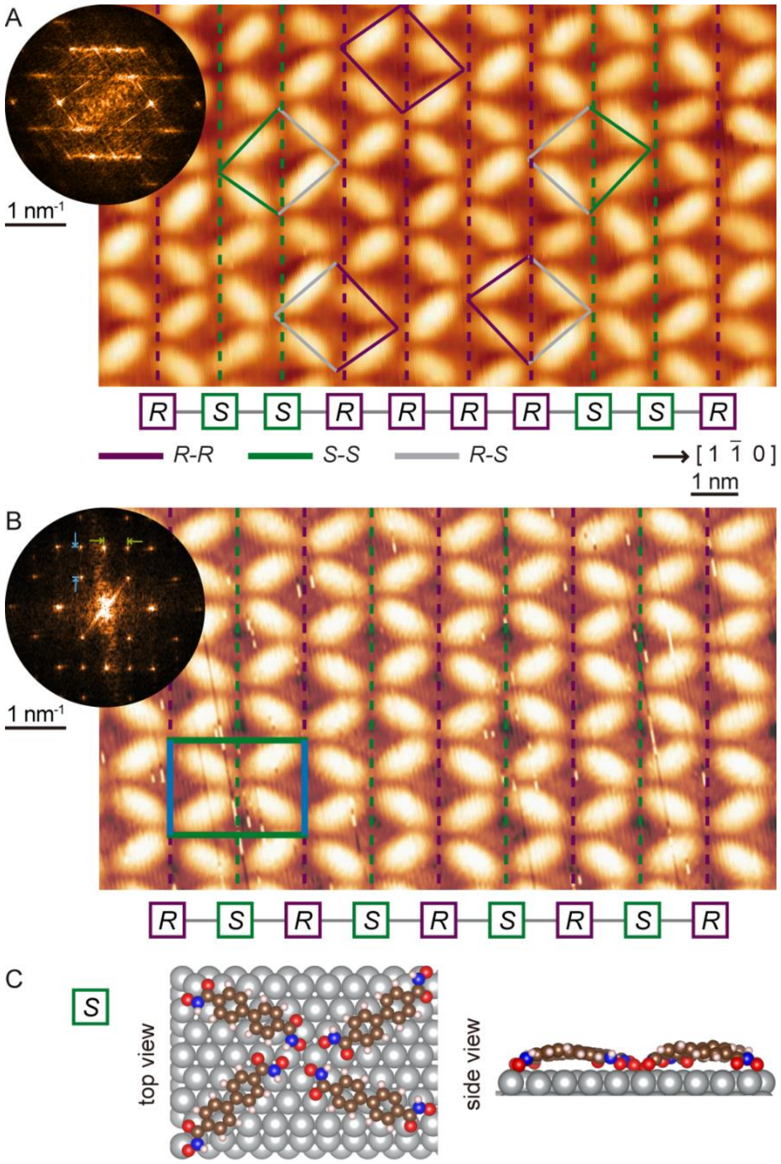

Figure 4.13: Cross network of BPDH molecules on Ag(111). (A) STM image of the self-assembly of BPDH molecules (U_s = 1.06 V, I_t = 0.08 nA, recorded at 140 K) with R (purple) and S (green) chiral structures at RT. (B) STM image after annealing at 373 K (U_s = 1.23 V, I_t = 0.1 nA, recorded at 298 K). The insets in A and B show related FFT of STM data (Figure 4.13). The periodicities of the structure are indicated both in the real and reciprocal space images. (C) Top and side view of simulated S node on Ag(111) surface after annealing. C, O, N, H, and Ag atoms are represented in brown, red, blue, pink, and silver color, respectively

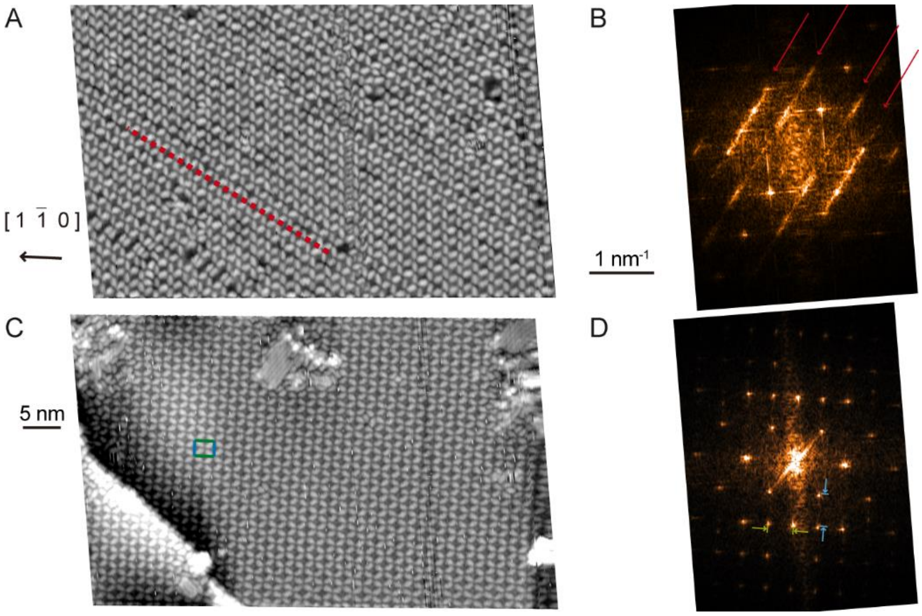
A
B
C
D
[1 $\bar{1}$ 0]
1 nm⁻¹
5 nm

Figure 4.14: The cross network of BPDH molecules on Ag(111). (A, B) After RT deposition (A: STM topography, U_s = 1.24 V, I_t = 0.11 nA, recorded at 140 K, B: corresponding fast Fourrier transform (FFT). (C,D) After annealing at ca. 373 K (C: STM topography, U_s = 1.24 V, I_t = 0.11 nA, recorded at 140 K, D: corresponding FFT). The Ag$[1\bar{1}0]$ is indicated. In A, the red dotted line shows the alignment of the 4-fold nodes along the Ag$[11\bar{2}]$. The same direction is indicated in the FFT image in B by red arrows: the streaking denotes the disorder in the arrangement of the 4-fold nodes in this direction. In C a unit cell can be identified (indicated by a rectangle) and the corresponding FFT in D shows sharp spots (the periodicities of the unit cell are indicated in the same color as in C).

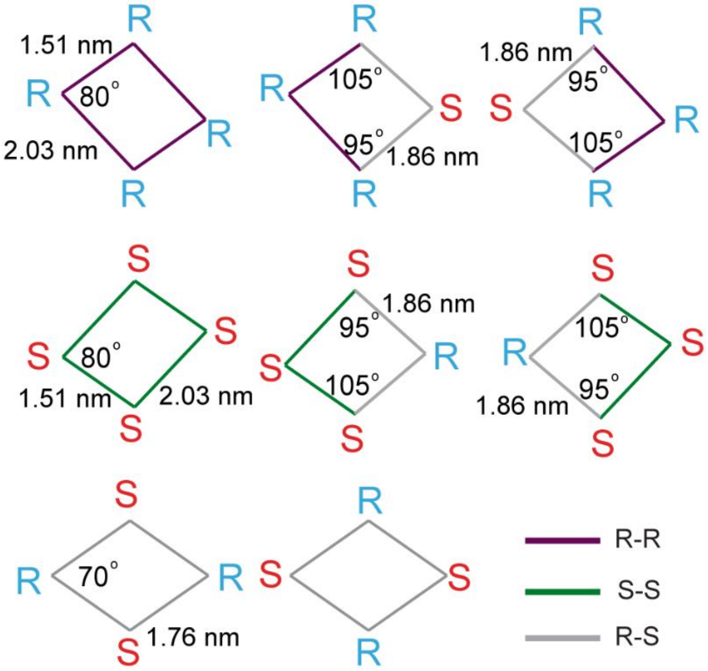
R
1.51 nm
R
80°
R
2.03 nm
R
R
R
105°
S
95°
1.86 nm
R
R
1.86 nm
S
95°
R
105°
R
S
S
80°
S
1.51 nm
2.03 nm
S
S
1.86 nm
95°
S
R
105°
S
S
105°
R
S
95°
1.86 nm
S
S
R
70°
R
1.76 nm
S
R
S
S
R
R-R
S-S
R-S

Figure 4.15: Various pores in cross networks composed of different R and S nodes.

However, advancing the control in the exhibition of this 1D randomness beyond the earlier report [131], we discovered that after annealing to ~ 373 K, the randomly distributed *R* and *S* chiral nodes alternate regularly to form an ordered racemic mixture of *RSRS* lines as shown in figure 4.13B. The *RSRS* cross structure displays a network of high ordering with less defects, as exemplified in larger scale STM data (Figure 4.14), with the corresponding FFT (Figure 4.13) demonstrating sharp spots representing the reciprocal lattice. The rectangular unit cell of the structure (indicated in real space and reciprocal space images in figure 4.13B) includes one *R* node and one *S* node and has a density of ~ 0.68 molecules/nm^2. As this structure did not appear on the Au(111) surface, which offers a closely related epitaxial environment, we deduce that it is driven by the interaction of the molecule with the Ag surface.

To rationalize its appearance and the increased order of the reticular superstructure composed by these chiral nodes, we turn our attention to the XPS results in figure 2. We consider that the molecules in the 2D network with 1D randomness contain also hydroxamate groups, similarly to the polyporous network. The hetero-deprotonation of molecules gives impetus to the 1D random alternation of R and S nodes. On the contrary, the 2D network with the regular arrangement of racemic nodes consists solely of molecules with hydroxamate groups, based on the low signal of OH group, after similar sample preparation in XPS measurements (Figure 2B). To propose a molecular model, we performed a DFT simulation of the regular 2D network with a racemic mixture of nodes. Here a *cis* isomer with two deprotonated –OH groups is used due to the asymmetric bonding of each molecule: the molecule sides are always involved in one *R* node and one *S* node, whereas a *trans* isomer would result in homochiral domains. By using the *cis* isomer, it was also possible to reproduce the observed ‘long’ and ‘short’ intermolecular distances of opposite molecules at the nodes, whereas for the *trans* isomer the equal intermolecular distances were found at the nodes. In the simulated structure (Figure 4.13C), $\mathrm{C{=}O\cdots H{-}C}$ and $\mathrm{N{-}O^{-}\cdots H{-}N}$ intermolecular hydrogen bonds are found between the two left molecules and $\mathrm{C{=}O\cdots H{-}C}$ bonding occurs between the two molecules on the right. The side view in figure 4.13C reveals that the node is stabilized by a strong interaction with the surface, evidenced by the proximity of the O atoms to the surface. The result is a unique cross structure, which appeared only on the silver surface.

4.3 Summary and conclusions

In summary, we found that the bioinspired hydroxamic acid linker molecules provide functional groups with great versatility for hydrogen bonded nodes supported on the noble metals Au and Ag. The related 2D structures exhibited RT stability with densities varying by a factor of almost two between the close packed and more open phases. We demonstrate that the molecular configuration and the “passive” biphenyl backbone is not a rigid building block, but will adapt its adsorption geometry to the different supramolecular assemblies. This finding is important in the design of related supramolecular assemblies. Interestingly, on the Ag(111) surface, the partial dehydrogenation to hydroxamate can give rise to an exceptional polyporous hexagonal framework of unusual complexity, featuring organizational chirality. The dehydrogenation degree also provides control on the ordering of the chiral nodes in a cross network: 1D randomness *vs.* regular racemic 2D networks. Although here the reactivity of the substrate was used to access the deprotonated state, we note that such states can also be realized by employing electrospray ionization deposition system[132] instead of organic molecular beam epitaxy. We therefore conclude that deep insight into the surface properties of hydroxamic acids would give guidance and inspirations for their applications in functional supramolecular assemblies. The use of hydroxamic acids as a directing group in surface supramolecular assemblies can significantly expand the accessible surface tessellations of 2D molecular networks, with high potential as templates. We anticipate that the chirality of the pores in these networks can potentially lead to chiral recognition of larger guest molecules, whereas the polyporous network can additionally provide a template with considerable size selectivity for, *eg.*, nanoparticles.

5. Metal-organic structures of hydroxamic acid on metal surface

As discussed in the previous section, the hydroxamic acid molecules have been used for fabrication of self-assembled structures on Au(111) and Ag(111) surfaces, resulting in versatile highly ordered structures including closed packed, chiral cross network and polyporous hexagonal nanostructures through hydrogen bonding interaction.

Furtherly, surface-confined two dimensional (2D) metal-organic architectures which comprise metal centers and organic ligands with specific functional groups have attracted intense attention in recent decades, while they shows great potential applications in catalysis [133], molecular electronics [134], energy storage [135, 136] and magnetic materials [137]. Compared with other bottom-up methods, it has not only relatively high thermal and chemical stability, but also the structures and morphologies are tunable by metal/ligand ratio, molecular coverage and/or temperature [138-143]. The 2D metal-organic architectures can be prepared in ultra-high vacuum, the metal center could be transition [144], lanthanide metal atoms [145] and alkali metals [146, 147]. The organic ligands can also bond to the native adatoms of the metal substrate, such as copper or silver adatoms [148-150]. Different molecular moieties are employed to fabricate metal-ligand structures, containing cyano group [86], carboxylic group [151, 152], amino group [153] etc. Therefore, the different metal centers and organic ligands confer many different potential applications to this metal-organic architectures.

In section 4 we utilized the dative bonding of the cyano group to transition metal adatoms for 2D metal-organic architectures. Herein, we will introduce hydroxamic acids into surface metal-organic patterns, which is seldom studied on surface, but it has many applications owing to its binding properties with kinds of metal ion, which could be used in mineral collection [154-156], the inhibitors of the enzyme involved DNA expressions [157-159], and dye-sensitized solar cells [105, 160]. However, to the best of our knowledge, the hydroxamic acid molecules have hitherto not been studied in 2D metal-organic nanostructures. Therefore, 4,4′-biphenyldihydroxamic acid (BPDH) is an interesting molecule for metal-ligand structures, we will study the coordination properties of the hydroxamic acid group with Co atoms on Au(111) and Ag(111) surface, combing VT-STM and XPS under ultra-high vacuum.

5.1 Co directed coordination structure on Au(111)

In this experiment, Co atoms were firstly deposited on the Au(111) surface and BPDH molecules were dosed subsequently to dissolve the metal clusters and formed a submonolayer. At the beginning, Co clusters nucleated at the elbows of the chevron structure of the gold substrate similar as depicted in previous work [161, 162]. Subsequently small amount of molecules was added to the surface, resulting in Co atoms clusters surrounded by molecules (green arrows) are shown in figure 5.1B.

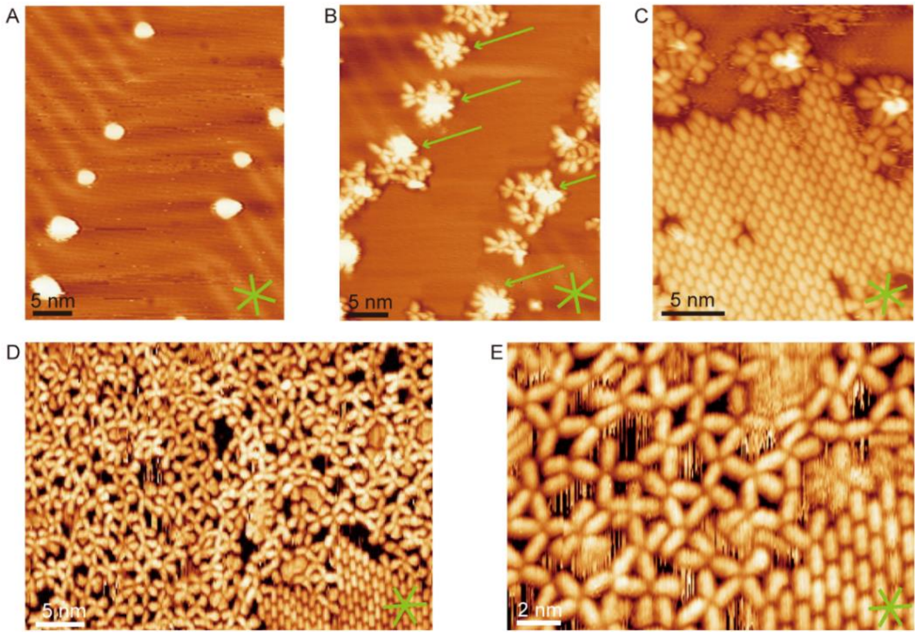

Figure 5.1: STM images of Co atoms and BPDH molecules on the Au(111) surface at room temperature. (A) clusters nucleating at the elbow sites of the chevron pattern of Au(111) (U_s = 1.63 V, I_t = 0.11 nA, recorded at 298 K). (B) Co-BPDH islands on Au(111) (U_s = 1.50 V, I_t = 0.10 nA, recorded at RT). (C) Extended hydrogen bonded BDBH island with Co-BPDH islands on its edge (U_s = 1.13 V, I_t = 0.11 nA, recorded at RT). (D) With increasing amount of Co atoms, BPDH molecules form extended metal-organic structures at room temperature (U_s = 1.25 V, I_t = 0.11 nA, recorded at RT). (E) Zoom-in highlighting four-fold and five fold motifs (U_s = 1.25 V, I_t = 0.11 nA, recorded at RT). The high symmetry directions of the Au(111) substrate are represented by the green lines.

Upon further addition of BPDH molecules, we observed the appearance of the hydrogen bonded close-packed structures described in the last chapter, coexisting with the previously formed small metal-organic islands (Figure 5.1C). However these islands were significantly extended by increasing quantities of Co atom and over time in decrease of the islands of close-packed self-assembly (Figure 5.1D-E). The extended metal organic islands were disordered with various building motifs including tetramer and pentamer nodes, this amorphous structure is similar with previous study [163]. The large clusters of Co atoms disappeared indicating metal dissolution and metal-molecule coordination. Subsequently, an annealing step was carried out to promote long-range ordered 2D nanopatterns.

After annealing at 373 K for 10 min, an ordered metal-organic cross-based network formed in the region of $50 * 50\ \text{nm}^2$, as depicted in figure 5.2A. It is important to note that the metal nodes are oriented along the <1$\bar{2}$1> direction of the gold substrate as indicated in figure 5.2A. Additionally, while the direction of sole molecules prefer to have their biphenyl axis follow the <1$\bar{2}$1> Au(111) directions, it's the chevron structure of gold surface in this structure, which suggests that the metal-molecule and metal-substrate interaction are stronger than the molecule-substrate interaction. This substrate epitaxy in the formed self-assembly is in accordance with the results of molecules on silver substrate in Chapter 4. Figure 5.2A displayed bonding nodes with 3 different directions as labelled in area I, II and III. Intriguingly, in area I and II, the bonding crosses rotated by 90º, however, the metal nodes followed identical direction suggesting the strong template effect acts on the metal centers. Moreover, in area III, the crosses showed a 120º rotation compared with the nodes in area II, nevertheless the direction of nodes also rotated 60º along with other herring bonds. Under this condition, the cross bonding motifs showed 6 possible orientations as illustrated in figure 5.2B. A close-up STM image of this network structure is shown in figure 5.2B overlaid partially with proposed model of the 2D coordination network. The rows of nodes are separated by ca. 2.6 nm (indicated in figure 5.2C), spanning along 9 gold substrate atoms in the high symmetry direction while the node-node distance along the <1$\bar{2}$1> direction is ca. 3.0 nm. The unit cell is indicated by a white rhombus with a side length of a1=2.18 nm and a2=1.80 nm which could be consistent with the epitaxial matrix $\begin{bmatrix} 7 & 5 \\ -1 & 7 \end{bmatrix}$ with a metal-molecule ratio of 1:1. According to the asymmetry of the cross nodes, we assume that every two Co atoms in the center coordinate with six functional group which is similar as previous work concerning carboxylic acid-Fe coordination [164]. For para-position molecules with shorter distance, -OH and C=O group in one molecule interacted with 2 Co atoms showing bidentate coordination, whereas molecules in the other direction, only -OH group coordinated with Co atoms. Therefore, every Co atom interacts with three oxygens. As Co atoms preferentially resided at the hollow sites of the substrate, the nodes direction resulted in the strong epitaxy. We suppose that the 90º direction exchange of bonding nodes are due to the position change of Co adatoms on gold surface as illustrated in figure 5.2 B. In addition, at the edge of the network, bended structures appeared showing a curved arc marked with green oval as shown in figure 5.2A. The bending of hydroxamate-Co bonds may be attributed to: (i) flexibility of the hydroxamate-Co coordination bonds and/or motifs, (ii) different stoichiometry of metal to molecule leading different coordination motif. (iii) incomplete coverage on the surface offering enough space for molecular movement [165]. This network coordination was observed after annealing to temperatures up to 473 K.

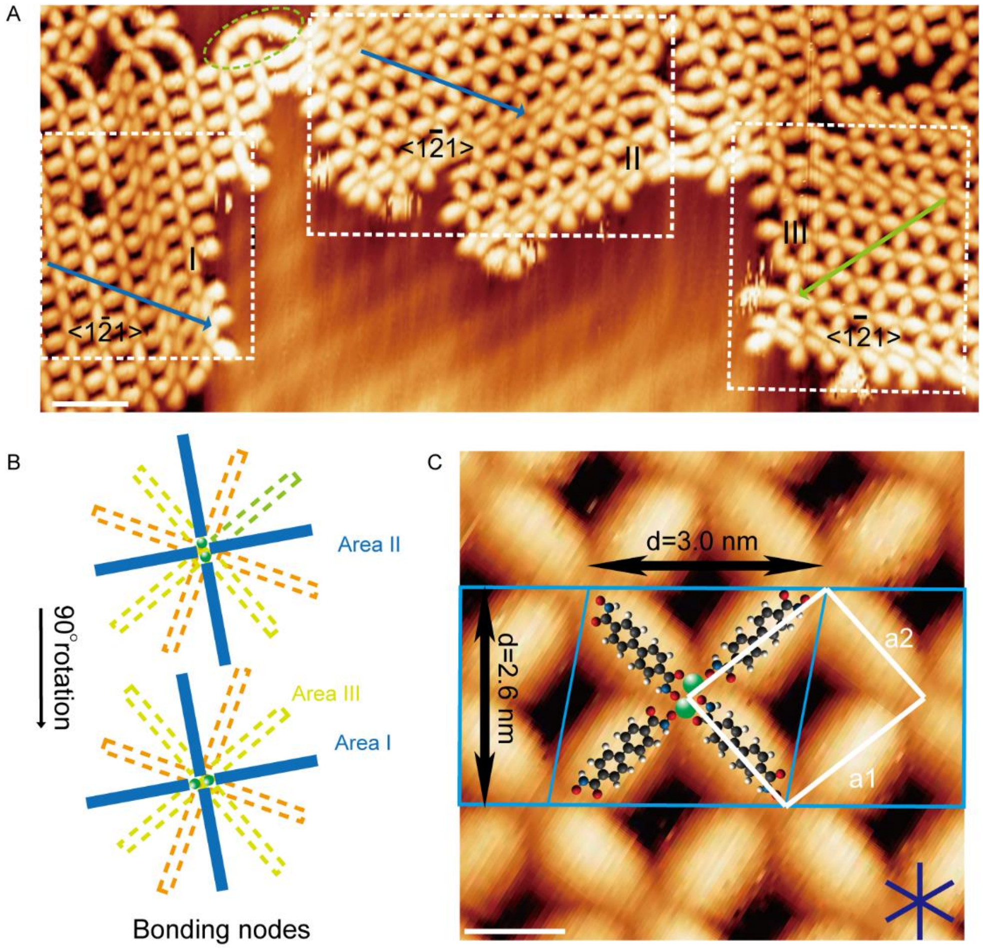

Figure 5.2: STM image of metal-organic network after annealing at 373 K on Au(111) and recorded at room temperature. (A) Large-scale STM image of metal-coordinated network (U_s = 1.25 V, I_t = 0.11 nA, the scale bar is 5 nm, measurement at room temperature). The bending structure is marked with green oval. (B) Schematics of different orientations of coordination motifs in figure A. The angle between each molecular

orientation is 120°, the two different orientation of Co dimer is perpendicular. (C) High resolution STM image of metal-organic network (U_s = 0.94 V, I_t = 0.12 nA, scale bar is 1 nm, measurement at room temperature). The unit cell is marked with a white rectangular. The green balls represent Co atoms. Molecular atomic model overlaid. In the molecule, red balls represent oxygen, blue balls depict nitrogen, black balls stand for carbon element, white balls show hydrogen. The blue lines show high symmetry directions of the substrate.

Experiments of XPS were performed to validate the proposed molecular models. On Au(111),we monitored the signal of the N 1s and O 1s core levels (figure 5.3). At room temperature (figure 5.3A), the molecules without Co are intact as discussed in the last chapter. After dosing Co atoms onto the sample (figure 5.3B), the N 1s peak shifted to a higher bonding energy of 400.1 eV. As we did not observe any indication in the STM data for interaction between Co and nitrogen, the peak shift of N 1s is unexpected compared with previous work and the shift is tentatively attributed to altered charge transfer from the Au(111) and/or screening from the metal substrate in the Co coordinated structure. However, it confirmed that there is no deprotonation of the -NH group. The peak of O 1s at higher bonding energy of 533.0 eV disappeared suggesting that the Co atoms expedited the deprotonation of -OH group. The peak at 531.4 eV became broader indicating the possible different chemical states of oxygen: deprotonated hydroxyl, carbonyl and partial oxygen coordinated with Co atoms. After annealing the sample at 373 K (figure 5.3C), the molecules were more engaged in the 2D network described above, with oxygen coordinated further with Co atoms, reflected in the narrowing of the O 1s spectral peak at 531.4 eV. Therefore, based on the STM and XPS results, we could identify that the molecules are intact after the sublimation to gold surface and the hydroxyl group completely deprotonates with the interaction of Co atoms. After annealing, the metal-molecule coordination resulted in the highly ordered network described above.

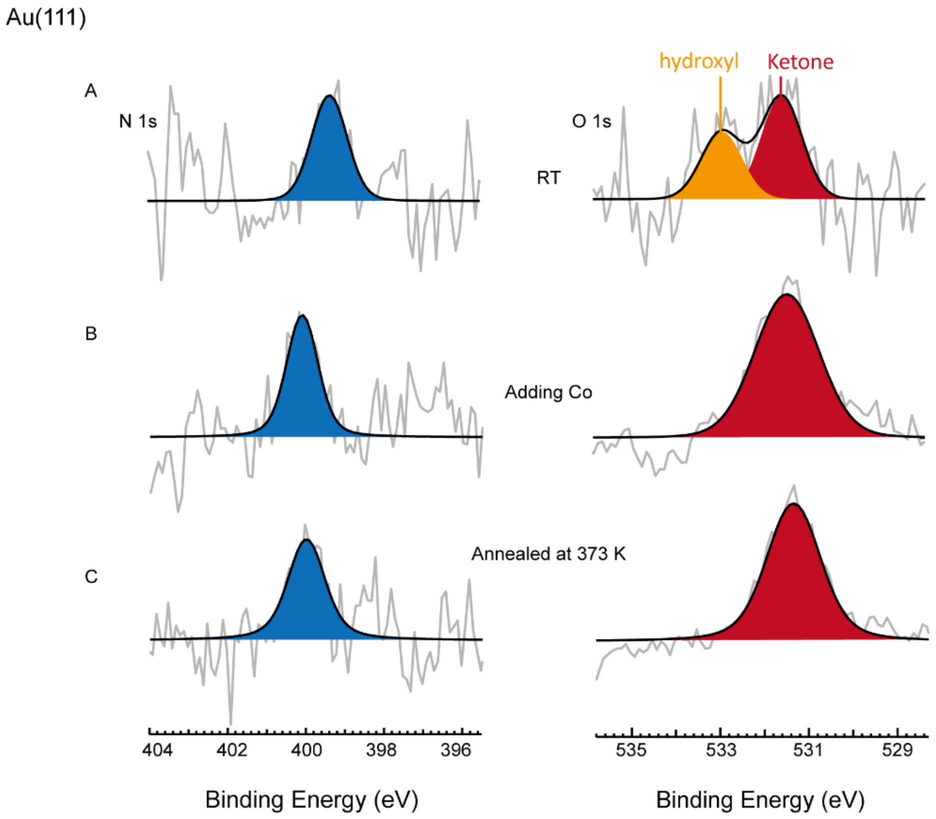

Figure 5.3: XPS measurements of N 1s and O 1s of BPDH adsorbed Au(111) (measured at room temperature). (A) Submonolayer of BPDH on Au(111) at room temperature. (B) BPDH with Co atoms on Au(111) at room temperature. (B) BPDH with Co atoms on Au(111) at room temperature. (C) After annealing the mixture of BPDH and Co atoms at 373 K on Au(111).

5.2 Co directed coordination structure on Ag(111)

To compare with the coordination on the gold surface, the molecules were deposited onto the Ag(111) surface with pre-deposited Co atoms, and were immediately measured with STM at room temperature. Figure 5.4 shows that the molecules with Co atoms formed a random disordered network which is similar as on Au(111) surface (figure 5.1). Different bonding motifs are marked with white circle including 3, 4 and 5 molecules motifs with various geometries. We assume that the disordered structure is constructed by the synergistic effect of metal-molecular coordination and intermolecular hydrogen bonding. However, the molecules showed alternative directions due to the spatial confinement and surrounded motifs. At some area, the polyporous hexagonal structure still existed.

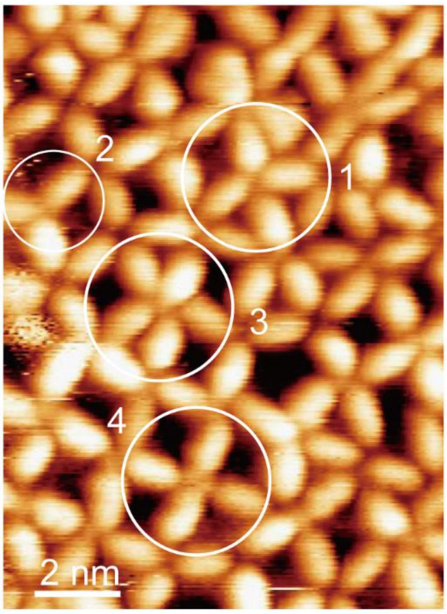

Figure 5.4: High resolution STM image (U_s = 1.28 V, I_t = 0.10 nA, measurement at room temperature) of random coordination network at room temperature on Ag(111). Different coordinated nodes labeled with white circles.

After two hours metal-molecule coordination at room temperature, an ordered porous framework were formed as exhibited in figure 5.5 marked with red triangles. Hexamer bonding nodes appeared with a triangle dark center and extended to a large scale nanostructure. The unit cell shown with a white rhombus includes 2 triangle pores indicated with blue and yellow color pointing up and down, with the side length of 20.5 nm giving the matrix of the unit cell as $\begin{bmatrix} 8 & 4 \\ 4 & 8 \end{bmatrix}$. The alignment direction of the molecules is perpendicular to the direction of substrate while the intermolecular angle is 60º in each triangle. The distribution of the adjacent bonding nodes is also vertical to the high symmetry axis. Due to the different molecular distances in each nodes, we consider the structure contain a mixture of stronger Co coordinated units with hydrogen bond to result in the 2D network by the hierarchical self-assembly. Three molecules with shorter distance are bonding with Co atoms by coordination while other molecules interact with neighboring molecules by hydrogen bonding. We proposed a molecular model for this hierarchical structure as illustrated in figure 5.5C. Three molecules coordinated with Co via the deprotonated hydroxyl group showing a unidentate bonding marked with orange oval in figure 5C. The hydrogen bonding between adjacent molecules is dominated by C=O···H-N interaction marked with green oval in figure 5.5C. For this structure, the metal center is not visible similar to the images reported for Fe centers coordinating three phenolate moieties on the same surface [166].

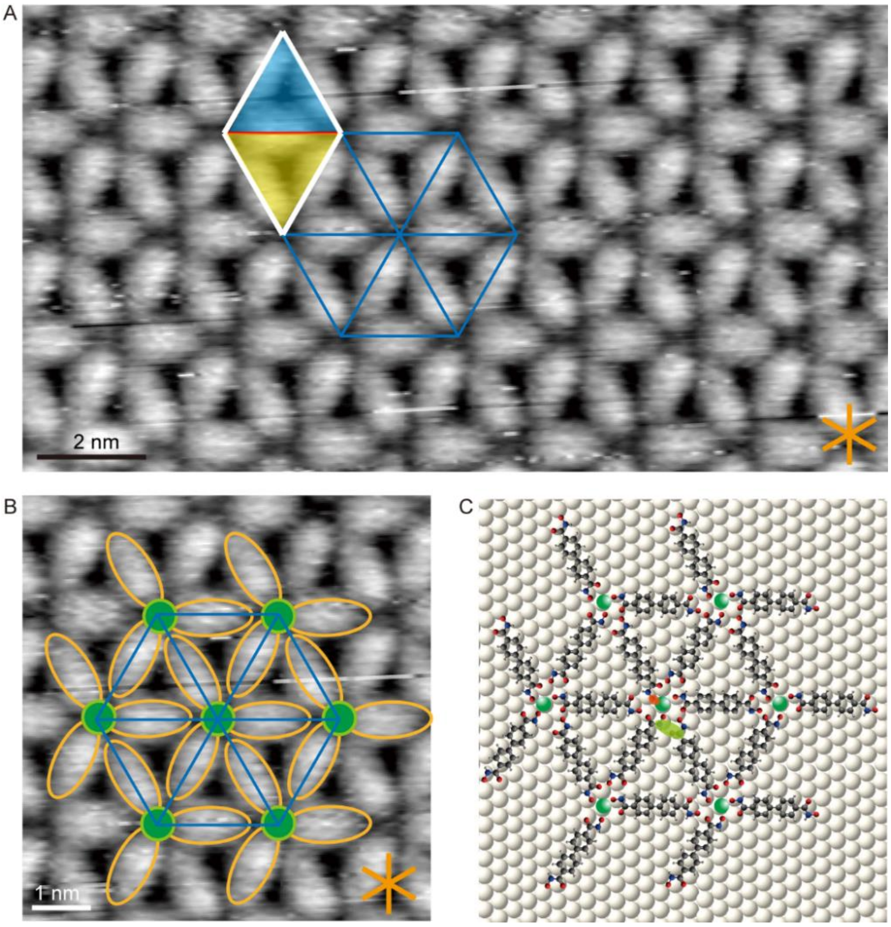

Figure 5.5: Metal-coordination of BPDH with Co on Ag (111) at room temperature. (A) Overview STM image of hierarchic self-assembled structure of BPDH and Co on Ag(111) (U_s = 1.24 V, I_t = 0.10 nA, recorded at room temperature). The unit cell is marked by the while rhombus. The yellow lines show high symmetry directions of the substrate. (B) High-resolution STM image with hierarchical self-assembled model. (C) Corresponding atomistic models. Green ball represents Co atom. Coordination bond and hydrogen bond are marked with orange and green ovals respectively.

From the DFT simulation, we have discussed in detail in section 4, the dehydrogenated *trans*-keto isomers bended and the side group is lower than the phenyl ring backbones on Ag(111) surface. A reasonable explanation for this phenomenon is that the hydroxyl groups coordinated with Co atoms siting on hollow sites of the silver substrate with more warped phenyl rings which are much higher than the Co atoms leading to bright backbones and dark centers.

In a different area, a cross-based network appeared on Ag(111) as shown in figure 5.6A which was quite similar to the structure on gold surface. As mentioned in the last chapter, without dosing Co atoms, both the crosses of the self-assembled structure exhibited 1D random chiral nodes. However, after adding Co atoms, the chirality of the nodes disappeared showing a symmetric cross structure, and the molecular orientation with respect to the Ag(111) also changed. The direction of opposite molecules in the cross structure which are closer together is mainly vertical to the high symmetry axis of the silver substrate. For this cross based structure, we use a similar molecular model as that on gold surface, which consists of 2 Co adatoms in the center, coordinated with molecules through bidentate and unidentate bonding, respectively. Notably, the molecules with unidentate bonding sites have directional variety as shown in figure 5.6B because of the hydroxamate group offers one O site for bonding to the Co atom, while the hydroxamate group offers two O sites in bidentate bonding. Therefore, the relative less liable unidentate interaction leading the tilt metal coordination structure. The direction of bonding nodes can also switch leading to the defects of the formed structure due to the alternation of Co atom pairs as labelled with green and red color. After annealing the sample at 373 K, higher ordering was observed in the cross network as illustrated in figure 5.6C-D. Unidentate-coordinated molecules changed from tilting to perpendicular with the direction of bidentate-coordinated molecules although there are still defects due to the switch of the metal center direction. Interestingly, after annealing, the direction of bonding nodes preferred to be vertical to the high symmetry axis of surface due to the additional energy enhanced the mobility of molecules on the surface while the metal-molecule and metal-substrate interactions dominate the formed structures. The cross based networks have the similar geometry as on the gold surface that the distance between bonding nodes rows is ca. 2.6 nm and node-node distance in the same row is ca. 3.0 nm. The unit cell containing two molecules with the length of b1=2.18 nm and b2=1.80 nm with the angle of 107^{o} between the two sides. The unit cell also could be descripted with the matrix of $\begin{bmatrix} 7 & 5 \\ -1 & 7 \end{bmatrix}$. This is in good accord with templated growth, as the unit cells of Au(111) and Ag(111) differ by less than 0.2%. After annealing, the sophisticated polyporous hexagons and hierarchical hexamer structure disappeared and only the cross network without defects formed. Therefore, this cross based network is the final stable coordination structure, which still existed after annealing at approximately 423 K.

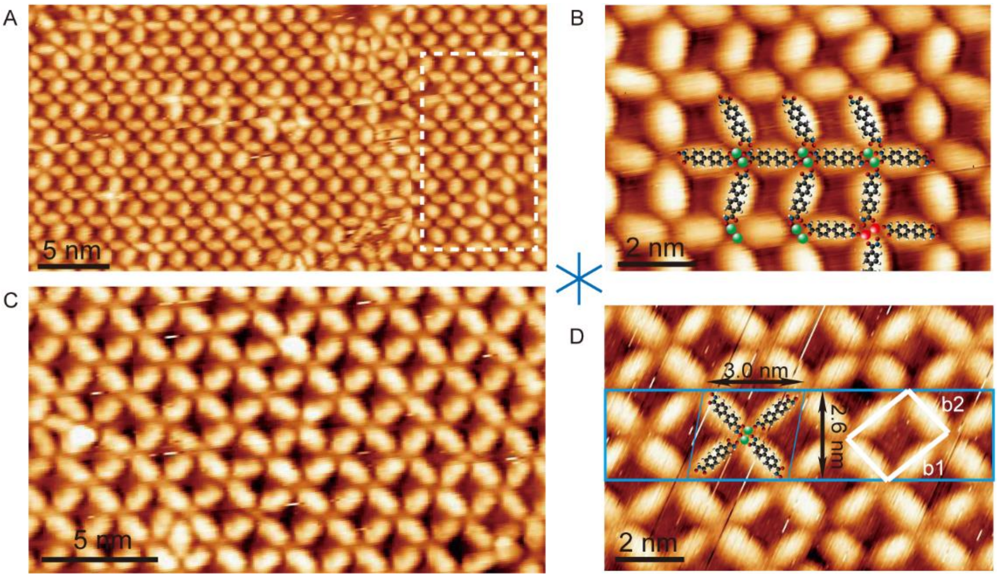

Figure 5.6: Coordination network of BPDH: Co stoichiometry of 1 : 1 on Ag(111). (A) STM image showing ordered network containing bending coordination bonds in the perpendicular direction marked with a white rectangular (U_s = 1.63 V, I_t = 0.11 nA, measurement at RT). (B) High resolution STM image containing bend coordination bonds with molecular model (U_s = 1.63 V, I_t = 0.11 nA). (C) Large-scale STM image of ordered rigid network on Ag (111) obtained after annealing at 373 K (U_s = 1.34 V, I_t = 0.12 nA, measurement at RT). (D) High resolution STM image of rigid coordination network after annealing at 373 K. Unit cell is marked with white rectangle. High symmetry orientation of substrate is depicted by blue line. Green and red balls stand for Co atoms.

The sample was annealed at higher temperature gradually, and the network changed into a random polypore structure after annealing at 523 K (in figure 5.7). The random reticular network is based on three-fold and four-fold nodes and has irregular quadrangular, pentagonal and hexagonal pores, which have been marked in figure 5.7B. After annealing at this temperature, the ordered structures don’t exist anymore, but curved segments meander on the surface. We suppose that the polyporous networks is the result of thermally induced molecular changes and polymerization.

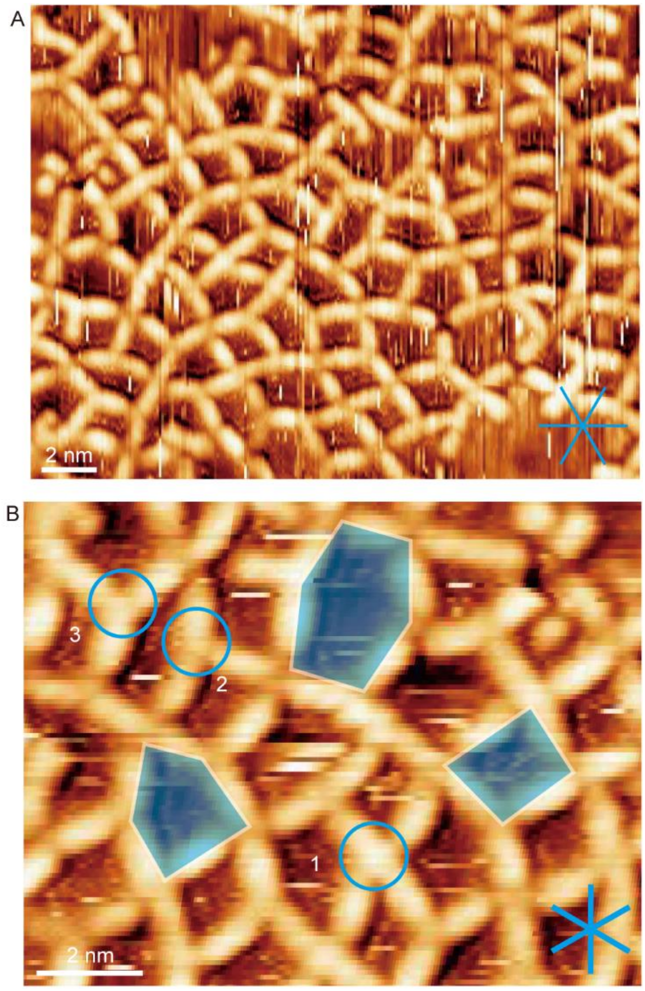

Figure 5.7: Random metal-ligand network after annealing at 520 K. (A) STM image of bent oligomers of BPDH after annealing at 520 K (U_s = 1.20 V, I_t = 0.09 nA, measurement at RT). (B) High resolution of STM image containing different metal-coordinated centers and networks marked with blue circles and green polygons.

XPS experiments at different temperatures were implemented to furtherly analyze the formed nanostructures. From figure 5.8, it is obvious that the spectra of N 1s do not change even after annealing at 573 K indicating that both temperature and Co atoms have no influence on the nitrogen groups of the molecules. The N 1s spectra depicts the possibility of hydrogen bonding between –NH and C=O group in the hierarchical (figure 5.5) and polyporous (figure 5.7) structures on Ag(111). As shown in the last chapter, the hydroxyl group starts to deprotonate already at room temperature evidenced by a reduced contribution in the peak of higher bonding energy of 533.0 eV. After dosing Co atoms, at room temperature (figure 5.8B), the corresponding O 1s spectrum changes from two peaks into one narrow peak at 531.4 eV indicating the complete deprotonation of hydroxyl group which is in accordance with the results on the gold surface and is consistent with the conclusion from STM images. After annealing to 473 K, the O 1s spectrum is constant suggesting the coordination between Co and molecules took place already at room temperature. These spectra suggest that the more order cross based networks after annealing are caused by the diffusion of the molecules on the surface instead of further deprotonation of molecules. After annealing to 573 K, the ratio of molecules to Co atoms decreased from ca. 1.5 (at the beginning) to 1.0 indicating desorption of molecules. The spectrum of O 1s reduced significantly with a very low signal-to-noise ratio which gives us a hint that the polymerization of the molecule at high temperature is related with the loss of oxygens.

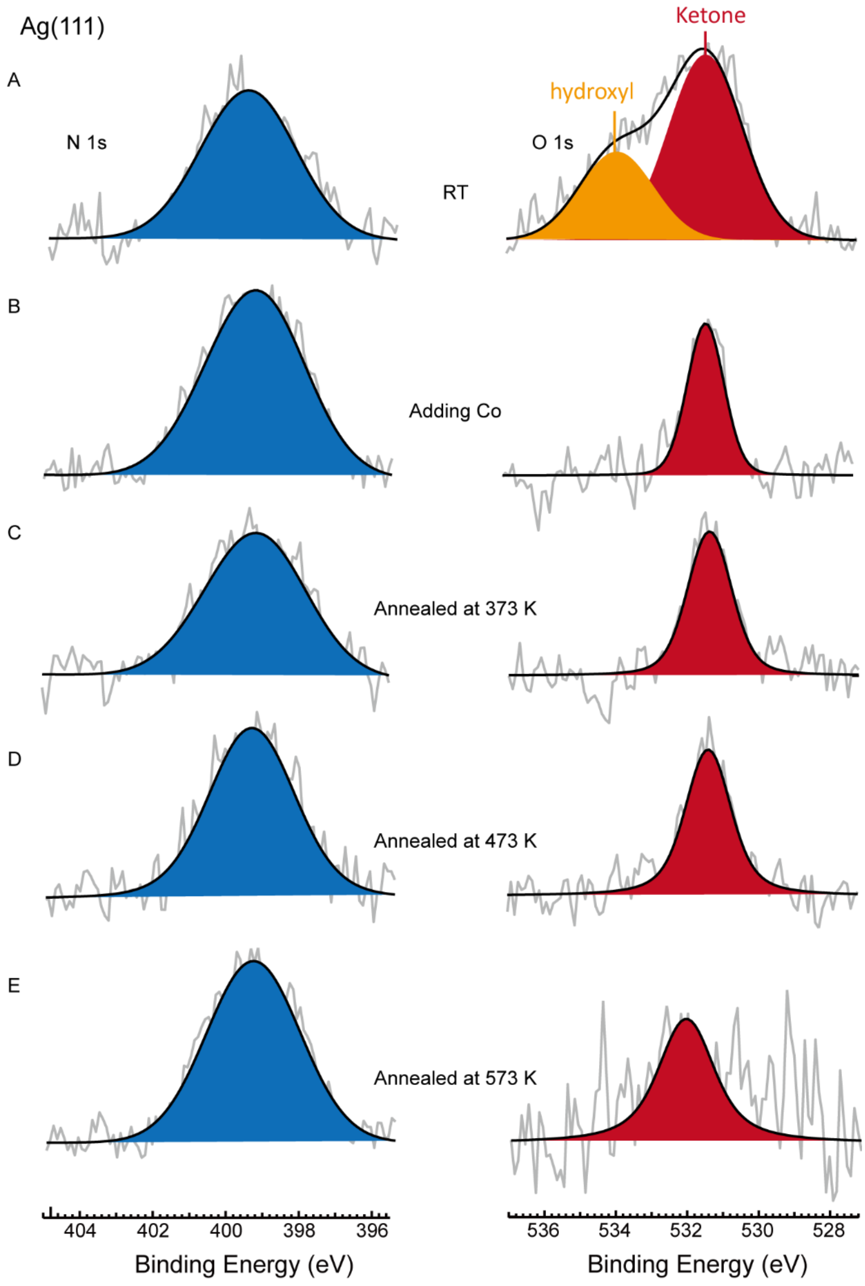

Figure 5.8: XPS measurements of N 1s and O 1s of BPDH and Co adsorbed Ag(111) (measured at room

temperature). (A) Submonolayer of BPDH on Ag(111) at room temperature. (B) Deposition of Co atoms onto submonolayer of BPDH at room temperature, dehydrogenated hydroxamate group and Co atoms coordination occurring. (C) - (E) Coordination of hydroxamate group and Co atom after annealing at 373 K, 473 K, 573 K, respectively.

5.3 Concluding remark

The coordination structures of hydroxamic acid molecules with Co atoms on Au(111) and Ag(111) surface were characterized through STM and XPS techniques. Dehydrogenation of hydroxyl group cause the coordination of BPDH ligand with Co atoms. On Au(111), the molecular structure changed from a close packed pattern to tetramer cross network after metal-molecule coordination with 2 Co atoms as coordination metal center. While on the Ag(111) surface, it forms a similar cross network as that of on the Au(111) surface. Moreover, on Ag(111), we identified a hierarchical self-assembled network at RT constructed by the synergistic effect of metal-molecule coordination and hydrogen bonding. The deprotonation process of the hydroxyl and subsequent coordination with Co atoms are also proved by the X-ray photoelectron spectroscopy of the O 1s signals. The insight in the on-surface coordination of hydroxamic acid with metal atoms at the single molecule level provides a solid foundation for its application as building blocks of 2D networks with potentially interesting magnetic properties.

6. Thermal chemistry and self-assembly of a dihydroxamic acid linear linker on Cu(111)

In the last two sections, we have studied the self-assembly of linear linker molecule functionalized with two hydroxamic acid groups and its coordination with Co atoms on Ag(111) and Au(111). It could be seen that the molecules form novel 2D nano-architectures at room temperature. We found that the series of self-assembly patterns and coordination structures originate from the diverse bonding motifs of the hydroxamate group, which can adapt in different conformations on the metal surface and is prone to form H bonding and coordination with metal atoms, owing that the surface induced -OH group deprotonation.

However, the cleavage of H is not very easy process [167, 168], which usually requires catalyst to achieve the goal, while leading a byproduct, difficult to separate. Therefore, with surface-assisted synthesis [169-172], where the substrate activates the reaction, provides a new way to access the dehydrogenation products. Usually, the on-surface synthesis is characterized combining with scanning tunneling microscopy (STM) with X-ray spectroscopy (XS), it is so-called STM+XS method. The interaction of molecules with Cu adatoms at real-space single molecular level could be investigated by STM, while X-ray photoelectron spectroscopy method detects molecular chemical state on surface. Until now, activation of N-H [173-175], O-H [176, 177] and C-H [178-180] has been successfully obtained, the free H atoms usually desorbed from the surface as the H_2 gas, so that with the surface-activated reactions, we only get obtain the main desired product, avoiding byproducts. Consequently, surface-assisted reactions could be applied in the industry of pharmaceutical [181] and nanodevices [182].

Herein, applying the 4,4′-biphenyldihydroxamic acid (BPDH) (Scheme 6.1) on the Cu(111) surface to study its dehydrogenation is very meaningful. In this part, we study the coordination of the hydroxamic acid group with Cu atoms at room temperature and higher temperature. The length of the molecule is 14.3 Å (scheme 6.1), defined as the two end hydrogen atoms, according to the DFT calculations. To the best of our knowledge, its dehydrogenation process when adsorbing with the C-N bond parallel to the surface has not been yet explored while it has showed great promising application in enzyme inhibitor [183], solar cell [105] etc.

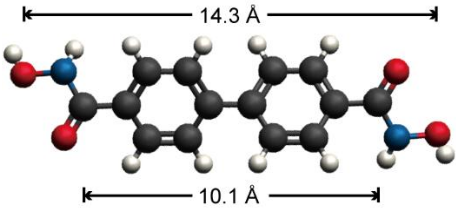

Scheme 6.1: DFT simulated chemical structure of 4,4´-biphenyldihydroxamic acid with minimum energy. (H, white; C, black; N, blue; O, red).

6.1 Densely packed metal-coordination structure on Cu(111) at room temperature

The large portion of the molecules assemble in an extended close packed structure following molecular deposition on Cu(111) at room temperature (see figure 6.1A). This is a periodic structure with the unit cell of $a_1 = 9$ Å, $b_1 = 32$ Å, and the angle between them is 75º. The short side a_1 has an angle of 48º with the orientation of the substrate. The unit cell could be described by the epitaxial matrix $\begin{bmatrix} 4 & 3 \\ -1 & 12 \end{bmatrix}$, and contains two molecules. The supramolecular structure is stable at room temperature as evidenced by the stable imaging. The molecules in adjacent rows show different orientations in figure 6.1B and reproducibly have different apparent heights. The similar close packed structure were also discovered on Ag(111) (in chapter 4), however, taking insight into single molecule, we found the molecular rods show different appearance at the end. Compared with the asymmetric contrast of the end on Ag(111), molecule shows symmetric appearance of the contrast in the STM image, the length is comparable to the theoretical DFT value of 1.43 nm in gas-phase. Therefore, the molecules lie parallel to the Cu(111) surface. The different apparent heights in the adjacent line due to difference in the adsorption site [184, 185]. We assume the BPDH molecules as *trans*-conformation on the Cu(111), and the brighter protrusions are ascribed to the tilt of the biphenyl moieties with respect to the surface. It is found that the molecules of adjacent rows have a head-to-head interaction, which is the interaction between the hydroxamic acid groups. To account for this head-to-head interaction, we propose that two opposing oxygen atoms are linked with a copper adatom illustrated in figure 6.1B. We conclude that the carbonyl group has strongly hybridized with the states of the copper surface promoting the oxygen to coordinate with a Cu adatom, forming the C-O-Cu bond. The hydroxyl group also deprotonated (as it will be shown by the XPS results below), enabling the respective oxygen atom to also coordinate with a Cu adatom, forming N-O-Cu bond, which is depicted in figure 6.1B. Therefore, every Cu adatom is ligated by two oxygen atoms of opposite molecules. Both of the processes of double bond weakening of the carboxyl group and the deprotonation of hydroxyl group occur once the molecules were deposited on Cu(111) single crystal at room temperature, owing that the strong interaction of the Cu with the hydroxamate group at room temperature. Every molecule forms four coordination bonds, and the relative strong metal ligand interaction makes large areas of the closed packed supramolecular structure stable at room temperature.

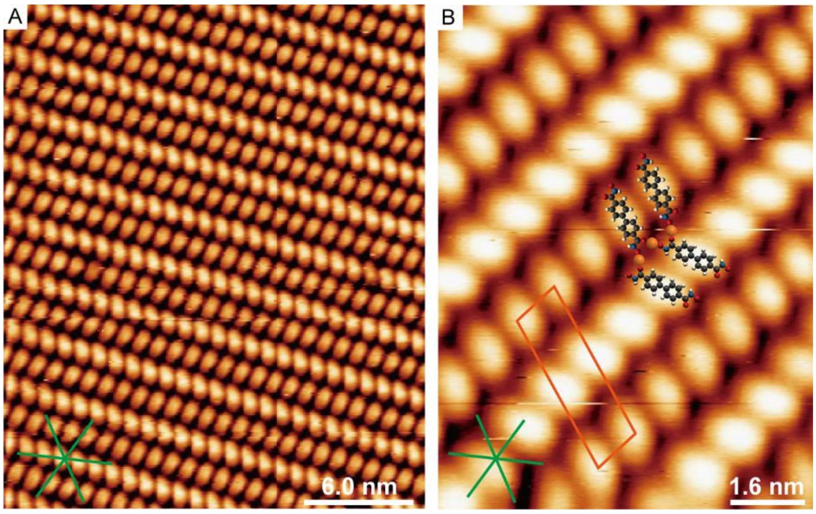

Figure 6.1: Close-pack structure of BPDH at room temperature on Cu(111). (A) Overview STM image of close packed arrangement (I_t = 0.06 nA, U_s = 1.7 V, recorded at room temperature) (B) High resolution STM image (I_t = 0.11 nA, U_s = 1.5 V, recorded at room temperature). The unit cell and the high symmetry axes of the substrate are indicated by the orange parallelogram and the green lines, respectively, proposed molecular ball-and-stick model and Cu adatoms (yellow ball) overlay on the image.

6.2 2D metal-organic coordination network involving stoichiometric Cu adatoms/BPDH ratio on Cu(111) at room temperature

The molecules could form other organic-coordinated structures on Cu(111) at room temperature. The molecules could form other organic-coordinated structures on Cu(111) at room temperature. It could be seen that BPDH molecules displayed long range of well-ordered two dimensional nanostructures at low molecular coverage, which are shown in figure 6.2. The structures keep stable at room temperature, reflected by STM image. One structure is a 4-fold organic-coordinated structure, reminiscent of the respective adatom coordinated dicarboxylic acid linear linkers [141, 186], the dicarboxylic acid linear linkers dehydrogenated once confined on Cu(111) at room temperature, different supramolecular networks could form at different metal atoms/molecules ratio. Herein, the unit cell of 4-fold network has been marked by the yellow rectangle in figure 6.2. Every unit cell contains four molecules, the sides of the unit cell are $a = 28$ Å, $b = 22$ Å, and the angle between them is 90º. The long side a has an angle of 9º with the <110> orientation of substrate. The matrix of the unit cell is $\begin{bmatrix} 12 & 2 \\ 3.5 & 10 \end{bmatrix}$. Another structure is marked by the green hexagon in figure 6.2. It could be observed the ordered hexagrams are connected with each other to form large scale polyporous nanostructures. And the direction of the four-fold linkers between the molecules are the same as the high symmetric axis of single crystal. Herein, length of BPDH is 1.43 nm, the distance of O-O between two molecules is 0.3 nm, which is longer than hydrogen bonds. Recent studies reveal that this ordered structure formed via substrate-mediated interactions [187]. Herein, we proposed that the dehydrogenated O atoms interact with substrate, the formation of polyporous structure is ascribed to O-substrate interactions.

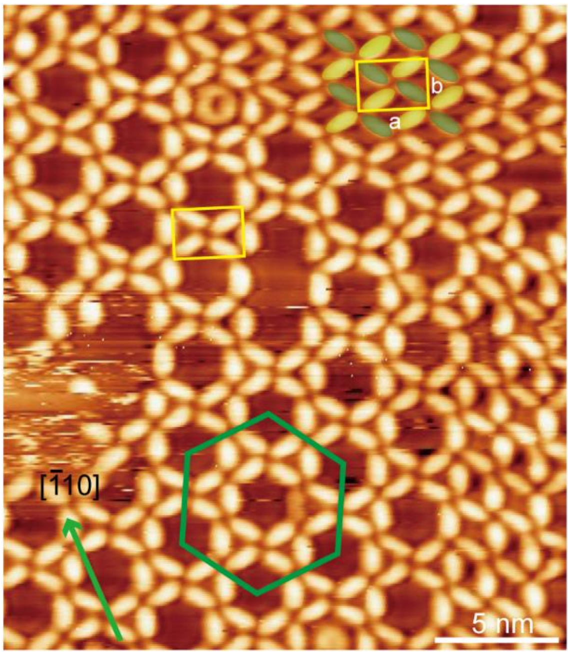

Figure 6.2: Porous metal-organic coordination structures on Cu(111) at room temperature. Large-scale STM image (I_t = 0.11 nA, U_s = 1.56 V, recorded at room temperature). The colorful ovals label the molecules in

four-fold metal-organic structures, the unit cell is marked with yellow rectangular. The connected hexagonal molecular structure is marked by a green hexagon. The green arrow marks the Cu [$\bar{1}10$] direction.

The atomic model of the four-fold metal coordinated node is depicted in figure 6.3, where it can be seen Cu adatom dimers form the center and bond with four molecules, this four-fold also exists in the polyporous structure (labeled with yellow rectangle), but the metal-ligand bonds of the four molecules are inequivalent. In the direction defined by the Cu adatom dimer, two oxygen atoms of the same hydroxamate group coordinate with a Cu adatom (forming the expected chelate of Cu with C-O-Cu and N-O-Cu bonds). Perpendicular to the Cu dimers, only one oxygen atom coordinates in η^2 with the Cu adatom dimer.

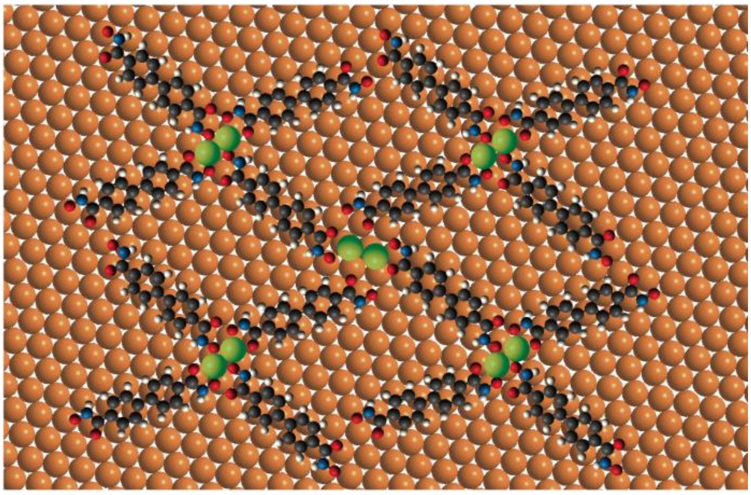

Figure 6.3: Tentative atomic model of molecules of four-fold structure on Cu(111) surface, the green (orange) balls represent Cu adatoms (surface atoms).

The other coordinated structure motif is depicted in finer detail with the high resolution STM image in figure 6.4A. Is a hexagonal structure with (the unit cell has been marked in yellow in figure 6.4A) with a side length of 35.5 Å. The unit cell is described by the matrix $\begin{bmatrix} 16 & 8 \\ -8 & 8 \end{bmatrix}$ and contains six molecules. The structure of highly ordered hydroxamate-Cu adatom dimers networks is stable at room temperature due to the coordination bondings. The pentagram structure marked with the green ovals. The proposed coordination motifs are analogous to the ones presented for the four-fold network in figure 6.3, every Cu adatom dimer is coordinated by three oxygen atoms (Figure 6.4B). The molecules have undergone dehydrogenation of the hydroxyl groups and the carboxyl groups are strongly hybridized with the on Cu(111) at room temperature. The coordination with Cu adatoms to form polyporous nanoarchitectures could be proved by the following XPS signals. Apart from these three kinds of metal-coordination structures, we also found that the pentagram structure served as cages to confine two BPDH molecules in the hexagonal nanopores as shown in figure 6.5. The hexagonal networks are prepared in a large-scale and are thermally robust, as discussed above. In the supramolecular cave, two BPDH molecules can be observed clearly, while their orientations changes continuously. From the previous work [188, 189], it was found that, the confined monomer attached to the 2D metal-organic network of polyphenyl dicyano modules, owing to the attraction between phenyl rings and CN end groups. Supramolecular dimers in the cage, were thermally activated to rotate. In our case, the hexagonal caves are very stable at room temperature through the metal-organic interaction, while the dimers are found to rotate at room temperature. The conformation of the dimers is stabilized during the rotation event through the interaction of hydrogen bond interaction, the length of C-O···H-N is 1.5 Å. It was found that the process of rotation occurred continuously between sequential images from 6.5A-H with the intervals of 37 seconds. Through observation of lots of STM images, it could be found that the dimers adsorbed onto the hexagonal sides, which means that the dimers form the hydrogen bond with the phenyl ring of the rim, which is marked by green oval in figure 6.5A’. The oxygen atoms of dimer interact with the phenyl ring of the rim in every position from 6.5A-H. Therefore, the interaction between the dimer is relative stronger, the rotation should overcome the interaction between the dimer and Cu substrate and the interaction between dimer and the molecules belongs to hexagram.

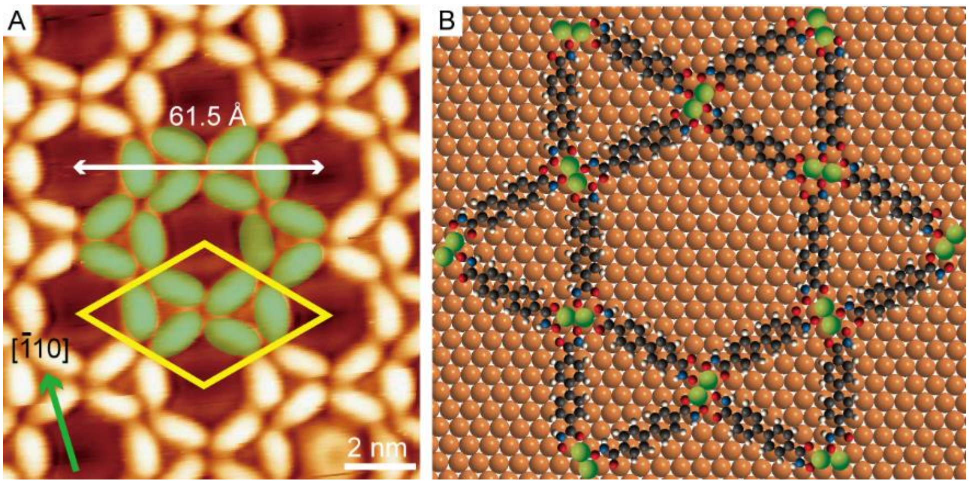

Figure 6.4: (A) High resolution STM image of the hexagonal molecular structure (I_t = 0.10 nA, U_s = 1.56 V). The molecules forming a pentagram are labeled by green ovals, the unit cell is marked by the yellow rhombus. The green line shows a direction of substrate close packed atoms. (B) Proposed atomistic scale model of the

pentagram observed in figure A; the green balls represent Cu adatoms.

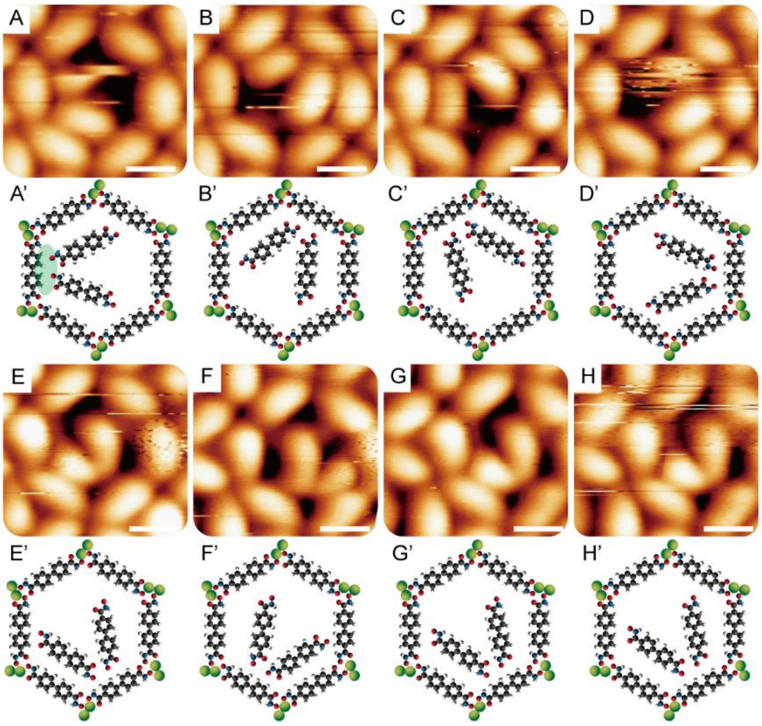

Figure 6.5: Rotational motion of molecular dimers in supramolecular cage. Continuously recorded STM images from A to H (all the values of U_s are kept at 1.3 V, and $I_{t,A}$ = 0.10 nA, $I_{t,B}$ = 0.06 nA, $I_{t,C}$ = 0.11 nA, $I_{t,D}$ = 0.10 nA $I_{t,E}$ = 0.10 nA, $I_{t,F}$ = 0.10 nA, $I_{t,G}$ = 0.10 nA, $I_{t,H}$ = 0.10 nA), all the STM images are recorded at room temperature. From A' to H' is the atomic model corresponding to the STM image respectively. Green balls represent Cu adatoms. Scale bars are 1 nm.

6.3 Stable metal-coordination structure on Cu(111)

After mild annealing of BPDH to 333 K on Cu(111), we found new structures by imaging the surface at RT (figure 6.6). It could be observed that the molecules with Cu adatom dimer formed flower-shape metal-organic structures, which is marked with orange ovals in image 6.6A. In the center of every six molecules, there are two protrusions are considered as two Cu adatoms. The dinuclear center has three orientations with respect to the substrate. According to atomic model in image 6.6B, and the atomic module of Cu(111) substrate is shown in image 6.6A, it's obvious that the direction of dinuclear center has the same orientation of the Cu(111) substrate and the dinuclear center could fit the size of the protrusion very well in image 6.6A. We conclude that the protrusions are the Cu(111) adatoms. We can see that six hydroxamate groups coordinate with metal center, the oxygen is the same chemical state with previous procedure (vide infra XPS), but after annealing, we propose that most of the nitrogen has deprotonated, which could be proved by the data of XPS. The unit cell has been marked with a red rhombus in the model presented in figure 6.6B. It contains twenty seven molecules, had side of 63.80 Å length and the angle between the sides is 120°. It can be described by the matrix $\begin{bmatrix} 29 & 14 \\ -14 & 14 \end{bmatrix}$. Comparing with the high symmetric direction of substrate, we found that the molecules arrange in the perpendicular direction with the substrate. Investigation of the flower-shape structure, it could be seen that the N has dehydrogenated. However, we consider that they are not enrolled in the coordination with Cu adatoms, it's most possible that the N has strong interaction with the substrate. XP spectrum could provide further explanation for the STM images.

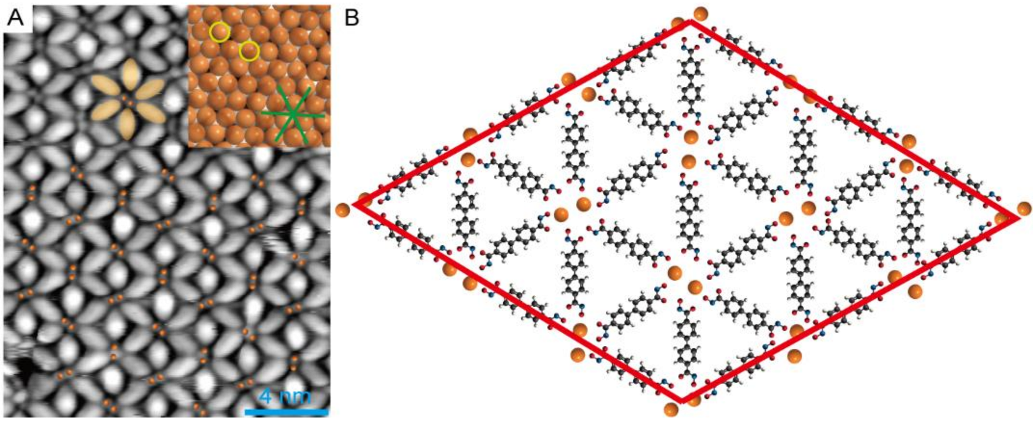

Figure 6.6: Metal-organic nanoarchitecture after annealing at 333 K. (A) High resolution STM images of six-fold metal-organic packed (I_t = 0.11 nA, U_s = 1.50 V). The orange ball represent Cu adatom. The green line shows high symmetric direction of substrate. The yellow ring labeled Cu adatom tetramer. (B) Molecular model of image A. The unit cell are marked with red rhombus.

For XPS experiments, we prepared a sub-monolayer of BPDH molecules (3 min of sublimation) on bare Cu(111) surface, then it was measured at room temperature. The signal of C 1s, N 1s and O 1s exhibited by the black lines in figure 6.7A, 6.7B and 6.7C respectively. For the C 1s, it shows two peaks, the main peak located at the binding energy of 284.5 eV is attributed by carbon on the phenyl ring, the small peak centered at 287.7 eV is ascribed to carbon of the functional group, the area ratio of the two peaks is 6 : 1, matching with the theoretical value very well. If the molecules are deposited continuously, only the intensity of the two peaks increase gradually. From the C 1s signal, we could show that carbon of the hydroxamic acid don't split off from the phenyl ring during the process of sublimation and deposition. In the N 1s signal (Figure 6.7B), there are also two peaks after 3 min sublimation of molecules (black line): one peak is centered at 398.2 eV is ascribe to intact nitrogen, and another peak centered at 397.0 eV belongs to deprotonated nitrogen. We propose that this shift is caused by a charge transferring from the Cu(111) substrate or by the coordination of the neighboring O-Cu. With increasing molecular coverage from sub-monolayer to multilayer, a small shoulder at 400.0 eV appeared, which belongs to the intact N without effect by the substrate. The result is consistent with the previous work [190]. The energies of the other two peaks do not shift, only change in intensity. The signal of O 1s is shown in figure 6.7C, there are also two peaks once the molecules form a submonolayer, the peak at 529.4 eV belongs to C-O-Cu coordination, and another peak centered at 531.1 eV refers to N-O-Cu coordination. Compared with the previous work [106], the two oxygen peaks shift to lower binding energy due to the strong interaction between O and copper adatoms cause high efficiency of the screening of the core-hole, resulting in a shift to lower binding energy.

From the XP spectrum, it could be concluded that the dehydrogenation of hydroxyl groups takes place at room temperature on Cu(111), while the ketone group also form coordination bond of C-O-Cu, which proves our assumption based on the STM images. From the 1s signal of C, N, O, we know that hydroxamate group has coordinated with Cu adatom at room temperature on Cu(111)

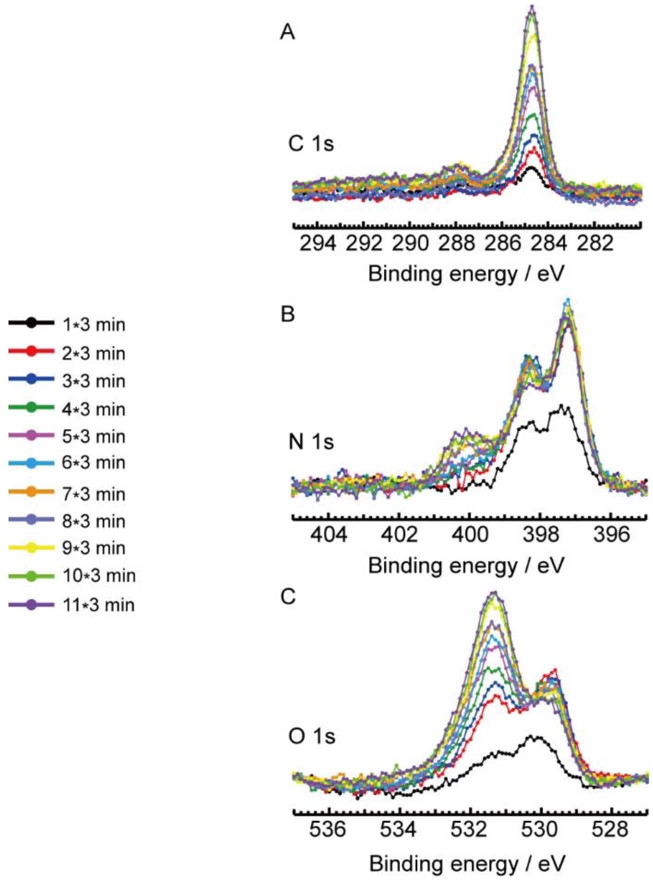

Figure 6.7: X-ray photoelectron (XP) spectra of BPDH uptake on Cu(111) surface. Image (A) to (C) is C 1s, N 1S and O 1s signal. Sequential dosing of equal amounts of BPDH is (three minutes deposition at a molecular temperature of 463 K) was interrupted for recording the XP spectra of different colors.

Then the molecules sublimated 5 minutes to form a monolayer on Cu(111). The signals of N 1s and O 1s at room temperature are showed in figure 6.8A. The peak of N 1s centered at 398.2 eV belongs to -NH, while another peak centered at 397.1 eV stands for dehydrogenated N. The dehydrogenated process of amide group on coinage surface has been studied in previous work [173, 191]. In our work, the two N 1s peaks shift to lower binding energy with 1 eV compared with literature value. This inconsistence presumably originates from strong interaction between imide group with Cu substrate and the contribution of hydroxyl group, leading to higher charge dense on nitrogen atom. With increasing annealing temperature, N will dehydrogenate gradually, finally after annealing at 473 K, most of the nitrogen has dehydrogenated with a small portion of nitrogen left. For the signal of O 1s at room temperature, the peak at 531.1 eV is assigned to C-O-Cu coordination, whereas the peak at 529.9 eV is thought to represent N-O-Cu coordination, and the two peaks do not change with increasing of annealing temperature, which means C-O-Cu and N-O-Cu keep stable at higher temperature.

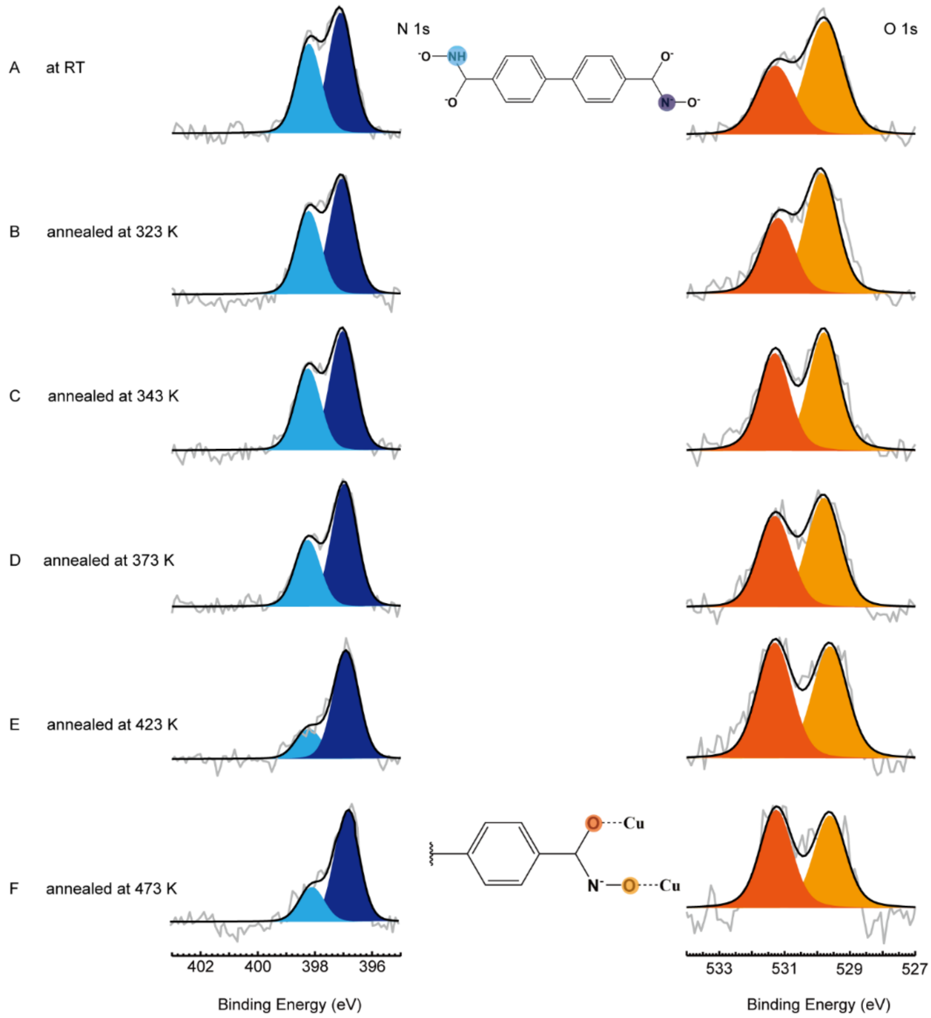

Figure 6.8: XPS measurements of N 1s and O 1s regions on Cu(111) surface with gradual increasing of temperature. (A) Monolayer of BPBH on Cu (111) at room temperature. From (B) to (E), annealing the substrate gradually at the indicated temperatures, the N dehydrogenated gradually with increasing of the temperature. The signals of O 1s do not change significantly.

6.4 Conclusion

In summary, we have studied the in-plane metal-organic structures of BPDH on Cu(111) combined with STM and XPS, which gives insight into the hydroxamic acid molecular coordination on the surface. We found that the hydroxyl group of the functional group dehydrogenated once the molecules are deposited onto Cu(111) at room temperature, and the oxygen could coordinate with Cu adatoms to form three ordered metal-organic structures. In the close packed structure, single adatom metal center coordinate with two oxygen atoms. Another ordered network structure is driven by Cu adatom dimer, every dimer coordinate with six oxygen atoms with inequivalent interaction. The same coordination nodes also exist in the hexagonal structure. An interesting supramolecular motor is found. The dimers of BPDH, which are formed by supramolecular interactions, are confined in a hexagonal molecular cage, could rotate continuously and are very stable at room temperature. And the metal-ligand structures would change into a relative close packed metal-coordinated architecture with temperature increasing, it was found that every six molecules coordinate with dinuclear metal center to form a flower-shape structure. And the nitrogen has dehydrogenated gradually after annealing the sample, while the nitrogen atoms are not involved directly in the planar interactions driving the formation of the flower-shape metal-organic structures. Therefore, at room temperature, BPDH presents diverse coordination behavior and the molecular motor could form and be investigated successfully. We found that thermally induced different nanoarchitecture started to form at 333 K. We provided a detailed description of the behaviors of the hydroxamic acid molecules on Cu(111) surface, which offer great help for its further application.

7. Conclusions and Outlook

A systematic study of the self-assembly of cyano functionalized lophine molecules, and hydroxamic acid molecules as well as their coordination with different metal adatoms on closed packed coinage metal surfaces was presented in this thesis. STM provides the atomic resolution topology of the architecture, XPS measurements gives further insights into the chemical state of the molecules.

Tri-cyanophenyl imidazole (TCPI) was investigated on Ag(111), Au(111) and Cu(111) to reveal its novel coordination motifs with different metal atoms. We studied the influence of the annealing temperature, different metal atoms and the underlying metal single crystal surface on the nanoarchitectures. On Ag(111), the molecules formed ordered close-packed self-assemblies structure, driven by hydrogen bonding of cyano groups with imidazole groups from neighboring molecules, dipolar coupling between two terminal cyano groups of neighboring molecules and attractive proton acceptor to ring interactions. With Co atoms, it formed an open porous coordination structure both at room temperature and at higher temperatures. On Au(111), the same self-assembled structure formed as that on Ag(111), driven by the same forces. After adding Co atoms, the porous networks formed through interaction between N_{cyano}-Co, $N_{imidazole}$-Co-N_{cyano} and NH···N. Similar porous network could be obtained with Fe atoms. On Cu(111), the self-assembly is stabilized by hydrogen bonding and two competitive coordination bonds, N_{cyano}-Cu-$N_{imidazole}$ bonds *vs.*$(N_{cyano})_3$-Cu. According to XPS data, the -NH of the imidazole dehydrogenate gradually with increasing temperature, till only the iminic N signal exists, suggesting that Cu adatoms coordinated with the iminic N. In this study, we find that Cu, Co and Fe adatoms prefer to coordinate with a terminal cyano group and an iminic N atom of the imidazole moiety rather than the most commonly reported multi-fold cyano coordination.

Biphenyl-4,4′-dihydroxamic acid (BPDH) was employed to fabricate two dimensional nanostructures on Ag(111) and Au(111), BPDH has a high degree of conformation flexibility owing to the possession of hydroxamic aicd group, which provides multiple bonding sites for self-assembly of versatile nanoarchitectures via hydrogen bonding. Close packed structures, as well as porous 2D networks form on Ag(111) and Au(111) surfaces. Particularly on the Ag(111) surface, an ordered porous structure with chiral crosses wetting the surface completely and a complex reticulated, polyporous network of high regularity featuring hexagrams were revealed, and a homogenous framework structures formed after annealing at annealing at 373 K. Open porous rectangular metal-coordination structure with Co atoms form on Au(111) and Ag(111), while six-fold and distorted metal-coordination structures formed on Ag(111). Furthermore, BPDH was studied on Cu(111), where various novel coordination structures exist on the surface. A densely packed structure, a four-fold coordination network and a fantastic hexagonal nanoarchitectures coexist on Cu(111) at room temperature. We also found rotational motion of molecular dimers in confined supramolecular hexagonal cavities at room temperature. After annealing at 333 K, all of structures turn into a six-fold coordination architecture. We could deduce that both the carbonyl and hydroxyl groups are involved into the coordination from the XPS result.

We have demonstrated hierarchical supramolecular coatings on solid surfaces via non-covalent bonds in this thesis. The coordination competition of cyano and imidazole group still needs to investigate further. The ordering of the networks formed by hydroxamic acids could be optimized as well as its functionalities.

8. Acknowledgements

Many people gave me support for the study and completion of the thesis, I am very grateful to all of them.

First of all, I want to thank my supervisor Prof. Dr. Johannes V. Barth, for his great support and giving me the opportunity to carry out the attractive research work at E20. Many thanks to Dr. Joachim Reichert, for his great help on experiment, offering insightful discussions, suggestions and supervision about the research. I extremely thank to Dr. Anthoula Papageorgiou. She has given me all-inclusive directions about the research. She offered great support during my PhD, from the project proposals to revising the thesis word by word. She is kind, energetic and enthusiastic, I will forever be grateful to her.

I would like to thank the whole team of VT-STM group, Dr. Li Jiang and Dr. Yuanyuan Guo, who introduced me the basic operation of STM, XPS and gave me helpful advices for experiment, as well as good cooperation on some projects. I also want to thank Dr. Chao Jing, she provided many meaningful suggestions for result analysis, also to Peter Knecht for good cooperation and discussions.

I also want to thank Andreas Walz for his great support on improvement of the UHV system and the apparatus. Thanks to Dr. Francesco Allegretti, Peter Deimel and Karl Eberle for the help in XPS measurements and valuable suggestions.

I am grateful to Dr. Guillaume Médard and Dr.Bernard Kuster from Proteomics and Bioanalytics group of TUM for offering the molecules that I can pursue various projects with.

I am also very grateful to thank Viktoria Blaschek, she gave me constant great and kind help in my daily work and life. Thanks to Max Glanz and Dr. Kund Seufert for assistance of computer and software.

Furthermore, I am grateful thanks to colleagues in my office, Aleksandr Baklanov, Dr. Jacob Ducke, Dr. Matin Schwarz, Mathias Pörtner, Peng Xie for the awesome working atmosphere. Also thanks to Yuxiang Gong for the great time during coffee break and lunch.

Finally, I especially thank my family, my parents who always give me unconditional love, encourage and support me. The most fortunate thing for me during the past years is marrying Fang Zhou, I truly thank to Fang for sharing happiness during good times and encouragement during my bad times.

9. List of Publications

1. Jiang, L., Zhang, B., Médard, G., Seitsonen, A.P., Haag, F., Allegretti, F., Reichert, J., Kuster, B., Barth, J.V. and Papageorgiou, A.C., 2017. N-Heterocyclic carbenes on close-packed coinage metal surfaces: bis-carbene metal adatom bonding scheme of monolayer films on Au, Ag and Cu. Chemical science, 8(12), pp.8301-8308.

2. Knecht, P., Suryadevara, N., Zhang, B., Reichert, J., Ruben, M., Barth, J.V., Klyatskaya, S. and Papageorgiou, A.C., 2018. The self-assembly and metal adatom coordination of a linear bis-tetrazole ligand on Ag (111). Chemical Communications, 54(72), pp.10072-10075.

3. Papageorgiou, A. C., Jiang L., Oh, S. C., Zhang, B., Sağlam, Ö., Guo, Y., ... & Barth, J. V., 2018. Tuning the ease of formation of on-surface metal-adatom coordination polymers featuring diketones. Nanoscale, 10(20), 9561-9568.

4. Zhang, B., Nadal, S., Médard, G., Jiang, L., Guo, Y., Allegretti, F., Reichert, J., Papageorgiou, A.C. and Barth, J.V. On-surface Assembly of a Chemoluminescent Module: Porous and Densely Packed Structures by Simultaneous Expression of Different Metal Coordination motifs, in preparation.

5. Jing, C., Zhang, B., Synkule, S., Ebrahimi, M., Riss, A., Auwärter, W., Jiang, L., Médard, G., Reichert, J., Barth, J.V. and Papageorgiou, A.C.. Hydroxamic Acid Linear Linkers for Molecular Surface Architectonics, in preparation.

6. Zhang, B., Jing, C., Médard, G., Jiang, L., Reichert, J., Barth, J.V. and Papageorgiou, A.C.. Two-Dimensional Architectures Based on Metal-Organic Coordination of Linear Bis-Hydroxamic Acid Linkers by Cobalt, in preparation.

7. Zhang, B., Jing, C., Médard, G., Jiang, L., Reichert, J., Barth, J.V. and Papageorgiou, A.C, Thermal Chemistry and Self-assembly of a Bihydroxamic Acid Linear Linker on Cu(111), in preparation

10. List of Figures

Figure 2.1: Schematic illustration of STM 8

Figure 2.2: Schematic of different views between classical and quantum physics 9

Figure 2.3: Illustration of a particle-wave tunneling through potential barrier. 9

Figure 2.4: Energy levels diagram shows tunneling current between tip and sample 11

Figure 2.5: The size and the DOS ρt (EF) of the tip 12

Figure 2.6: Schematic a piezo tube scanner. 13

Figure 2.7: Illustration of two scanning modes in scanning tunneling microscopy 13

Figure 2.8: Image of the apparatus of the variable-temperature of STM under UHV 15

Figure 2.9: Image of the metal sample holder 16

Figure 2.10: Image of OMBE with 4 independent crucibles 16

Figure 2.11: Image of home-built metal evaporator. 17

Figure 2.12: Schematic of Aarhus 150 VT-STM 18

Figure 2.13: Sketch of the etching process of tungsten tip. 18

Figure 2.14: Core electrons are excited by X-ray radiation 20

Figure 2.15: Inelastic mean free path versus the kinetic energy of the photoelectron 21

Figure 2.16: Working principle of XPS 21

Figure 2.17: Image of the XPS setup of TUM-WSI in Garching 22

Figure 2.18: Basic working principle of the ellipsoidal monochromator FOCUS 500 23

Figure 3.1: Molecular model and STM image of TCPI. 26

Figure 3.2: STM image of self-assembled structure on Ag(111) 27

Figure 3.3: STM image of submonolayer of TCPI with excessive Co on Ag(111) 28

Figure 3.4: STM image of the molecules on Au(111) at room temperature 29

Figure 3.5: Structures of TCPI with Co atoms on flat surface 30

Figure 3.6: XPS measurement of N 1s of TCPI at RT on Au(111) 31

Figure 3.7: XPS measurement of N 1s and Co 2p at RT on Au(111)...............................32

Figure 3.8: Blends of TCPI and Fe atoms on Au(111) 33

Figure 3.9: Self-assembled structure of TCPI on Cu(111) at room temperature 34

Figure 3.10: Annealing the monolayer of TCPI on Cu (111) 35

Figure 3.11: XP spectra of N1s for multilayer of TCPI on Cu(111) at room temperature.36

Figure 3.12: XP spectra of N1s of TCPI at RT on Cu(111)..36

Figure 4.1: Different forms pf Biphenyl-4,4′-dihydroxamic acid (BPDH). 40

Figure 4.2: Single BPDH on Ag(111) surface 41

Figure 4.3: STM topography of BPDH molecules on Au(111) substrate 42

Figure 4.4: Gas phase DFT geometry optimisation of BPDH 43

Figure 4.5: DFT geomtry optimisation and simulate nc-AFM images on Ag(111) 43

Figure 4.6: N1s signal of BPDH on Au(111) and Ag(111) 44

Figure 4.7:Close packed islands of BPDH molecules on Ag(111) substrate 46

Figure 4.8: nc-AFM close-packed BPDH molecules 47

Figure 4.9: Close up of BPDH nodes 47

Figure 4.10: Polyporous network of BPDH molecules on Ag(111) 48

Figure 4.11: Overview STM image of polyporous structure 49

Figure 4.12: Organizational chirality and different pores on Ag(111) 50

Figure 4.13: Cross network of BPDH molecules on Ag(111) 52

Figure 4.14: Ordering of cross networks in real and reciprocal space 53

Figure 4.15: Various pores in cross networks composed of different R and S nodes 53

Figure 5.1: STM images of Co atoms and BPDH molecules on the Au(111) 58

Figure 5.2: STM image of metal-organic network after annealing at 373 K on Au(111) .60

Figure 5.3: XPS measurements of N 1s and O 1s of BPDH adsorbed Au(111) 62

Figure 5.4: High resolution STM image 63

Figure 5.5: Metal-coordination of BPDH with Co on Ag (111) at room temperature.......64

Figure 5.6: Coordination network of BPDH: Co stoichiometry of 1 : 1 on Ag(111)........ 66

Figure 5.7: Random metal-ligand network after annealing at 520 K 67

Figure 5.8: XPS measurements of N 1s and O 1s of BPDH and Co adsorbed Ag(111) ... 68

Figure 6.1: Close-pack structure of BPDH at room temperature on Cu(111) 73

Figure 6.2: Porous metal-organic coordination structures on Cu(111) at RT.................... 74

Figure 6.3: Tentative atomic model of molecules of four-fold structure on Cu(111) 75

Figure 6.4: (A) High resolution STM image of the hexagonal molecular structure.......... 76

Figure 6.5: Rotational motion of molecular dimers in supramolecular cage...................... 77

Figure 6.6: Metal-organic nanoarchitecture after annealing at 333 K 78

Figure 6.7: X-ray photoelectron (XP) spectra of BPDH uptake on Cu(111) surface 80

Figure 6.8: XPS measurements of N 1s and O 1s regions on Cu(111) surface 81

11. List of Tables

Table 2.1: Details of molecules investigated in this thesis and related deposition temperatures. 19

12. List of Abbreviations

AFM. Atomic force microscopy

BPDH. 1,1´-biphenyl-4,4´-dihydroxamic acid

DFT. Density functional theory

DOS. Density of states

Fcc. Face centered cubic

FFT. Fast fourier transform

RT. Room temperature

SPM. Scanning probe microscopy

STM. Scanning tunneling microscopy

TCPI. 2,4,5-triphenyl-1H-imidazole

UHV. Ultra-high vacuum

VT-STM. Variable-temperature scanning tunneling microscopy

XPS. X-ray photoelectron spectroscopy

Bibliography

1. Feynman, R., *There's Plenty of Room at the Bottom.* Eng. Sci., 1960. **23**: p. 22-36.

2. Arthur, J.R., *Interaction of Ga and As2 Molecular Beams with Gaas Surfaces.* Journal of Applied Physics, 1968. **39**(8): p. 4032-4034.

3. McCray, W.P., *Mbe Deserves a Place in the History Books.* Nat. Nanotechnol., 2007. **2**(5): p. 259.

4. Suntola, T. and J. Antson, *Method for Producing Compound Thin Films*. 1977, DEPARTMENT OF THE NAVY WASHINGTON DC.

5. Eigler, D.M. and E.K. Schweizer, *Positioning Single Atoms with a Scanning Tunnelling Microscope.* Nature, 1990. **344**(6266): p. 524.

6. Jackman, R.J., J.L. Wilbur, and G.M. Whitesides, *Fabrication of Submicrometer Features on Curved Substrates by Microcontact Printing.* Science, 1995. **269**(5224): p. 664-666.

7. Novoselov, K.S., A.K. Geim, S. Morozov, D. Jiang, M. Katsnelson, I. Grigorieva, S. Dubonos, Firsov, and AA, *Two-Dimensional Gas of Massless Dirac Fermions in Graphene.* Nature, 2005. **438**(7065): p. 197.

8. Desai, S.B., S.R. Madhvapathy, A.B. Sachid, J.P. Llinas, Q. Wang, G.H. Ahn, G. Pitner, M.J. Kim, J. Bokor, and C. Hu, *Mos2 Transistors with 1-Nanometer Gate Lengths.* Science, 2016. **354**(6308): p. 99-102.

9. Wilbur, J.L., A. Kumar, E. Kim, and G.M. Whitesides, *Microfabrication by Microcontact Printing of Self‐Assembled Monolayers.* Adv. Mater., 1994. **6**(7‐8): p. 600-604.

10. Sirringhaus, H., T. Kawase, R. Friend, T. Shimoda, M. Inbasekaran, W. Wu, and E. Woo, *High-Resolution Inkjet Printing of All-Polymer Transistor Circuits.* Science, 2000. **290**(5499): p. 2123-2126.

11. Piner, R.D., J. Zhu, F. Xu, S. Hong, and C.A. Mirkin, *"Dip-Pen" Nanolithography.* Science, 1999. **283**(5402): p. 661-663.

12. Daniel, M.-C. and D. Astruc, *Gold Nanoparticles: Assembly, Supramolecular Chemistry, Quantum-Size-Related Properties, and Applications toward Biology, Catalysis, and Nanotechnology.* Chem. Rev., 2004. **104**(1): p. 293-346

13. Decher, G., B. Lehr, K. Lowack, Y. Lvov, and J. Schmitt, *New Nanocomposite Films for Biosensors: Layer-by-Layer Adsorbed Films of Polyelectrolytes, Proteins or DNA.* Biosensors and Bioelectronics, 1994. **9**(9-10): p. 677-684.

14. Cavallini, M., F. Biscarini, S. León, F. Zerbetto, G. Bottari, and D.A. Leigh, *Information Storage Using Supramolecular Surface Patterns.* Science, 2003. **299**(5606): p. 531-531.

15. Chia, S., J. Cao, J.F. Stoddart, and J.I. Zink, *Working Supramolecular Machines Trapped in Glass and Mounted on a Film Surface.* Angew. Chem., 2001. **113**(13): p. 2513-2517.

16. De Feyter, S. and F.C. De Schryver, *Two-Dimensional Supramolecular Self-Assembly Probed by Scanning Tunneling Microscopy.* Chem. Soc. Rev., 2003. **32**(3): p. 139-150.

17. Barth, J.V., J. Weckesser, C. Cai, P. Günter, L. Bürgi, O. Jeandupeux, and K. Kern, *Building Supramolecular Nanostructures at Surfaces by Hydrogen Bonding.* Angew. Chem., Int. Ed., 2000. **39**(7): p. 1230-1234.

18. Payer, D., A. Comisso, A. Dmitriev, T. Strunskus, N. Lin, C. Wöll, A. DeVita, J.V. Barth, and K. Kern, *Ionic Hydrogen Bonds Controlling Two‐Dimensional Supramolecular Systems at a Metal Surface.* Chem.- Eur. J., 2007. **13**(14): p. 3900-3906.

19. Anasori, B., M.R. Lukatskaya, and Y. Gogotsi, *2d Metal Carbides and Nitrides (Mxenes) for Energy Storage.* Nat. Rev. Mater., 2017. **2**(2): p. 16098.

20. Khan, A.H., S. Ghosh, B. Pradhan, A. Dalui, L.K. Shrestha, S. Acharya, and K. Ariga, *Two-Dimensional (2d) Nanomaterials Towards Electrochemical Nanoarchitectonics in Energy-Related Applications.* Bulletin of the Chemical Society of Japan, 2017. **90**(6): p. 627-648.

21. Zhao, K., S. Liu, G. Ye, Q. Gan, Z. Zhou, and Z. He, *High-Yield Bottom-up Synthesis of 2d Metal–Organic Frameworks and Their Derived Ultrathin Carbon Nanosheets for Energy Storage.* J. Mater. Chem. A , 2018. **6**(5): p. 2166-2175.

22. Zhang, M., G. Feng, Z. Song, Y.-P. Zhou, H.-Y. Chao, D. Yuan, T.T. Tan, Z. Guo, Z. Hu, and B.Z. Tang, *Two-Dimensional Metal–Organic Framework with Wide Channels and Responsive Turn-on Fluorescence for the Chemical Sensing of Volatile Organic Compounds.* J. Am. Chem. Soc., 2014. **136**(20): p. 7241-7244.

23. Rieter, W.J., K.M. Taylor, and W. Lin, *Surface Modification and Functionalization of Nanoscale Metal-Organic Frameworks for Controlled Release and Luminescence Sensing.* J. Am. Chem. Soc., 2007. **129**(32): p. 9852-9853.

24. Campbell, M.G., S.F. Liu, T.M. Swager, and M. Dincă, *Chemiresistive Sensor Arrays from Conductive 2d Metal–Organic Frameworks.* J. Am. Chem. Soc., 2015. **137**(43): p. 13780-13783.

25. Clough, A.J., J.W. Yoo, M.H. Mecklenburg, and S.C. Marinescu, *Two-Dimensional Metal–Organic Surfaces for Efficient Hydrogen Evolution from Water*. J. Am. Chem. Soc., 2014. **137**(1): p. 118-121.

26. Zhao, S., Y. Wang, J. Dong, C.-T. He, H. Yin, P. An, K. Zhao, X. Zhang, C. Gao, and L. Zhang, *Ultrathin Metal–Organic Framework Nanosheets for Electrocatalytic Oxygen Evolution.* Nature Energy, 2016. **1**(12): p. 16184.

27. Köster, R., J.-S. Hwang, C. Durand, D.L.S. Dang, and J. Eymery, *Self-Assembled Growth of Catalyst-Free Gan Wires by Metal–Organic Vapour Phase Epitaxy*. Nanotechnology, 2009. **21**(1): p. 015602.

28. Binnig, G. and H. Rohrer, *Scanning Tunneling Microscopy\Char22{}from Birth to Adolescence.* Reviews of Modern Physics, 1987. **59**(3): p. 615-625.

29. Binnig, G., H. Rohrer, C. Gerber, and E. Weibel, *Surface Studies by Scanning Tunneling Microscopy*. Phys. Rev. Lett., 1982. **49**(1): p. 57-61.

30. Binnig, G., H. Rohrer, C. Gerber, and E. Weibel, *7 *7 Reconstruction on Si(111) Resolved in Real Space.* Phys. Rev. Lett., 1983. **50**(2): p. 120-123.

31. Lyo, I.-W. and P. Avouris, *Field-Induced Nanometer-to Atomic-Scale Manipulation of Silicon Surfaces with the Stm.* Science, 1991. **253**(5016): p. 173-176.

32. Stroscio, J.A. and D. Eigler, *Atomic and Molecular Manipulation with the Scanning Tunneling Microscope.* Science, 1991. **254**(5036): p. 1319-1326.

33. Bartels, L., G. Meyer, and K.-H. Rieder, *Basic Steps of Lateral Manipulation of Single Atoms and Diatomic Clusters with a Scanning Tunneling Microscope Tip.* Phys. Rev. Lett., 1997. **79**(4): p. 697.

34. Cai, J., P. Ruffieux, R. Jaafar, M. Bieri, T. Braun, S. Blankenburg, M. Muoth, A.P. Seitsonen, M. Saleh, X. Feng, K. Mullen, and R. Fasel, *Atomically Precise Bottom-up Fabrication of Graphene Nanoribbons.* Nature, 2010. **466**(7305): p. 470-3.

35. Ugeda, M.M., A.J. Bradley, S.F. Shi, F.H. da Jornada, Y. Zhang, D.Y. Qiu, W. Ruan, S.K. Mo, Z. Hussain, Z.X. Shen, F. Wang, S.G. Louie, and M.F. Crommie, *Giant Bandgap Renormalization and Excitonic Effects in a Monolayer Transition Metal Dichalcogenide Semiconductor.* Nat. Mater., 2014. **13**(12): p. 1091-5.

36. Smith, D., A. Bryant, C. Quate, J. Rabe, C. Gerber, and J. Swalen, *Images of a Lipid Bilayer at Molecular Resolution by Scanning Tunneling Microscopy.* Proc. Natl. Acad. Sci. U. S. A., 1987. **84**(4): p. 969-972.

37. Lampa-Pastirk, S., J.P. Veazey, K.A. Walsh, G.T. Feliciano, R.J. Steidl, S.H. Tessmer, and G. Reguera, *Thermally Activated Charge Transport in Microbial Protein Nanowires.* Sci Rep, 2016. **6**: p. 23517.

38. Http://www.Iap.Tuwien.Ac.At/Www/Surface/Stm_Gallery/Stm_Schematic

39. Tersoff, J. and D.R. Hamann, *Theory and Application for the Scanning Tunneling Microscope.* Phys. Rev. Lett., 1983. **50**(25): p. 1998-2001.

40. Tersoff, J. and D. Hamann, *Theory of the Scanning Tunneling Microscope*, in *Scanning Tunneling Microscopy*. 1985, Springer. p. 59-67.

41. Meyer, E., H.J. Hug, and R. Bennewitz, *Introduction to Scanning Tunneling Microscopy*, in *Scanning Probe Microscopy*. 2004, Springer. p. 15-44.

42. Http://Physicsopenlab.Org/2017/05/30/Tunnel-Effect/.

43. Bardeen, J., *Tunnelling from a Many-Particle Point of View.* Phys. Rev. Lett., 1961. **6**(2): p. 57.

44. Chen, C.J., *Origin of Atomic Resolution on Metal Surfaces in Scanning Tunneling Microscopy.* Phys Rev Lett, 1990. **65**(4): p. 448-451.

45. Laegsgaard, E., L. Österlund, P. Thostrup, P.B. Rasmussen, I. Stensgaard, and F. Besenbacher, *A High-Pressure Scanning Tunneling Microscope.* Rev. Sci. Instrum., 2001. **72**(9): p. 3537-3542.

46. Besenbacher, F., E. Lægsgaard, and I. Stensgaard, *Fast-Scanning Stm Studies.* Materials Today, 2005. **8**(5): p. 26-30.

47. Weissler, G. and R.W. Carlson, *Vacuum Physics and Technology*. Vol. 14. 1980: Academic Press.

48. Fischer, S., *Combined Stm and X-Ray Spectroscopy Study of Surface-Confined Biologically Relevant Molecules.* 2013.

49. Horcas, I., R. Fernandez, J.M. Gomez-Rodriguez, J. Colchero, J. Gomez-Herrero, and A.M. Baro, *Wsxm: A Software for Scanning Probe Microscopy and a Tool for Nanotechnology.* Rev Sci Instrum, 2007. **78**(1): p. 013705.

50. Chusuei, C.C. and D.W. Goodman, *X-Ray Photoelectron Spectroscopy.* Encyclopedia of physical science and technology, 2002. **17**: p. 921-938.

51. Theobald, J.A., N.S. Oxtoby, M.A. Phillips, N.R. Champness, and P.H. Beton, *Controlling Molecular Deposition and Layer Structure with Supramolecular Surface Assemblies.* Nature, 2003. **424**(6952): p. 1029-1031.

52. Llanes-Pallas, A., M. Matena, T. Jung, M. Prato, M. Stohr, and D. Bonifazi, *Trimodular Engineering of Linear Supramolecular Miniatures on Ag(111) Surfaces Controlled by Complementary Triple Hydrogen Bonds.* Angew. Chem. Int. Ed. Engl., 2008. **47**(40): p. 7726-30.

53. Rahsepar, F.R., N. Moghimi, and K.T. Leung, *Surface-Mediated Hydrogen Bonding of Proteinogenic Alpha-Amino Acids on Silicon.* Acc Chem Res, 2016. **49**(5): p. 942-51.

54. Yokoyama, T., S. Yokoyama, T. Kamikado, Y. Okuno, and S. Mashiko, *Selective Assembly on a Surface of Supramolecular Aggregates with Controlled Size and Shape.* Nature, 2001. **413**(6856): p. 619-621.

55. Shimizu, T.K., J. Jung, H. Imada, and Y. Kim, *Supramolecular Assembly through Interactions between Molecular Dipoles and Alkali Metal Ions.* Angew. Chem. Int. Ed. Engl., 2014. **53**(50): p. 13729-33.

56. Baber, A.E., S.C. Jensen, and E.C.H. Sykes, *Dipole-Driven Ferroelectric Assembly of Styrene on Au {111}.* J. Am. Chem. Soc., 2007. **129**(20): p. 6368-6369.

57. Langner, A., S.L. Tait, N. Lin, C. Rajadurai, M. Ruben, and K. Kern, *Self-Recognition and Self-Selection in Multicomponent Supramolecular Coordination Networks on Surfaces.* Proc Natl Acad Sci U S A, 2007. **104**(46): p. 17927-30.

58. Lin, N., A. Dmitriev, J. Weckesser, J.V. Barth, and K. Kern, *Real‐Time Single‐Molecule Imaging of the Formation and Dynamics of Coordination Compounds.* Angew. Chem., Int. Ed., 2002. **41**(24): p. 4779-4783.

59. Heim, D., D. Ecija, K. Seufert, W. Auwärter, C. Aurisicchio, C. Fabbro, D. Bonifazi, and J.V. Barth, *Self-Assembly of Flexible One-Dimensional Coordination Polymers on Metal Surfaces.* J. Am. Chem. Soc., 2010. **132**(19): p. 6783-6790.

60. Ecija, D., M. Marschall, J. Reichert, A. Kasperski, D. Nieckarz, P. Szabelski, W. Auwärter, and J.V. Barth, *Dynamics and Thermal Stability of Surface-Confined Metal–Organic Chains.* Surf. Sci., 2016. **643**: p. 91-97.

61. Dmitriev, A., H. Spillmann, N. Lin, J.V. Barth, and K. Kern, *Modular Assembly of Two‐Dimensional Metal‐Organic Coordination Networks at a Metal Surface.* Angew. Chem., 2003. **115**(23): p. 2774-2777.

62. Barth, J.V., *Molecular Architectonic on Metal Surfaces.* Annu Rev Phys Chem, 2007. **58**: p. 375-407.

63. Bebensee, F., K. Svane, C. Bombis, F. Masini, S. Klyatskaya, F. Besenbacher, M. Ruben, B. Hammer, and T.R. Linderoth, *A Surface Coordination Network Based on Copper Adatom Trimers.* Angew. Chem., Int. Ed., 2014. **53**(47): p. 12955-12959.

64. Della Pia, A., M. Riello, J. Lawrence, D. Stassen, T.S. Jones, D. Bonifazi, A. De Vita, and G. Costantini, *Two-Dimensional Ketone-Driven Metal-Organic Coordination on Cu(111).* Chemistry - A European Journal, 2016. **22**(24): p. 8105-8112.

65. Kim, H., Y.H. Chang, S.-H. Lee, Y.-H. Kim, and S.-J. Kahng, *Switching and Sensing Spin States of Co–Porphyrin in Bimolecular Reactions on Au (111) Using Scanning Tunneling Microscopy.* ACS Nano, 2013. **7**(10): p. 9312-9317.

66. Fabris, S., S. Stepanow, N. Lin, P. Gambardella, A. Dmitriev, J. Honolka, S. Baroni, and K. Kern, *Oxygen Dissociation by Concerted Action of Di-Iron Centers in Metal-Organic Coordination Networks at Surfaces: Modeling Non-Heme Iron Enzymes.* Nano Lett, 2011. **11**(12): p. 5414-20.

67. Skomski, D., C.D. Tempas, K.A. Smith, and S.L. Tait, *Redox-Active on-Surface Assembly of Metal-Organic Chains with Single-Site Pt(Ii).* J Am Chem Soc, 2014. **136**(28): p. 9862-5.

68. Yang, H.-H., Y.-H. Chu, C.-I. Lu, T.-H. Yang, K.-J. Yang, C.-C. Kaun, G. Hoffmann, and M.-T. Lin, *Digitized Charge Transfer Magnitude Determined by Metal–Organic Coordination Number.* ACS Nano, 2013. **7**(3): p. 2814-2819.

69. Tseng, T.-C., C. Lin, X. Shi, S.L. Tait, X. Liu, U. Starke, N. Lin, R. Zhang, C. Minot, M.A. Van Hove, J.I. Cerdá, and K. Kern, *Two-Dimensional Metal-Organic Coordination Networks of Mn-7,7,8,8-Tetracyanoquinodimethane Assembled on Cu(100): Structural, Electronic, and Magnetic Properties.* Phys. Rev. B, 2009. **80**(15).

70. Wang, L., H. Kong, C. Zhang, Q. Sun, L. Cai, Q. Tan, F. Besenbacher, and W. Xu, *Formation of a G-Quartet-Fe Complex and Modulation of Electronic and Magnetic Properties of the Fe Center.* ACS Nano, 2014. **8**(11): p. 11799-11805.

71. Nakashima, K., *Lophine Derivatives as Versatile Analytical Tools.* Biomed Chromatogr, 2003. **17**(2-3): p. 83-95.

72. Saravanan, K., N. Srinivasan, V. Thanikachalam, and J. Jayabharathi, *Synthesis and Photophysics of Some Novel Imidazole Derivatives Used as Sensitive Fluorescent Chemisensors.* J Fluoresc, 2011. **21**(1): p. 65-80.

73. Alves, J., A. Boaro, J.S. da Silva, T.L. Ferreira, V.B. Keslarek, C.A. Cabral, R.B. Orfao, Jr., L.F. Ciscato, and F.H. Bartoloni, *Lophine Derivatives as Activators in Peroxyoxalate Chemiluminescence.* Photochem Photobiol Sci, 2015. **14**(2): p. 320-8.

74. Tsunenaga, M., H. Iga, and M. Kimura, *Location Effect of an Oh Group on the Chemiluminescence Efficiency of 4-Hydroperoxy-2-(O-, M-, or P-Hydroxyphenyl)-4,5-Diphenyl-4h-Isoimidazoles.* Tetrahedron Lett., 2005. **46**(11): p. 1877-1880.

75. Kimura, M., G.H. Lu, H. Nishigawa, Z.Q. Zhang, and Z.Z. Hu, *Singlet Oxygen Generation from Lophine Hydroperoxides.* Luminescence, 2007. **22**(2): p. 72-6.

76. Lu, G., J. Wada, T. Kimoto, H. Iga, H. Nishigawa, M. Kimura, and Z. Hu, *The Chemiexcitation of the Chemiluminescence of Lophine Peroxide Anions Via a Partially Cyclic Transition State.* European Journal of Organic Chemistry, 2014. **2014**(6): p. 1212-1219.

77. Fridman, N., M. Kaftory, and S. Speiser, *Structures and Photophysics of Lophine and Double Lophine Derivatives.* Sens. Actuators, B, 2007. **126**(1): p. 107-115.

78. Ichibangase, T., Y. Ohba, N. Kishikawa, K. Nakashima, and N. Kuroda, *Evaluation of Lophine Derivatives as L-012 (Luminol Analog)-Dependent Chemiluminescence Enhancers for Measuring Horseradish Peroxidase and H2o2.* Luminescence, 2014. **29**(2): p. 118-21.

79. Hariharasubramanian, A. and Y.D. Ravichandran, *Synthesis and Studies of Electrochemical Properties of Lophine Derivatives.* RSC Adv., 2014. **4**(97): p. 54740-54746.

80. Camas-Anzueto, J.L., J.A. Gómez-Valdéz, R. Meza-Gordillo, M. Pérez-Patricio, H.R. Hernández de León, and V. León-Orozco, *Sensitive Layer Based on Lophine and Calcium Hydroxide for Detection of Dissolved Oxygen in Water.* Measurement, 2015. **68**: p. 280-285.

81. Baker, B. and M. Stöhr, *Role of Cyano Groups in the Self-Assembly of Organic Molecules on Metal Surfaces.*

82. Yokoyama, T., S. Yokoyama, T. Kamikado, Y. Okuno, and S. Mashiko, *Selective Assembly on a Surface of Supramolecular Aggregates with Controlled Size and Shape.* Nature, 2001. **413**(6856): p. 619.

83. Arras, E., A.P. Seitsonen, F. Klappenberger, and J.V. Barth, *Nature of the Attractive Interaction between Proton Acceptors and Organic Ring Systems.* Phys Chem Chem Phys, 2012. **14**(46): p. 15995-6001.

84. Schlickum, U., R. Decker, F. Klappenberger, G. Zoppellaro, S. Klyatskaya, M. Ruben, I. Silanes, A. Arnau, K. Kern, and H. Brune, *Metal− Organic Honeycomb Nanomeshes with Tunable Cavity Size.* Nano Lett., 2007. **7**(12): p. 3813-3817.

85. Lázaro Martínez, J.M., E. Rodríguez-Castellón, R.M.T. Sánchez, L.R. Denaday, G.Y. Buldain, and V. Campo Dall' Orto, *Xps Studies on the Cu(I,Ii)–Polyampholyte Heterogeneous Catalyst: An Insight into Its Structure and Mechanism.* J. Mol. Catal. A: Chem., 2011. **339**(1-2): p. 43-51.

86. Muller, K., J.C. Moreno-Lopez, S. Gottardi, U. Meinhardt, H. Yildirim, A. Kara, M. Kivala, and M. Stohr, *Cyano-Functionalized Triarylamines on Coinage Metal Surfaces: Interplay of Intermolecular and Molecule-Substrate Interactions.* Chemistry, 2016. **22**(2): p. 581-9.

87. Liu, W., K.L. Koh, J. Lu, L. Yang, S. Phua, J. Kong, Z. Chen, and X. Lu, *Simultaneous Catalyzing and Reinforcing Effects of Imidazole-Functionalized Graphene in Anhydride-Cured Epoxies.* J. Mater. Chem., 2012. **22**(35): p. 18395.

88. Pham, T.A., F. Song, M.N. Alberti, M.T. Nguyen, N. Trapp, C. Thilgen, F. Diederich, and M. Stohr, *Heat-Induced Formation of One-Dimensional Coordination Polymers on Au(111): An Stm Study.* Chem Commun (Camb), 2015. **51**(77): p. 14473-6.

89. Weber, P.B., R. Hellwig, T. Paintner, M. Lattelais, M. Paszkiewicz, P. Casado Aguilar, P.S. Deimel, Y. Guo, Y.Q. Zhang, F. Allegretti, A.C. Papageorgiou, J. Reichert, S. Klyatskaya, M. Ruben, J.V. Barth, M.L. Bocquet, and F. Klappenberger, *Surface-Guided Formation of an Organocobalt Complex.* Angew Chem Int Ed Engl, 2016. **55**(19): p. 5754-9.

90. Li, J., C. Wäckerlin, S. Schnidrig, E. Joliat, R. Alberto, and K.H. Ernst, *On‐Surface Metalation and 2d Self‐Assembly of Pyrphyrin Molecules into Metal‐*

Coordinated Networks on Cu (111). Helvetica Chimica Acta, 2017. **100**(1): p. e1600278.

91. Yeh, J. and I. Lindau, *Atomic Subshell Photoionization Cross Sections and Asymmetry Parameters: 1⩽ Z⩽ 103.* Atomic data and nuclear data tables, 1985. **32**(1): p. 1-155.

92. Li, Y., J. Xiao, T.E. Shubina, M. Chen, Z. Shi, M. Schmid, H.P. Steinruck, J.M. Gottfried, and N. Lin, *Coordination and Metalation Bifunctionality of Cu with 5,10,15,20-Tetra(4-Pyridyl)Porphyrin: Toward a Mixed-Valence Two-Dimensional Coordination Network.* J Am Chem Soc, 2012. **134**(14): p. 6401-8.

93. Lukasczyk, T., K. Flechtner, L.R. Merte, N. Jux, F. Maier, J.M. Gottfried, and H.-P. Steinrück, *Interaction of Cobalt (Ii) Tetraarylporphyrins with a Ag (111) Surface Studied with Photoelectron Spectroscopy.* J. Phys. Chem. C, 2007. **111**(7): p. 3090-3098.

94. Bansmann, J., S. Baker, C. Binns, J. Blackman, J. Bucher, J. Dorantesdavila, V. Dupuis, L. Favre, D. Kechrakos, and A. Kleibert, *Magnetic and Structural Properties of Isolated and Assembled Clusters.* Surf. Sci. Rep., 2005. **56**(6-7): p. 189-275.

95. Clair, S., S. Pons, H. Brune, K. Kern, and J.V. Barth, *Mesoscopic Metallosupramolecular Texturing by Hierarchic Assembly.* Angew. Chem., 2005. **117**(44): p. 7460-7463.

96. Bouju, X., C. Mattioli, G. Franc, A. Pujol, and A. Gourdon, *Bicomponent Supramolecular Architectures at the Vacuum-Solid Interface.* Chem. Rev., 2017. **117**(3): p. 1407-1444.

97. Goronzy, D.P., M. Ebrahimi, F. Rosei, Arramel, Y. Fang, S. De Feyter, S.L. Tait, C. Wang, P.H. Beton, A.T.S. Wee, P.S. Weiss, and D.F. Perepichka, *Supramolecular Assemblies on Surfaces: Nanopatterning, Functionality, and Reactivity.* ACS Nano, 2018. **12**(8): p. 7445-7481.

98. Mali, K.S., N. Pearce, S. De Feyter, and N.R. Champness, *Frontiers of Supramolecular Chemistry at Solid Surfaces.* Chem. Soc. Rev., 2017. **46**(9): p. 2520-2542.

99. Sosa-Vargas, L., E. Kim, and A.J. Attias, *Beyond "Decorative" 2d Supramolecular Self-Assembly: Strategies Towards Functional Surfaces for Nanotechnology.* Mater. Horiz., 2017. **4**(4): p. 570-583.

100. Shang, J., Y. Wang, M. Chen, J. Dai, X. Zhou, J. Kuttner, G. Hilt, X. Shao, J.M. Gottfried, and K. Wu, *Assembling Molecular Sierpiński Triangle Fractals.* Nat. Chem., 2015. **7**: p. 389.

101. Cheng, F., X.-J. Wu, Z. Hu, X. Lu, Z. Ding, Y. Shao, H. Xu, W. Ji, J. Wu, and K.P. Loh, *Two-Dimensional Tessellation by Molecular Tiles Constructed from Halogen–Halogen and Halogen–Metal Networks.* Nat. Commun., 2018. **9**(1): p. 4871.

102. Écija, D., J.I. Urgel, A.P. Seitsonen, W. Auwärter, and J.V. Barth, *Lanthanide-Directed Assembly of Interfacial Coordination Architectures–from Complex Networks to Functional Nanosystems.* Acc. Chem. Res., 2018. **51**(2): p. 365-375.

103. Kakkar, R., *Theoretical Studies on Hydroxamic Acids.* 2013: p. 19-53.

104. Manal, M., M.J.N. Chandrasekar, J. Gomathi Priya, and M.J. Nanjan, *Inhibitors of Histone Deacetylase as Antitumor Agents: A Critical Review.* Bioorg. Chem., 2016. **67**: p. 18-42.

105. Rudshteyn, B., C.F.A. Negre, R.S. Oliboni, A. Monti, J. Chen, R.H. Crabtree, L.G.C. Rego, and V.S. Batista, *Inferring Protonation States of Hydroxamate Adsorbates on TiO_2 Surfaces.* J. Phys. Chem. C, 2017. **121**(22): p. 11985-11990.

106. Higashino, T., Y. Kurumisawa, N. Cai, Y. Fujimori, Y. Tsuji, S. Nimura, D.M. Packwood, J. Park, and H. Imahori, *A Hydroxamic Acid Anchoring Group for Durable Dye-Sensitized Solar Cells Incorporating a Cobalt Redox Shuttle.* ChemSusChem, 2017. **10**(17): p. 3347-3351.

107. Aung, S.H., Y. Hao, T.Z. Oo, and G. Boschloo, *2-(4-Butoxyphenyl)-N-Hydroxyacetamide: An Efficient Preadsorber for Dye-Sensitized Solar Cells.* ACS Omega, 2017. **2**(5): p. 1820-1825.

108. Tieu, W., T. Lifa, A. Katsifis, and R. Codd, *Octadentate Zirconium(Iv)-Loaded Macrocycles with Varied Stoichiometry Assembled from Hydroxamic Acid Monomers Using Metal-Templated Synthesis.* Inorg. Chem., 2017. **56**(6): p. 3719-3728.

109. Folkers, J.P., C.B. Gorman, P.E. Laibinis, S. Buchholz, G.M. Whitesides, and R.G. Nuzzo, *Self-Assembled Monolayers of Long-Chain Hydroxamic Acids on the Native Oxides of Metals.* Langmuir, 1995. **11**(3): p. 813-824.

110. Kaur, D. and R. Kohli, *Understanding Hydrogen Bonding of Hydroxamic Acids with Some Amino Acid Side Chain Model Molecules.* Struct. Chem., 2011. **23**(1): p. 161-173.

111. Kaur, D. and R. Kohli, *Hydrogen Bond Cooperativity in Dimers of Hydroxamic Acids.* Int. J. Quantum Chem., 2011. **111**(12): p. 2931-2943.

112. Schuler, B., W. Liu, A. Tkatchenko, N. Moll, G. Meyer, A. Mistry, D. Fox, and L. Gross, *Adsorption Geometry Determination of Single Molecules by Atomic Force Microscopy.* Phys. Rev. Lett., 2013. **111**(10): p. 106103.

113. Kawai, S., S. Nakatsuka, T. Hatakeyama, R. Pawlak, T. Meier, J. Tracey, E. Meyer, and A.S. Foster, *Multiple Heteroatom Substitution to Graphene Nanoribbon.* Sci. Adv., 2018. **4**(4): p. eaar7181.

114. Ellner, M., P. Pou, and R. Pérez, *Molecular Identification, Bond Order Discrimination, and Apparent Intermolecular Features in Atomic Force Microscopy Studied with a Charge Density Based Method.* ACS Nano, 2019. **13**(1): p. 786-795.

115. Krull, C., M. Castelli, P. Hapala, D. Kumar, A. Tadich, M. Capsoni, M.T. Edmonds, J. Hellerstedt, S.A. Burke, P. Jelinek, and A. Schiffrin, *Iron-Based Trinuclear Metal-Organic Nanostructures on a Surface with Local Charge Accumulation.* Nat. Commun., 2018. **9**(1): p. 3211.

116. Kakkar, R., R. Grover, and P. Chadha, *Conformational Behavior of Some Hydroxamic Acids.* Org. Biomol. Chem., 2003. **1**: p. 2200-2206.

117. Zhu, N., T. Osada, and T. Komeda, *Supramolecular Assembly of Biphenyl Dicarboxylic Acid on Au(111).* Surf. Sci., 2007. **601**(8): p. 1789-1794.

118. Xiao, W.D., Y.H. Jiang, K. Ait-Mansour, P. Ruffieux, H.J. Gao, and R. Fasel, *Chiral Biphenyldicarboxylic Acid Networks Stabilized by Hydrogen Bonding.* J. Phys. Chem. C, 2010. **114**(14): p. 6646-6649.

119. Schmitt, T., L. Hammer, and M.A. Schneider, *Evidence for on-Site Carboxylation in the Self-Assembly of 4,4 '-Biphenyl Dicarboxylic Acid on Cu(111).* J. Phys. Chem. C, 2016. **120**(2): p. 1043-1048.

120. Schwarz, D., R. van Gastel, H.J.W. Zandvliet, and B. Poelsema, *In Situ Observation of a Deprotonation-Driven Phase Transformation: 4,4'-Biphenyldicarboxylic Acid on Au(111).* J. Phys. Chem. C, 2013. **117**(2): p. 1020-1029.

121. Quiroga Argañaraz, B., L.J. Cristina, L.M. Rodríguez, A. Cossaro, A. Verdini, L. Floreano, J.D. Fuhr, J.E. Gayone, and H. Ascolani, *Ubiquitous Deprotonation of Terephthalic Acid in the Self-Assembled Phases on Cu(100).* Phys. Chem. Chem. Phys., 2018. **20**(6): p. 4329-4339.

122. Papageorgiou, A.C., S. Fischer, J. Reichert, K. Diller, F. Blobner, F. Klappenberger, F. Allegretti, A.P. Seitsonen, and J.V. Barth, *Chemical Transformations Drive Complex Self-Assembly of Uracil on Close-Packed Coinage Metal Surfaces.* ACS Nano, 2012. **6**(3): p. 2477-2486.

123. Kelly, R.E.A. and L.N. Kantorovich, *Hexagonal Adenine Networks Constructed from Their Homopairings.* Surf. Sci., 2005. **589**(1): p. 139-152.

124. Kelly, R.E.A. and L.N. Kantorovich, *Homopairing Possibilities of the DNA Base Thymine and the Rna Base Uracil: An Ab Initio Density Functional Theory Study.* J. Phys. Chem. B, 2006. **110**(5): p. 2249-2255.

125. van der Lit, J., F. Di Cicco, P. Hapala, P. Jelinek, and I. Swart, *Submolecular Resolution Imaging of Molecules by Atomic Force Microscopy: The Influence of the Electrostatic Force.* Phys. Rev. Lett., 2016. **116**(9): p. 096102.

126. Barlow, S.M. and R. Raval, *Complex Organic Molecules at Metal Surfaces: Bonding, Organisation and Chirality.* Surf. Sci. Rep., 2003. **50**(6-8): p. 201-341.

127. Teyssandier, J., S.D. Feyter, and K.S. Mali, *Host–Guest Chemistry in Two-Dimensional Supramolecular Networks.* Chem. Commun., 2016. **52**(77): p. 11465-11487.

128. Papageorgiou, A.C., J. Li, S.C. Oh, B. Zhang, Ö. Sağlam, Y. Guo, J. Reichert, A.B. Marco, D. Cortizo-Lacalle, A. Mateo-Alonso, and J.V. Barth, *Tuning the Ease of Diketones.* Nanoscale, 2018. **10**(20): p. 9561-9568.

129. De Marchi, F., G. Galeotti, M. Simenas, E.E. Tornau, A. Pezzella, J. MacLeod, M. Ebrahimi, and F. Rosei, *Room-Temperature Surface-Assisted Reactivity of a Melanin Precursor: Silver Metal–Organic Coordination Versus Covalent Dimerization on Gold.* Nanoscale, 2018. **10**(35): p. 16721-16729.

130. Stepanow, S., N. Lin, D. Payer, U. Schlickum, F. Klappenberger, G. Zoppellaro, M. Ruben, H. Brune, J.V. Barth, and K. Kern, *Surface-Assisted Assembly of 2d Metal-Organic Networks That Exhibit Unusual Threefold Coordination Symmetry.* Angew. Chem., Int. Ed., 2007. **46**(5): p. 710-713.

131. Zhang, Y.-Q., T. Lin, B. Cirera, R. Hellwig, C.-A. Palma, Z. Chen, M. Ruben, J.V. Barth, and F. Klappenberger, *One-Dimensionally Disordered Chiral Sorting by Racemic Tiling in a Surface-Confined Supramolecular Assembly of Achiral Tectons.* Angew. Chem., Int. Ed., 2017. **56**(27): p. 7797-7802.

132. Méthivier, C., V. Humblot, and C.-M. Pradier, *Uhv Deposition of the Gly-Pro Dipeptide on Cu(110) by Sublimation or Electrospray Ionization.* J. Phys. Chem. C, 2016. **120**(48): p. 27364-27368.

133. Leus, K., Y.-Y. Liu, and P. Van Der Voort, *Metal-Organic Frameworks as Selective or Chiral Oxidation Catalysts.* Catalysis Reviews, 2014. **56**(1): p. 1-56.

134. Ruben, M., J. Rojo, F.J. Romero-Salguero, L.H. Uppadine, and J.-M. Lehn, *Metallionen-Gitterarchitekturen: Funktionelle Supramolekulare Metallkomplexe.* Angew. Chem., 2004. **116**(28): p. 3728-3747.

135. Lux, L., K. Williams, and S. Ma, *Heat-Treatment of Metal–Organic Frameworks for Green Energy Applications.* CrystEngComm, 2015. **17**(1): p. 10-22.

136. Tang, Y.J., M.R. Gao, C.H. Liu, S.L. Li, H.L. Jiang, Y.Q. Lan, M. Han, and S.H. Yu, *Porous Molybdenum ‐ Based Hybrid Catalysts for Highly Efficient Hydrogen Evolution.* Angew. Chem., 2015. **127**(44): p. 13120-13124.

137. Lopez-Cabrelles, J., S. Manas-Valero, I.J. Vitorica-Yrezabal, P.J. Bereciartua, J.A. Rodriguez-Velamazan, J.C. Waerenborgh, B.J.C. Vieira, D. Davidovikj, P.G. Steeneken, H.S.J. van der Zant, G. Minguez Espallargas, and E. Coronado, *Isoreticular Two-Dimensional Magnetic Coordination Polymers Prepared through Pre-Synthetic Ligand Functionalization.* Nat. Chem., 2018. **10**(10): p. 1001-1007.

138. Ecija, D., S. Vijayaraghavan, W. Auwärter, S. Joshi, K. Seufert, C. Aurisicchio, D. Bonifazi, and J.V. Barth, *Two-Dimensional Short-Range Disordered Crystalline Networks from Flexible Molecular Modules.* ACS Nano, 2012. **6**(5): p. 4258-4265.

139. Kong, H., C. Zhang, L. Xie, L. Wang, and W. Xu, *Constitutional Dynamics of Metal-Organic Motifs on a Au(111) Surface.* Angew. Chem. Int. Ed. Engl., 2016. **55**(25): p. 7157-60.

140. Liu, J., T. Lin, Z. Shi, F. Xia, L. Dong, P.N. Liu, and N. Lin, *Structural Transformation of Two-Dimensional Metal-Organic Coordination Networks Driven by Intrinsic in-Plane Compression.* J. Am. Chem. Soc., 2011. **133**(46): p. 18760-6.

141. Dmitriev, A., H. Spillmann, N. Lin, J.V. Barth, and K. Kern, *Modular Assembly of Two-Dimensional Metal-Organic Coordination Networks at a Metal Surface.* Angew. Chem. Int. Ed. Engl., 2003. **42**(23): p. 2670-3.

142. Pivetta, M., G.E. Pacchioni, E. Fernandes, and H. Brune, *Temperature-Dependent Self-Assembly of Nc-Ph5-Cn Molecules on Cu(111).* J Chem Phys, 2015. **142**(10): p. 101928.

143. Tseng, T.-C., N. Abdurakhmanova, S. Stepanow, and K. Kern, *Hierarchical Assembly and Reticulation of Two-Dimensional Mn- and Ni–Tcnqx (X = 1, 2, 4) Coordination Structures on a Metal Surface.* J. Phys. Chem. C, 2011. **115**(20): p. 10211-10217.

144. Urgel, J.I., D. Ecija, W. Auwärter, D. Stassen, D. Bonifazi, and J.V. Barth, *Orthogonal Insertion of Lanthanide and Transition‐Metal Atoms in Metal‐Organic Networks on Surfaces.* Angew. Chem., Int. Ed., 2015. **54**(21): p. 6163-6167.

145. Yan, B., *Lanthanide-Functionalized Metal–Organic Framework Hybrid Systems to Create Multiple Luminescent Centers for Chemical Sensing.* Acc. Chem. Res., 2017. **50**(11): p. 2789-2798.

146. Kitagawa, S., R. Kitaura, and S.i. Noro, *Functional Porous Coordination Polymers.* Angew. Chem., Int. Ed., 2004. **43**(18): p. 2334-2375.

147. Xu, W., J.-g. Wang, M. Yu, E. Lægsgaard, I. Stensgaard, T.R. Linderoth, B. Hammer, C. Wang, and F. Besenbacher, *Guanine-and Potassium-Based Two-Dimensional Coordination Network Self-Assembled on Au (111).* J. Am. Chem. Soc., 2010. **132**(45): p. 15927-15929.

148. Classen, T., G. Fratesi, G. Costantini, S. Fabris, F.L. Stadler, C. Kim, S. de Gironcoli, S. Baroni, and K. Kern, *Templated Growth of Metal–Organic Coordination Chains at Surfaces.* Angew. Chem., Int. Ed., 2005. **44**(38): p. 6142-6145.

149. Nijs, T., Y.M. Klein, S.F. Mousavi, A. Ahsan, S. Nowakowska, E.C. Constable, C.E. Housecroft, and T.A. Jung, *The Different Faces of 4'-Pyrimidinyl-Functionalized 4,2':6',4''-Terpyridines: Metal-Organic Assemblies from Solution and on Au(111) and Cu(111) Surface Platforms.* J. Am. Chem.Soc., 2018. **140**(8): p. 2933-2939.

150. Knecht, P., N. Suryadevara, B. Zhang, J. Reichert, M. Ruben, J.V. Barth, S. Klyatskaya, and A.C. Papageorgiou, *The Self-Assembly and Metal Adatom Coordination of a Linear Bis-Tetrazole Ligand on Ag (111).* Chem. Commun., 2018. **54**(72): p. 10072-10075.

151. Moradi, M., L.G. Tulli, J. Nowakowski, M. Baljozovic, T.A. Jung, and P. Shahgaldian, *Two-Dimensional Calix[4]Arene-Based Metal-Organic Coordination Networks of Tunable Crystallinity.* Angew. Chem. Int. Ed. Engl., 2017. **56**(46): p. 14395-14399.

152. Dmitriev, A., N. Lin, J. Weckesser, J. Barth, and K. Kern, *Supramolecular Assemblies of Trimesic Acid on a Cu (100) Surface.* J. Phys. Chem. B, 2002. **106**(27): p. 6907-6912.

153. Li, Q., B. Yang, J. Björk, Q. Zhong, H. Ju, J. Zhang, N. Cao, Z. Shi, H. Zhang, and D. Ebeling, *Hierarchical Dehydrogenation Reactions on a Copper Surface.* J. Am. Chem. Soc., 2018. **140**(19): p. 6076-6082.

154. Powell, P., G. Cline, C. Reid, and P. Szaniszlo, *Occurrence of Hydroxamate Siderophore Iron Chelators in Soils.* Nature, 1980. **287**(5785): p. 833.

155. Kurzak, B., H. Kozłowski, and E. Farkas, *Hydroxamic and Aminohydroxamic Acids and Their Complexes with Metal Ions.* Coord. Chem. Rev., 1992. **114**(2): p. 169-200.

156. Lee, K., D. Archibald, J. McLean, and M.A. Reuter, *Flotation of Mixed Copper Oxide and Sulphide Minerals with Xanthate and Hydroxamate Collectors.* Minerals Engineering, 2009. **22**(4): p. 395-401.

157. Porter, N.J., A. Mahendran, R. Breslow, and D.W. Christianson, *Unusual Zinc-Binding Mode of HDAC6-Selective Hydroxamate Inhibitors.* Proc Natl Acad Sci U S A, 2017. **114**(51): p. 13459-13464.

158. Wu, R., Z. Lu, Z. Cao, and Y. Zhang, *Zinc Chelation with Hydroxamate in Histone Deacetylases Modulated by Water Access to the Linker Binding Channel.* J. Am. Chem. Soc., 2011. **133**(16): p. 6110-3.

159. Leipoldt, F., J. Santos-Aberturas, D.P. Stegmann, F. Wolf, A. Kulik, R. Lacret, D. Popadic, D. Keinhorster, N. Kirchner, P. Bekiesch, H. Gross, A.W. Truman, and L. Kaysser, *Warhead Biosynthesis and the Origin of Structural Diversity in Hydroxamate Metalloproteinase Inhibitors.* Nat. Commun., 2017. **8**(1): p. 1965.

160. Higashino, T., Y. Kurumisawa, N. Cai, Y. Fujimori, Y. Tsuji, S. Nimura, D.M. Packwood, J. Park, and H. Imahori, *A Hydroxamic Acid Anchoring Group for Durable Dye ‐ Sensitized Solar Cells Incorporating a Cobalt Redox Shuttle.* ChemSusChem, 2017. **10**(17): p. 3347-3351.

161. Repain, V., G. Baudot, H. Ellmer, and S. Rousset, *Two-Dimensional Long-Range–Ordered Growth of Uniform Cobalt Nanostructures on a Au (111) Vicinal Template.* EPL (Europhysics Letters), 2002. **58**(5): p. 730.

162. Voigtländer, B., G. Meyer, and N.M. Amer, *Epitaxial Growth of Thin Magnetic Cobalt Films on Au(111) Studied by Scanning Tunneling Microscopy.* Phys. Rev. B, 1991. **44**(18): p. 10354-10357.

163. Krotzky, S.r., C. Morchutt, V.S. Vyas, B.V. Lotsch, R. Gutzler, and K. Kern, *Thermodynamics of the Segregation of a Kinetically Trapped Two-Dimensional Amorphous Metal–Organic Network.* J. Phys. Chem. C, 2016. **120**(8): p. 4403-4409

164. Lingenfelder, M.A., H. Spillmann, A. Dmitriev, S. Stepanow, N. Lin, J.V. Barth, and K. Kern, *Towards Surface-Supported Supramolecular Architectures: Tailored*

Coordination Assembly of 1,4-Benzenedicarboxylate and Fe on Cu(100). Chemistry - A European Journal, 2004. **10**(8): p. 1913-1919.

165. Langner, A., S.L. Tait, N. Lin, C. Rajadurai, M. Ruben, and K. Kern, *Self-Recognition and Self-Selection in Multicomponent Supramolecular Coordination Networks on Surfaces.* Proc. Natl. Acad. Sci. U. S. A., 2007. **104**(46): p. 17927-17930.

166. Stepanow, S., N. Lin, D. Payer, U. Schlickum, F. Klappenberger, G. Zoppellaro, M. Ruben, H. Brune, J.V. Barth, and K. Kern, *Surface‐Assisted Assembly of 2d Metal‐Organic Networks That Exhibit Unusual Threefold Coordination Symmetry.* Angew. Chem., 2007. **119**(5): p. 724-727.

167. Arndtsen, B.A., R.G. Bergman, T.A. Mobley, and T.H. Peterson, *Selective Intermolecular Carbon-Hydrogen Bond Activation by Synthetic Metal Complexes in Homogeneous Solution.* Acc. Chem. Res., 1995. **28**(3): p. 154-162.

168. Li, Q., B. Yang, J. Bjork, Q. Zhong, H. Ju, J. Zhang, N. Cao, Z. Shi, H. Zhang, D. Ebeling, A. Schirmeisen, J. Zhu, and L. Chi, *Hierarchical Dehydrogenation Reactions on a Copper Surface.* J. Am. Chem. Soc., 2018. **140**(19): p. 6076-6082.

169. Ruffieux, P., S. Wang, B. Yang, C. Sánchez-Sánchez, J. Liu, T. Dienel, L. Talirz, P. Shinde, C.A. Pignedoli, and D. Passerone, *On-Surface Synthesis of Graphene Nanoribbons with Zigzag Edge Topology.* Nature, 2016. **531**(7595): p. 489.

170. Weigelt, S., C. Busse, C. Bombis, M.M. Knudsen, K.V. Gothelf, E. Lægsgaard, F. Besenbacher, and T.R. Linderoth, *Surface Synthesis of 2d Branched Polymer Nanostructures.* Angew. Chem., 2008. **120**(23): p. 4478-4482.

171. Treier, M., N.V. Richardson, and R. Fasel, *Fabrication of Surface-Supported Low-Dimensional Polyimide Networks.* J. Am. Chem. Soc., 2008. **130**(43): p. 14054-14055.

172. Fan, Q., C. Wang, Y. Han, J. Zhu, W. Hieringer, J. Kuttner, G. Hilt, and J.M. Gottfried, *Surface‐Assisted Organic Synthesis of Hyperbenzene Nanotroughs.* Angew. Chem., Int. Ed., 2013. **52**(17): p. 4668-4672.

173. Matena, M., J. Björk, M. Wahl, T.-L. Lee, J. Zegenhagen, L.H. Gade, T.A. Jung, M. Persson, and M. Stöhr, *On-Surface Synthesis of a Two-Dimensional Porous Coordination Network: Unraveling Adsorbate Interactions.* Phys. Rev. B, 2014. **90**(12): p. 125408.

174. Knor, M., H.-Y. Gao, S. Amirjalayer, A. Studer, H. Gao, S. Du, and H. Fuchs, *Stereoselective Formation of Coordination Polymers with 1, 4-Diaminonaphthalene on Various Cu Substrates.* Chem. Commun., 2015. **51**(54): p. 10854-10857

175. Katano, S., Y. Kim, M. Hori, M. Trenary, and M. Kawai, *Reversible Control of Hydrogenation of a Single Molecule.* Science, 2007. **316**(5833): p. 1883-1886.

176. Fischer, S., A.C. Papageorgiou, J.A. Lloyd, S.C. Oh, K. Diller, F. Allegretti, F. Klappenberger, A.P. Seitsonen, J. Reichert, and J.V. Barth, *Self-Assembly and Chemical Modifications of Bisphenol a on Cu (111): Interplay between Ordering and Thermally Activated Stepwise Deprotonation.* ACS Nano, 2013. **8**(1): p. 207-215.

177. Bebensee, F., K. Svane, C. Bombis, F. Masini, S. Klyatskaya, F. Besenbacher, M. Ruben, B. Hammer, and T. Linderoth, *Adsorption and Dehydrogenation of Tetrahydroxybenzene on Cu (111).* Chem. Commun., 2013. **49**(81): p. 9308-9310.

178. Zhong, D., J.-H. Franke, S.K. Podiyanachari, T. Blömker, H. Zhang, G. Kehr, G. Erker, H. Fuchs, and L. Chi, *Linear Alkane Polymerization on a Gold Surface.* Science, 2011. **334**(6053): p. 213-216.

179. Zhou, H., J. Liu, S. Du, L. Zhang, G. Li, Y. Zhang, B.Z. Tang, and H.-J. Gao, *Direct Visualization of Surface-Assisted Two-Dimensional Diyne Polycyclotrimerization.* J. Am. Chem. Soc., 2014. **136**(15): p. 5567-5570.

180. Wiengarten, A., K. Seufert, W. Auwärter, D. Ecija, K. Diller, F. Allegretti, F. Bischoff, S. Fischer, D.A. Duncan, and A.C. Papageorgiou, *Surface-Assisted Dehydrogenative Homocoupling of Porphine Molecules.* J. Am. Chem. Soc., 2014. **136**(26): p. 9346-9354.

181. Dobereiner, G.E. and R.H. Crabtree, *Dehydrogenation as a Substrate-Activating Strategy in Homogeneous Transition-Metal Catalysis.* Chem. Rev., 2009. **110**(2): p. 681-703.

182. Mieszawska, A.J., R. Jalilian, G.U. Sumanasekera, and F.P. Zamborini, *Synthesis of Gold Nanorod/Single-Wall Carbon Nanotube Heterojunctions Directly on Surfaces.* J. Am. Chem. Soc., 2005. **127**(31): p. 10822-10823.

183. Hockly, E., V.M. Richon, B. Woodman, D.L. Smith, X. Zhou, E. Rosa, K. Sathasivam, S. Ghazi-Noori, A. Mahal, and P.A. Lowden, *Suberoylanilide Hydroxamic Acid, a Histone Deacetylase Inhibitor, Ameliorates Motor Deficits in a Mouse Model of Huntington's Disease.* Proc. Natl. Acad. Sci. U. S. A., 2003. **100**(4): p. 2041-2046.

184. Lloyd, J.A., A.C. Papageorgiou, S. Fischer, S.C. Oh, O.z. Sağlam, K. Diller, D.A. Duncan, F. Allegretti, F. Klappenberger, and M. Stöhr, *Dynamics of Spatially Confined Bisphenol a Trimers in a Unimolecular Network on Ag (111).* Nano Lett., 2016. **16**(3): p. 1884-1889.

185. Oh, S.C., J.A. Lloyd, S. Fischer, Ö. Sağlam, A.C. Papageorgiou, K. Diller, D.A. Duncan, F. Klappenberger, F. Allegretti, and J. Reichert, *Isomerism Control of Diethylstilbestrol by Metal Surface Induced O–H Cleavage.* Chem. Commun., 2018. **54**(88): p. 12495-12498.

186. Tait, S.L., Y. Wang, G. Costantini, N. Lin, A. Baraldi, F. Esch, L. Petaccia, S. Lizzit, and K. Kern, *Metal− Organic Coordination Interactions in Fe− Terephthalic Acid Networks on Cu (100).* J. Am. Chem. Soc., 2008. **130**(6): p. 2108-2113.

187. Kormoš, L.s., P. Procházka, T.s. Šikola, and J. Čechal, *Molecular Passivation of Substrate Step Edges as Origin of Unusual Growth Behavior of 4, 4′-Biphenyl Dicarboxylic Acid on Cu (001).* J. Phys. Chem. C, 2018. **122**(5): p. 2815-2820.

188. Kühne, D., F. Klappenberger, W. Krenner, S. Klyatskaya, M. Ruben, and J.V. Barth, *Rotational and Constitutional Dynamics of Caged Supramolecules.* Proc. Natl. Acad. Sci. U. S. A., 2010. **107**(50): p. 21332-21336.

189. Palma, C.A., J. Bjork, F. Klappenberger, E. Arras, D. Kuhne, S. Stafstrom, and J.V. Barth, *Visualization and Thermodynamic Encoding of Single-Molecule Partition Function Projections.* Nat. Commun., 2015. **6**: p. 6210.

190. Folkers, J.P., C.B. Gorman, P.E. Laibinis, S. Buchholz, G.M. Whitesides, and R.G. Nuzzo, *Self-Assembled Monolayers of Long-Chain Hydroxamic Acids on the Native Oxide of Metals.* Langmuir, 1995. **11**(3): p. 813-824.

191. Schmitz, C.H., M. Schmid, S. Gärtner, H.-P. Steinrück, J.M. Gottfried, and M. Sokolowski, *Surface Polymerization of Poly(P-Phenylene-Terephthalamide) on Ag(111) Investigated by X-Ray Photoelectron Spectroscopy and Scanning Tunneling Microscopy.* J. Phys. Chem. C, 2011. **115**(37): p. 18186-18194.